Vilniaus universitetas
Fizikos fakultetas
Lazerinių tyrimų centras

Džiugas Kimbaras

FEMTOSEKUNDINĖS SKYROS VAIZDINIMAS PANAUDOJANT SUMINIO DAŽNIO GENERACIJĄ

Magistrantūros studijų baigiamasis darbas

Lazerinės fizikos ir optinių technologijų
studijų programa

Studentas	Džiugas Kimbaras
Leista ginti	2018-05-28
Darbo vadovas	Dr. Rytis Butkus
Konsultantas	Dr. Paweł Wnuk
Konsultantas	Prof. Dr. Matthias Kling
LTC direktorius	Prof. Dr. Roaldas Gadonas

Vilnius 2018

Vilnius University
Faculty of Physics
Laser Research Center

Džiugas Kimbaras

FEMTOSECOND IMAGING BASED ON SUM FREQUENCY GENERATION

Master's thesis

Study programme of
Laser Physics and Optical Technologies

Student	Džiugas Kimbaras
Permitted to defend	2018-05-28
Supervisor	Dr. Rytis Butkus
Advisor	Dr. Paweł Wnuk
Advisor	Prof. Dr. Matthias Kling
Director of LRC	Prof. Dr. Roaldas Gadonas

Vilnius 2018

Table of Contents

1. List of abbreviations

BBO – beta Barium Borate (β-BaB_2O_4)

BSI – Back Side Illuminated

CCD – charge-coupled device

CMOS – complementary metal–oxide–semiconductor

CW – continuous-wave

EM – electromagnetic

FOV – field of view

FPS – frames per second

FRAME – Frequency Recognition Algorithm for Multiple Exposures

FWHM – full width at half maximum

GVD – group velocity dispersion

GVM – group velocity mismatch

ISAS – image signal accumulation sensor

ISIS – In-situ Storage Image Sensor

MCG – multi-collection-gate

NA – numerical aperture

ND – neutral density

SF-STAMP – Sequentially Timed All-optical Mapping Photography utilizing Spectral Filtering

SNR – signal-to-noise ratio

SPAD – single-photon avalanche diode

STAPM – Sequentially Timed All-optical Mapping Photography

TG-FROG – Transient-grating Frequency-resolved Optical Gating

2. Introduction

Time-resolved imaging is a fascinating tool, allowing observation of otherwise invisible high-speed phenomena. Since 1878, pioneered by E. Muybridgne, who captured image sequence of a galloping horse [1], until recently, when slow-motion propagation of light itself [2] can be observed, art and science of high-speed photography gradually progressed, new techniques and methods of capturing events in slow-motion were invented.

Over the years, clever mechanical solutions like using multiple cameras [1], the use of rotating optical elements [3][4], improving speed of mechanical shutters, invention of the CCD sensor [5] (awarded by Nobel prize), first high-speed digital camera [6], steadily increased frame rate and shortened exposure time by several orders of magnitude eventually reaching $10^8\ fps$ [7] and 10^{-11} s [8].

Not only high-speed imaging techniques provide beautiful images, it also is a powerful tool of collecting spatial, temporal and spectral data about various processes in nature. Having this time-resolved information about various ultra-fast processes enriches knowledge related to a number of different fields – from biology and medicine [9][10], industry [11] to fundamental research like light transport [12], carrier dynamics [13], nonlinear processes [14] and other.

As science progresses, spatial scales get smaller, temporal – shorter. Hence, new techniques and approaches are still being developed. Conventional high-speed photography is limited by electronic memory storing and readout speed [15]. Time resolution that such devices can achieve is generally down to hundreds of picoseconds [6]. Using some clever workarounds, it is possible to achieve better resolution down to tens of picoseconds or even hundreds of femtoseconds [16]. Generally if processes of our interest are extremely short, like charge carrier dynamics, light – matter interaction or nonlinear processes, faster tools are needed to act like a camera shutter. Such tool is a light itself – a laser pulse. Techniques using laser pulses for high-speed imaging have also been extensively developed [17][18][19][20].

Main topic of this thesis was building a high-speed imaging setup by using sum frequency generation based optical shutter together with wide-field imaging module. Such module would allow capturing and recreating various physical phenomena with a femtosecond temporal resolution.

Main tasks of this thesis were to design, build and test sum-frequency generation based high-speed imaging device.

The layout of this thesis is following. In Chapter 2 review of current time-resolved imaging techniques is presented. Chapter 3 is a brief overview of related theory. Chapter 4 is a

detailed presentation of designed high-speed imaging setup. In Chapter 5 main test results are presented followed by conclusions in Chapter 6.

3. Review of time-resolved imaging techniques

This chapter is dedicated to overview of recent techniques of high-speed imaging together with a brief overview of non-optical ways of ultra-fast imaging.

3.1. Non-optical high-speed imaging

Over decades, a number of different approaches were developed to satisfy the need of high-speed imaging devices. Definition of video camera may vary, depending on number of captured frames. Generally, imaging devices can be sorted into two large groups – continuous mode cameras and burst-mode cameras. Continuous mode cameras record a large number of frames to memory, while burst-mode cameras are usually faster, but are able to record a smaller number of frames (for example less than 100). There are many variations of each camera differing in sensor size, construction type, number of pixels and memory storing principles and other properties. As there are a lot of different approaches only several methods and technologies are briefly mentioned below, because this work is mainly focused on optical methods.

In ISIS (In-situ Storage Image Sensor) implementation [15], memory elements are attached to each pixel allowing storing signals without reading them out, thus improving FPS. There is a number of ISIS improvements and variations such as BSI (Back Side Illuminated) ISIS for better fill factor; CCD/CMOS ISIS – for high-speed imaging and high-speed readout; ISAS (Image Signal Accumulation Sensor) – ISIS with ability to accumulate several frames, for better signal-to-noise ratio; MCG (Multi Collection Gate) – for better frame rate and few others. Generally such cameras can capture >100 frames with frame rates around 1-16.7 Mfps [15]. Current maximum frame rate reached with MCG BSI sensor is 100 Mfps; 5 frames; 512 x 576 [7]. Other recent example is 50 Mfps MCG BSI sensor, capturing 1200 images at 50 Mfps [7]. CMOS sensors with pixel memory storage have also been developed and 20 Mfps camera, capturing 400 x 256 resolution images, with 128 on chip memory cells per pixel, was demonstrated [21][22].

Another approach to improve fps is to use multiple image sensors or one large sensor (or segmented sensor) and capture several frames onto different parts of the sensor. These methods use different approaches of post processing, and image splitting, so each should be analyzed separately. Examples could be framing cameras like prism beam splitter camera [23][24], capturing up to 16 frames up to 200 Mfps, rotating mirror cameras [25] – 128 images up to 25 Mfps; multi

aperture camera [26] – 32 images, up to 200 Mfps and others [27]. Generally such cameras have lower amount of captured images, but higher frame rates.

Another worth mentioning method is using SPAD (single-photon avalanche diode) [2][8]. SPAD technology is based upon silicon CMOS array of single-photon avalanche diode detectors. Each pixel is operated in time correlated single photon counting mode. SPAD used before as a single detector now can be combined into arrays, which allows capturing 2D image. In 2015, 32 x 32 images with a resolution of 67 ps and 700 ps between frames were recorded [2], capturing pulse propagation in air, as well as plasma dynamics. Total recording length of camera was 69 ns. In 2017 laser propagation in optical fiber with resolution of 150 ps was demonstrated [8]. Compared to CCD this method has a high time resolution and single – photon sensitivity.

To conclude, high-speed imaging based on electronic sensors only – theoretically estimated temporal resolution of silicon based sensor is $\Delta\tau = 6.12\ \delta$ [6], where $\Delta\tau$ is temporal resolution limit (in ps); while δ – average penetration depth of photons (in μm). This corresponds to tens of picoseconds at room temperature and visible light and frame rates around tens of Gfps.

It should be also mentioned, that signal-to-noise ratio becomes extremely low, at such integration times. So most of the time, processes observed must be repetitive. Another aspect is that reaching such low integration times is an extreme technological challenge.

3.2. Streak camera based imaging

One way to improve time resolution is to use a detector, which can work faster than widely used 2D CCD or CMOS sensors. An example of such detector is a streak camera. Time resolution achieved with streak camera is 0.3 – 0.1 ps, for example Hamamatsu streak camera FESCA-100 C11853-01 [28]. Operating principle of streak camera could be described as following: light to be measured travels through a slit on the photo cathode. Photons hitting cathode release electrons proportional to the intensity. Electrons are accelerated towards the phosphor screen. Before hitting phosphor screen, electrons travel through focus electrodes, where a synchronized high-speed voltage is applied. Electrons are swept in one dimension relatively to their arrival time. After phosphor screen, where electrons are converted back into photons, a 2D streak image is recorded. One dimension of recorded image is the same spatial dimension, while other axis corresponds to arrival time of the photons. Time resolution as well as duration of recorded event depends on applied sweeping voltage. One of the main downsides of such detection is that captured image has only one spatial dimension.

MIT together with University of Zaragoza overcame this issue by synchronizing streak camera with mirror-scanning system [16] which allowed them to record multiple horizontal one

dimensional slices of repetitive process, for example - laser pulse propagation. Recording laser pulse light is also helpful for improving low SNR, which is highly influenced by extremely short integration time. After adding number of one dimension movies together, two-dimensional movie of the event is recreated. With such technique, in 2013 Velten et al. were able to demonstrate light propagation in various scenes with time resolution as short as 1.85 ps [16]. Important aspects such as synchronization between light source and camera, the need of statistically repetitive process, correct data interpretation (time unwrapping) and long recording times should be kept in mind.

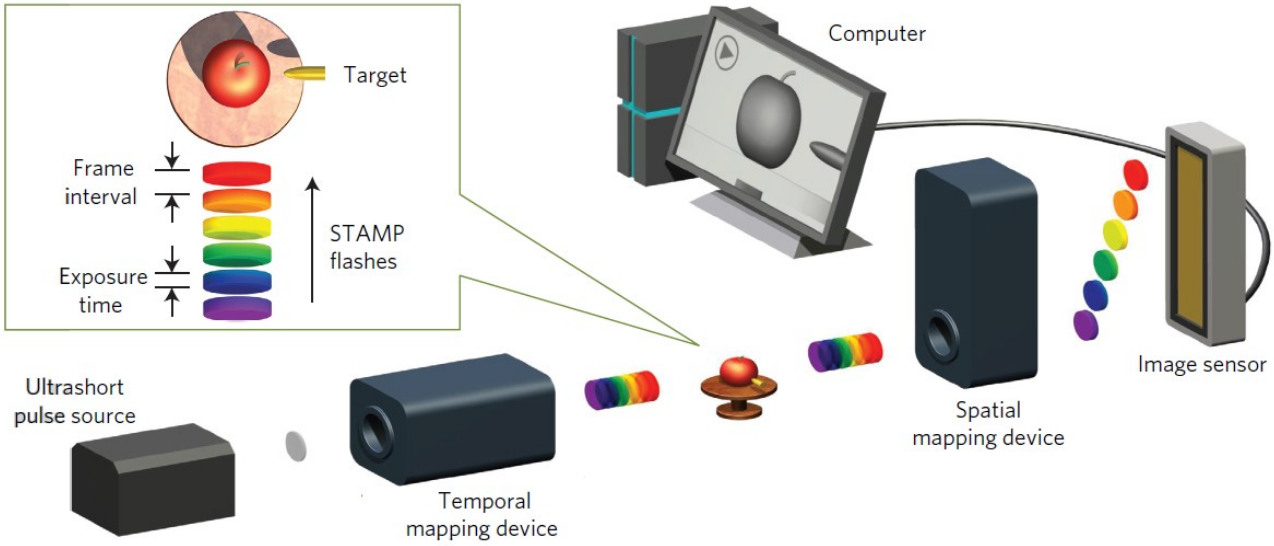

Figure 1. Basic schematic of STAMP. [29]

3.3. STAMP method

In 2014 a new approach of burst camera was introduced, called Sequentially Timed All-optical Mapping Photography, or STAMP [29]. This innovative technique was based on capturing a sequence of short laser pulses carrying spatial information about an image and mapping them on different parts of a sensitive image sensor. By mapping different frames on different parts on the sensor, the use of traditional, slow, image sensor is allowed without the loss of time resolution. All-optical separation of laser pulses (frames of the movie), allows short exposure times and high frame rates of the picture sequence.

First version of STAMP working principle can be described as follows. Ultrashort laser pulse is dispersed and shaped (by temporal mapping device) into a series of discrete daughter pulses in different spectral bands. Those pulses hit a target as successive flashes in reflective or transmissive manner and spatial information of a target is encoded into daughter pulses. Each pulse carries information about different moment in time. Then, daughter pulses are optically directed to

different parts of image sensor by a spatial mapping device. Then the whole image is recorded, digitally processed and burst-mode motion picture is constructed. For a proof-of-principle experiment, image sequence of 6 images were recorded with a maximum frame rate of 4.37 Tfps, 229 fs interval between frames and average exposure time of 733 fs for each frame [29]. Several different targets were observed, like plasma dynamics on the surface of a glass plate and lattice vibrational waves. A main scheme of STAMP is depicted in Figure 1. [29]

Main advantage of such setup is extremely high temporal resolution while maintaining ability to capture non repetitive process. Also, this method is quite versatile and could be implemented in different kind of setups. Unfortunately, such method allows only a low number of total frames to be captured, although authors proposed a new and better approach and claimed that this number can be increased [30]. Also, higher number of frames comes at a price of lower pixel resolution, as image sensor must be divided by a number of frames. Another issue is that spectral information is lost, as each frame has to be separated into different parts of EM spectrum. Due to the spectral separation, the temporal resolution is reduced as well. Last issue is the loss of intensity, as for each frame, only small amount of the EM spectrum is captured.

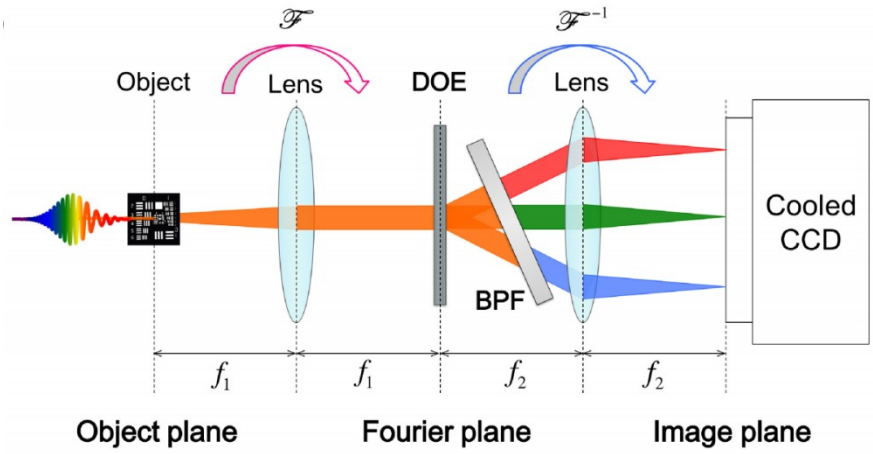

Figure 2. Schematic setup of SF-STAMP. [30]

Later, as mentioned above, a second version of STAMP called SF-STAMP [30] (SF stands for spectral filtering) was introduced [30] [14] [31]. It increased the total number of frames up to 25. The main innovation of SF-STAMP was changing temporal mapping device to a dispersive element and spatial mapping device to a diffractive optical element and a band pass filter. Image amplitude or amplitude and phase information is encoded into dispersed pulse. Different spectral parts of the pulse correspond to different time. Then, encoded dispersed pulse is Fourier transformed and divided by a diffractive optical element into a number of copies. Afterwards, a tilted band pass filter spectrally differentiates each element of diffracted beam array. Finally each

pulse is reconverted by a second lens and an array of different spectrum images is formed on the image sensor. If original pulse is dispersed linearly and spectral differentiation is done correctly, captured images can be represented as a sequence of images in time, like in a burst camera. Ultrafast laser dynamics like ablation, filaments [30] [14] and phase transitions [31] were observed. A maximum number of 25 frames with exposure time of 565 fs for each frame, interval between frames of 133 fs and 450 x 450 pixel resolution were achieved [31].

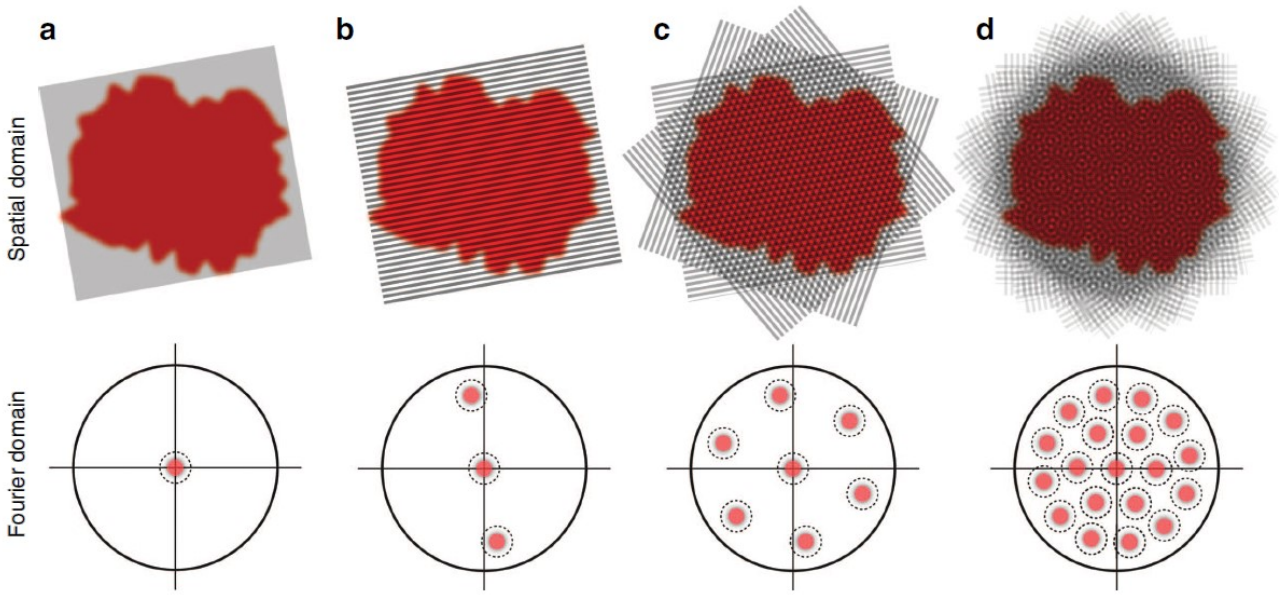

Figure 3. Operating principle of FRAME. Uniformly illuminated sample and its Fourier spectrum can be seen in a). In b) sample is illuminated with sinusoidal modulation. Pictures c) and d) represent implemented multi-illumination, using sinusoidal modulation in different directions and spatial frequencies. [12]

3.4. FRAME method

Other interesting approach of capturing sequence of time-resolved images was proposed and implemented by scientists from Lund University. This methodology called FRAME [12] (Frequency Recognition Algorithm for Multiple Exposures) relies on the premise that power spectrum of image is strongly shifted into low spatial frequencies. Then adding sinusoidal modulation with frequency v to an image creates two image copies at $\pm v$ in the Fourier domain. By altering spatial frequency and orientation of this modulation, it is possible to strategically place number of copies at different parts of the Fourier plane. Recording such Fourier Plane with CCD camera, allows to capture information about a number of images with just one exposure event.

Afterwards, by using filtering and post processing distinct parts of power spectrum can be selected and each of the images can be reconstructed separately.

This technique could be adapted into different kind of setups: pump-probe, wave mixing, scattering, etc. A probe pulse is split into several relatively delayed pulses, which probe or illuminate the object of interest. Such pulses are spatially modulated with distinct orientations and/or orientations. The Fourier plane of an object is then recorded. In September of Ehn et al. demonstrated sequence of time-resolved images of pulse traveling through Kerr medium with resolution of 200 fs [12]. Time resolution is determined by gate pulse duration and time step between frames by delay between probing pulses. This can vary a lot depending on laser and probing setup.

More importantly, this technique allows collecting information about a single event, which means it is possible to observe more complex, non-repetitive processes. Unfortunately, an additional probe pulse is necessary for adding each new frame, thus the system becomes more complicated. As for now, only several frames were recorded and interpolation methods were used to simulate images in between the captured frames.

3.5. Time-resolved microscopy

Another large subgroup of high-speed imaging are pump-probe based methods. The main principle of such methods is repetitive measurement of a statistically similar event, by changing delay between “pump” (signal, trigger) and “probe” (gate, measurement) pulses. With one of many measurements, one frame (or a single spectrum in time-resolved spectroscopy) is recorded. After whole sequence of measurements is recorded, a movie with extremely high temporal resolution (<100 fs as will be presented below) can be recreated. The main advantage of such systems is that generally time resolution of the movie depends purely on gate (probe) pulse duration. Another huge benefit and simplification is that there is no need for high-speed image sensors. On the other hand, ultra-short lasers are needed to keep up with high temporal resolution. The main downside is the need of measuring repetitive processes. Again, in some cases even burst cameras have to take repetitive measurements due to extremely low light collection, because of short integration times.

There are many different variations of time-resolved microscopy and each of them offers some unique advantages and disadvantages. Time-resolved imaging using light upconversion would also fall in the pump-probe or at least pump-probe-like measurement category.

3.5.1. Transient absorption, shadowgraphy

One of the most popular approaches in spectroscopy is transient absorption. In this approach usually the pump-induced changes of the probe beam transmission are recorded while changing delay between the pump and probe. Usually the wavelength of a pump beam is tunable, while a probe has broader spectrum, and dynamics of the spectral changes can be observed. This observation approach is usually focused on the more complex transient absorption processes. Changes in transmission are small and related more to the excitation (emission, bleaching) of molecules, nanostructures or other materials, rather than large changes created by, e.g. ablation processes. These small changes require sensitive detection, hence sensitive detectors are used with lock-in amplifiers, which are incompatible with CCD cameras. Because of this, if spatial and temporal resolution is desired, both temporal and spatial scanning is required. This has been successfully done and remains a popular technique, analyzing various excited state dynamics like analyzing carrier motion, plasmon propagation, exciton migration [13][32]. Recently, however, examples of sensitive wide-field transient absorption measurements were presented, using both CMOS [33] and smart pixel array sensors [34]. Demonstration of photo-induced changes in films with several hundred nanometer resolution and sub-10 fs pump and probe pulses were demonstrated [33].

Another approach is time-resolved shadowgraphy or shadow-imaging. This approach may as well be called as a version of transient absorption pump-probe technique. In this setup, the pump beam generates an event, while the probe beam propagates perpendicularly to an event and the event plane is imaged on the image sensor. Usually the probe beam is a second harmonic of the pump beam and there is a bandpass filter for pump beam wavelength before the image sensor. Dynamical object of interest, for example laser-induced material ejection during ablation process [35], can absorb, partially absorb, reflect, scatter, diffract or refract light of the probe beam. Because of that, in the final image, object of interest looks dark, as we see the absence of light, due to the object “blocking” the back light. The image is called a shadowgraph or a shadow image. Various processes could be observed like laser-induced pressure waves in liquids, solids and gasses [36][19][37], plasma generation [38]. The main advantages of this setup are a relatively simple experimental setup, and temporal resolution limited only by gate, which undergoes relatively simple optical path before hitting object. Examples of setups using 50 fs probe pulses were demonstrated [35] [36][37]. The main drawback is that detected light is the remaining light, which was not obstructed by object – we don’t see any spectral information or more precise features of the object.

Transient absorption pump-probe methodology could also be implemented not only in a way of measuring transmission, but reflection [39][40] or scattering as well [11], as absorption changes the properties of reflectivity. This method is also based on irradiating the sample with the

pump pulse, to create some changes in an object, and probing the affected spot with delayed probe pulse. The probe pulse, after reflection from sample, is directed to an image sensor. Similar to shadowgraphy, usually the probe pulse is the second harmonic of the pump pulse and a bandpass filter for probe beam is placed in front of an image sensor. Using this technique, laser-induced surface changes of various materials can be observed as well plasma dynamics. Both shadowgraphy (side-view observation) and reflective transient absorption can be combined in the same setup [20].

3.5.2. Kerr-gated wide-field microscopy

Another pump-probe like method, called Kerr-gated microscopy, is based on Kerr effect, where isotropic material becomes birefringent in a presence of intense electric field. Linearly polarized light traveling through birefringent medium experience partial change of polarization (depending on light intensity, length of birefringent zone). Essential part of Kerr-gate time-resolved measurements is a Kerr-gate, which is a nonlinear isotropic medium placed between crossed polarizers.

The pump pulse creates some kind of event on the object, this could be either excitation – the fluorescent light is collected, or some scattering event – the scattered light is observed. This light is collected and goes through Kerr-gate to the image sensor. Another short pulse (gate or probe) is going through Kerr medium and induces birefringence, which induces phase shift between orthogonal components of light and rotates the polarization of collected light. As the polarization is rotated, some of the light is transmitted through the analyzer. Short pulse “gates” the collected light in same manner as a mechanical shutter – the camera collects light only when the gate pulse is present. Rather than being based on short stroboscopic illumination for scattering, reflection or absorption observation, this method is more similar to traditional camera, where scattered collected light is being gated. Changing delays between the pump and gate pulses allows recreating stop motion movies of the event.

Kerr-gated wide-field microscopy was presented in 2008 by L. Gundlach and P. Piotrowiak [41]. They investigated emission of gold nanoparticles and DNS solution with time resolution of sub-110 fs. Studies of CdSSe nanowires and ZnO nanowires by J. Blake et al. were presented with <100 fs resolution [17].

As well as in other pump-probe experiments, the short gate pulse is necessary. Also, collected light from the object should be ideally unaffected by dispersion. This is usually achieved by using reflective optics, like in this case - Cassegrain or Schwarzschild objectives. Another aspect is necessity of low-thickness optical elements like polarizers or Kerr medium.

One of the challenges of this setup is obtaining high SNR ratio, as it is inversely related to temporal response of the setup. Some of the collected light still goes through crossed polarizers

even if there is no gate pulse. This contrast between desired signal and leakage noise is limited by contrast of polarizers and by magnitude of Kerr response, which depends on nonlinear coefficient of Kerr medium, its length and gate pulse intensity. Usually liquid materials have higher nonlinear coefficient, but longer and asymmetric temporal response, compared to, for example, fused silica or YAG. Gate pulse intensity is limited by the damage threshold of Kerr medium as well as other nonlinear effects. Longer Kerr mediums also increase signal level at a cost of temporal resolution due to dispersion and group velocity mismatch (GVM).

Speaking of wavelengths, Kerr-gated microscopy leaves the signal unchanged. By replacing CCD camera with a dispersive element and spectrometer, time-resolved spectroscopy measurements can be performed.

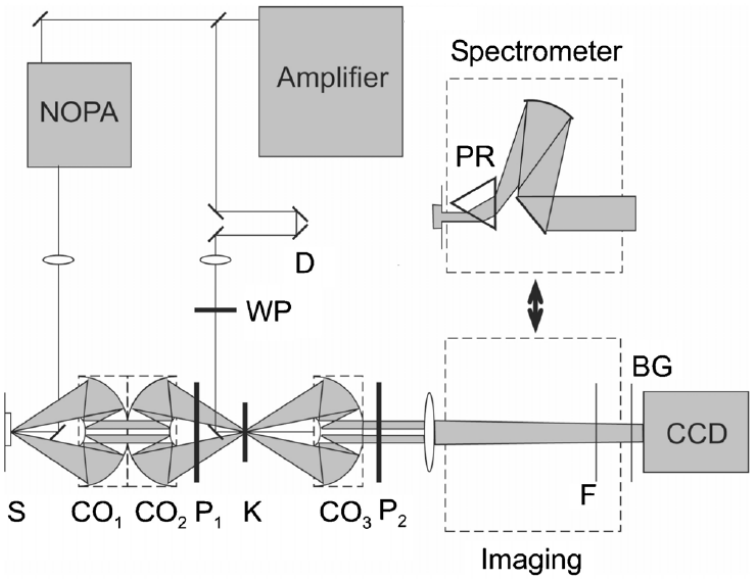

Figure 4. Setup of the Kerr-gated fluorescence microscope. S, sample; CO1−3, Cassegrain objectives; P1−2, polarizer; K, Kerr medium; D, delay line; F, BG, spectral filter; WP, waveplate; PR, prism. Reproduced from [41].

3.5.3. Upconversion and optical parametric amplification

Another way to create an optical gate is to use second order nonlinearity and generate sum frequency or utilize optical parametric amplification. A scattered, transmitted or fluoresced (depending on the object of interest) light is collected and directed towards nonlinear crystal, where it overlaps with short gate pulse. When signal and gate pulses overlap, sum frequency is generated or parametric amplification takes place, depending on chosen conditions. Either way, time-resolved part of a signal is generated – sum frequency in upconversion or idler in parametric amplification, and collected by an image sensor. There is a number of configurations, each presenting own traits and features.

Depending on gate beam wavelength and power, sum frequency generation or parametric amplification can be chosen, which results in different wavelengths of registered pulses as well as different noise sources and characteristics. When using sum frequency generation based gating, background is generated due to the second harmonic of the gate beam, if wavelength of interested matches gating frequency. On most of other occasions background could be spectrally filtered out. If gating is based on parametric amplification, signal is amplified, which is not possible in sum frequency or Kerr-gating, but due to spontaneous parametric down conversion, background is also generated and can easily become limiting factor [10].

Non-collinear and collinear geometries could be utilized. Non-collinear geometries give additional angular separation from desired signal and unwanted background light at a price of more complex beam paths and various additional distortions. Another option is to upconvert the infinity corrected light or light at the image plane.

Compared to Kerr-gating, phase matching condition has to be satisfied, but higher nonlinear efficiencies are achieved. Also, the change of wavelength could be beneficial, if observed wavelengths are out of camera sensitivity range.

A number of works were dedicated to learning more about this type of imaging and investigating various aspects of it. A lot of works use both upconversion gating and parametric amplification for imaging through scattering media [42][43][44] and resolving different depths of the object of interest [44][9]. Study of light transport in complex, partially transmissive media was investigated by L. Pattelli et al. [45] using the collinear upconversion of the image and achieved time resolution was 174 fs. Parametric image amplification was also used also for ultra-high-speed imaging of light propagation on diffusing screen with picosecond time resolution [18][46].

This work uses the sum frequency generation based optical shutter to build a time-resolved wide-field microscope. Many related experiments have been done before. For example utilizing non-collinear upconverion spectroscopy [47][48], investigating spatial resolution of the upconverted images [49], study of the light transport by upconverting transient signal [45], using Kerr gate instead of sum frequency generation[41][17] and others. Although these experiments give some great insights and show nice applications, to our knowledge, no such exact configuration was implemented, for imaging the scattered light of the Object and upconverting it in a non-collinear geometry to investigate the time resolved light propagation, scattering and reflection dynamics.

The Imaging setup, based on the non-collinear sum frequency generation, should have high SNR, as the detected upconverted signal is spatially separated from the Gate and Object beams and spectral filters can be used to remove most of the unwanted background noise, with few exceptions (analyzed further in this work). The temporal resolution is also competitive compared to other works, as it is in principle limited only by the Gate pulse duration.

Another important notification is that the only condition of recording a ultra-fast event with this setup, is the need of scattering event, as the scattered light is imaged and upconverted. There is no need of the material modification or specific geometries of the Pump beam propagation. Lastly, not only the spatial information, but the spectral information can be recorded as well, giving full data set of temporally resolved spatial and spectral features.

As it will be seen, the temporal resolution achieved with this setup was ~ 50 fs with the spatial resolution of ~ 45.3 lp/mm. The Signal-to-noise ratio varied from ~ 5 dB (weak signals like pulse propagation in a bulk glass), to 33 dB (reflection from a surface, scattering from defects).

Related theory, arising problems and main results are presented and analyzed further in this work.

4. Theory overview

4.1. Description of light pulses and beams

Pulsed laser beams can be described using a mathematical formulation of spatially and temporally modulated plane waves. Propagation in a vacuum of such wave packet is described by the wave equation [50], derived from the Maxwell equations:

$$\nabla^2 \boldsymbol{E} - \frac{1}{c^2}\frac{\partial^2 \boldsymbol{E}}{\partial t^2} = 0; \quad (1)$$

The solution of the wave equation for the wave propagating in z axis can be written in a form [51]:

$$\boldsymbol{E}(t,x,y,z) = \boldsymbol{e}A(t,x,y,z)\exp\big(i(\omega_0 t - k_0 z)\big) \quad (2);$$

Here, x, y are the transverse coordinates, t – the time dimension, E(t,x,y,z) marks the electric field strength, e – the unitary polarization vector, ω_0 – the angular carrier frequency, $k_0 = \frac{n_0\omega_0}{c}$ – the wave vector, A(t,x,y,z) – the complex amplitude. The complex amplitude can be expressed as [51]:

$$A(t,x,y,z) = a(t,x,y,z)\exp(i(\varphi(t,x,y,z))); \quad (3)$$

The first term a defines the real amplitude, while φ is the phase term. If a light wave, propagating in z direction, is modulated only in time $a(t,z)$, an electromagnetic wave is called a light pulse and $a(t)$ is its envelope, while a transverse modulation $a(x,y,z)$ represents a laser beam, with its envelope $a(x,y)$. A phase modulation of the light pulse $\varphi(t)$ causes change of the carrier frequency: $\omega(t) = \omega_0 + \frac{d\varphi}{dt}$. Function $\varphi(x,y)$ describes the wavefront of the beam.

Information about Electric field can be represented both in time or frequency domains. Both representations carry the same information and are related to each other by the Fourier transforms [51]:

$$E(t) = \frac{1}{2\pi}\int_{-\infty}^{+\infty} E(\omega)\exp(i\omega t)\,d\omega;\; E(t) = \int_{-\infty}^{+\infty} E(t)\exp(-i\omega t)\,dt; \quad (4)$$

For example, the laser pulse $E(t)$ with the amplitude modulation $A(t)$ has the spectrum (spectral amplitude) $S(\omega) = \int_{-\infty}^{\infty} A(t)\exp(i(w_0 - w)t)\,dt$. Analogously, the laser beam propagating in z direction with the amplitude $A(x,y)$ can be represented with the spatial frequency spectrum $S(k_x, k_y) = \iint_{-\infty}^{\infty} A(x,y)\exp\left(i(k_x x + k_y y)\right)\,dxdy$.

4.2. Gaussian pulse

The most common description of the light pulse envelope is the Gaussian function [51]:

$$a(t) = a_{max} \exp\left(-\frac{t^2}{\tau_0^2}\right); \quad (5)$$

In this expression, a_{max} is the maximal amplitude, τ_0 corresponds to the temporal properties. The pulse duration usually is described either at 0,5 (FWHM) or $1/e$ level of the maximum intensity. This corresponds to $\tau_e = \sqrt{2}\tau_0$; $\tau_{0,5} = \sqrt{2\ln 2}\tau_0$.

Then, the light pulse with both temporal amplitude and phase modulation, would be described by[51]:

$$A(t) = a_{max} \exp\left(-\frac{t^2}{\tau_0^2}\right) \exp\big(i\varphi(t)\big); \quad (6)$$

When an electromagnetic wave is modulated in time, it must have more than one frequency and can be described in a frequency notation, which is equivalent to a time notation. Spectrum of a Gaussian pulse is a Fourier transform of $A(t)$. For a Gaussian pulse, its spectrum is also a Gaussian function with spectrum widths equal to $\Delta\Omega_{0,5} = \frac{2\sqrt{2\ln 2}}{\tau_0}$; $\Delta\Omega_e = \frac{2\sqrt{2}}{\tau_0}$. A Gaussian pulse with a phase modulation has a broader spectrum and ideally can be compressed into a shorter pulse, removing the phase modulation, as width of the spectrum is inversely proportional to the minimal pulse duration.

4.3. Gaussian beam

Similar to the light pulse characterization, most common spatial modulation of the plane wave is the Gaussian beam with its amplitude [51]:

$$a(r) = a_{max} \exp\left(-\frac{r^2}{\rho_0^2}\right); \quad (7)$$

Here $r = \sqrt{x^2 + y^2}$ is the radial coordinate and ρ_0 – the coefficient relating to the spatial parameters. The beam radius at $I = |A|^2 = 0{,}5 I_{max}$ is $\rho_{0,5} = \frac{\sqrt{\ln 2}}{2}\rho_0$, while $I = |A|^2 = \frac{1}{e} I_{max}$ is $\rho_e = \frac{\rho_0}{2}$. Analogous to the spectrum of the Gaussian light pulse, the spatial spectrum of the Gaussian laser beam is also a Gaussian function and sometimes called an angular spectrum, as spectral amplitude can be expressed as a function of angle between propagation axis z of the beam and the $\boldsymbol{k_n}$ vector of the angular spectrum component n.

To see how these modulated waves propagate in space, the Helmholtz equation [50] $(\nabla^2 + k^2)E = 0,$ derived from the Wave equation (1), has to be solved. By applying the slowly varying envelope approximation, the Helmholtz equation is turned into the Paraxial Helmholtz equation [50]:

$$\nabla^2_{Trans} - i2k\frac{\partial A}{\partial z} = 0; \quad (8)$$

One of the solutions of this equation is a Gaussian beam with its main properties [50], describing the spatial distribution of the laser light in space:

$$E(x,y,z) = A_0\frac{\rho_0}{\rho(z)}\exp\left(-\frac{r^2}{\rho_0^2}\right)\exp\left(-ikz - ik\frac{r^2}{2R(z)} + i\xi(z)\right); \quad (9)$$

$$\rho(z) = \rho_0\sqrt{1 + (z/z_0)^2}; \;\; R(z) = z(1 + (z_0/z)^2);$$

$$\xi(z) = \left(\tan^{-1}\frac{z}{z_0}\right); \;\; \rho_0 = \sqrt{\left(\frac{\lambda z_0}{\pi}\right)}; \quad (10)$$

Here, ρ_0 is the minimal radius of the beam at its waist; $\rho(z)$ – the beam radius at the distance z from its waist, $R(z)$ – the radius of curvature, z_0 – the Rayleigh length, where the radius is increased by the factor of $\sqrt{2}$, while the intensity drops twice, $\xi(z)$ – the Gouy phase shift.

When $z \gg z_0$, the beam radius increases approximately linearly with the divergence angle $\theta = \lambda/\pi\rho_0$. Here $\lambda = \lambda_0/n$.

It can be shown, that the evolution of the complex amplitude $A(x,y,z)$ of a Gaussian beam is governed by the solution of the parabolic diffraction equation:

$$\frac{\partial A}{\partial z} = -\frac{i}{2k_0}\left(\frac{\partial^2 A}{\partial x^2} + \frac{\partial^2 A}{\partial y^2}\right), \quad (11)$$

which is analogous to the temporal dispersion equation. The spatial frequencies of a Gaussian beam spectrum get out of phase, while moving in the beam propagation direction, and the beam experiences diffraction.

4.4. Light pulses in dispersive linear medium

In a dispersive medium the Wave equation can be written as [52]:

$$\nabla^2\boldsymbol{E} - \frac{n^2(\omega)}{c^2}\frac{\partial^2\boldsymbol{D}}{\partial t^2} = 0; \quad (12)$$

Here $D = \epsilon_0 E + P$ is the electric displacement field. Let's say that a plane electromagnetic wave, modulated in time is propagating in z direction. The medium is isotropic, linear ($P = P^{(1)}$) dielectric. The Electric field strength $E(t, z)$ can be then written as [51]:

$$E(t,z) = \frac{1}{2\pi} \int_{-\infty}^{+\infty} S(\omega) \exp(i(\omega t - k(\omega)z))\, d\omega; \quad (13)$$

Assuming, that the spectral width of the light pulse is much smaller than the carrier frequency, function $k(\omega_0 + \Omega)$ can be represented in the form of the Taylor series [51]:

$$k(\omega) = k(\omega_0) + \frac{\Omega}{u(\omega_0)} + \frac{g(\omega_0)}{2}\Omega^2 + \frac{h(\omega_0)}{6} + \Omega^3 \ldots; \quad (14)$$

$$u = \frac{d\omega}{dk};\ g = \frac{d^2k}{d\omega^2};\ h = \frac{d^3k}{d\omega^3}; \quad (15)$$

Here u marks the group velocity speed, the group velocity dispersion (GVD) coefficient is marked with g and h – the dispersion of GVD. Since the spectral width $\Delta\Omega$ is much smaller than the carrier frequency ω_0, the complex amplitude $A(t, z)$ will change slowly. By using (13), (14) and (15), change of the complex amplitude $A(t, z)$, propagating in z direction through a dispersive media, can be expressed as following: [51]

$$\frac{\partial A}{\partial z} = -\frac{1}{u(\omega_0)}\frac{\partial A}{\partial t} + \frac{ig(\omega_0)}{2}\frac{\partial^2 A}{\partial t^2} + \frac{h(\omega_0)}{6}\frac{\partial^3 A}{\partial t^3} \ldots; \quad (16)$$

Solving this equation with only the first approximation (one term on the right side), describes that a pulse is propagating in a medium with a group velocity $u(\omega_0)$, while no additional changes are introduced to the amplitude or the phase of the pulse.

When taking into account the second term as well and solving the equation (12), quadratic modulation of the spectral phase, together with the linear frequency modulation is present. This means that the pulse with flat spectral phase becomes temporally broadened due to the group velocity dispersion. The dispersion is characterized by the distance, after which the duration of the pulse is elongated by $\sqrt{2}$: $L_d = \frac{\tau_0^2}{2g(\omega_0)}$. Duration of the pulse changes according to $\tau(z) = \tau_0\sqrt{1 + z^2/L_d^2}$, while the peak of the amplitude change is calculated by $a(z) = a_0/\sqrt[4]{1 + z^2/L_d^2}$.

Depending on the chirp of the pulse and the sign of coefficient g, pulses could be both temporally broadened or shortened (if the original chirp is compensated by chirp introduced by material). More complex changes to the pulse are introduced when taking into account the higher order terms.

4.5. Pulsed beams in nonlinear medium

In the previous expressions, the light induced polarization was written as a linear $\boldsymbol{P} = \boldsymbol{P}^{(1)}$ function. The generalized equation for the light induced polarization (the dipole moment per unit volume) in the material is: [53]

$$P(t) = \chi^{(1)}E(t) + \chi^{(2)}E^2(t) + \chi^{(3)}E^3(t) \ldots$$
$$\equiv \boldsymbol{P^{(1)}(t)} + \boldsymbol{P^{(2)}(t)} + \boldsymbol{P^{(3)}(t)} \ldots; \quad (17)$$

$E(t)$ is the electric field strength, rapidly changing in time; $P(t)$ notes the polarization; $\chi^{(1)}, \chi^{(2)}, \chi^{(3)}$ – accordingly the first (or linear), second and third order optical susceptibilities; $P^{(1)}(t), P^{(2)}(t), P^{(3)}(t)$ are the linear, second-order nonlinear and third-order nonlinear polarizations. Generally, $\tilde{E}(t)$ and $\tilde{P}(t)$ are vectors, while χ is a tensor. While the electric field strength describes the electromagnetic field of the laser pulse, susceptibility is the material property, describing material's response to the electric field. The time varying polarization can act as a source for new components of the electric field, which is why expressing the polarization in terms of the applied field is a common way to describe various nonlinear phenomena. The second order polarization term, which occurs in the noncentrosymetric materials, and the third order nonlinear polarization, occurring in every isotropic media, create separate groups of various nonlinear phenomena.

When the electric field is strong, the nonlinear polarization terms have to be taken into account.

4.5.1. Second order nonlinearity

Let's consider noncentrosymetric crystal as a medium, where $\chi^{(2)} \neq 0$ and an applied electric field having two discrete components[53]:

$$E(t) = E_1 \exp(-i\omega_1 t) + E_2 \exp(-i\omega_2 t) + c.c. \quad (18)$$

Then, second order polarization can be written in a form of:

$$P^{(2)}(t) = \chi^{(2)}E^2(t);$$
$$P^{(2)}(t) = \chi^{(2)}[E_1^2 \exp(-2i\omega_1 t) + E_2^2 \exp(-2i\omega_2 t) + 2E_1E_2 \exp(-i(\omega_1+\omega_2)t) +$$
$$+2E_1E_2^* \exp(-i(\omega_1-\omega_2)t) + c.c.] + 2\chi^{(2)}[E_1E_1^* + E_2E_2^*]; (19)$$

The term $2\chi^{(2)}E_1E_2 \exp(-i(\omega_1+\omega_2)t)$ suggests that one of the components of second order polarization has the frequency equal to the sum of input frequencies. This means, that each atom in the material, due to nonlinear response, has the oscillating dipole moment containing $\omega_1+\omega_2$ frequency component (as well as several others) and emits such radiation. If waves, emitted

by individual atoms, are in phase, waves will interfere constructively and radiation with the frequency $\omega_1+\omega_2$ will be generated.

4.5.2. Three-wave mixing

For the pulsed laser beams, it is needed to take into account the spatial and temporal modulations together, as well as the nonlinear response of the medium. As previously, from the Maxwell equations, the Wave equation can be written[51]:

$$\nabla^2 \boldsymbol{E_n} + \frac{n^2(\omega_n)}{c^2}\frac{\partial^2 \boldsymbol{E_n}}{\partial t^2} = -\frac{1}{\epsilon_0 c^2}\frac{\partial^2 \boldsymbol{P_n^{(1)}}}{\partial t^2} - \frac{1}{\epsilon_0 c^2}\frac{\partial^2 \boldsymbol{P_n^{(2)}}}{\partial t^2}; \quad (20)$$

Here E_n is the electric field strength for each frequency component, n is the linear refractive index, c – the speed of light, $\epsilon_0 = 8{,}85 \times 10^{-12}\mathrm{F/M}$ – the permittivity of free space, P_n – the polarization, ω_n – the angular frequency. The nonlinear response of a medium $\boldsymbol{P^{(2)}_n}$ acts as a source for new electromagnetic waves and appears on the right side of the equation. As mentioned before, for the generation of signal, there has to be satisfied the phase matching condition $\boldsymbol{k_3 = k_1 + k_2}$ together with the energy conservation law $\omega_3 = \omega_1 + \omega_2$. The phase velocities of created electromagnetic wave and the polarizing field, creating it, have to be the same.

From the Wave equation, new set of equations, describing the three-wave mixing can be written [51]:

$$\frac{\partial A_1}{\partial z} + \frac{1}{u_1}\frac{\partial A_1}{\partial t} + \frac{i}{2}g_1\frac{\partial^2 A_1}{\partial t^2} + \beta_1\frac{\partial A_1}{\partial x} + \frac{i}{2k_1}\nabla^2_{Trans}A_1 = -i\sigma_1 A_2^* A_3 \exp(-i\Delta k z),$$

$$\frac{\partial A_2}{\partial z} + \frac{1}{u_2}\frac{\partial A_2}{\partial t} + \frac{i}{2}g_2\frac{\partial^2 A_1}{\partial t^2} + \beta_2\frac{\partial A_2}{\partial x} + \frac{i}{2k_2}\nabla^2_{Trans}A_2 = -i\sigma_2 A_1^* A_3 \exp(-i\Delta k z),$$

$$\frac{\partial A_3}{\partial z} + \frac{1}{u_3}\frac{\partial A_3}{\partial t} + \frac{i}{2}g_3\frac{\partial^2 A_1}{\partial t^2} + \beta_3\frac{\partial A_3}{\partial x} + \frac{i}{2k_3}\nabla^2_{Trans}A_3 = -i\sigma_3 A_1 A_2 \exp(i\Delta k z); \quad (21)$$

Here $\omega_3 = \omega_1 + \omega_2$, u_n – the group speed, g_n – the GVD coefficient, β_n – the walk off angle, k_1 – the wavenumber. The second term of this equation describes the pulse propagation with a group velocity, the third term – dispersive elongation of the pulse, the fourth term gives the transverse mismatch due to anisotropy (double refraction) and the fifth one expresses the diffraction the beam. The term σ_n is the coefficient related to the nonlinear response of the material.

These general equations govern how each of the three electromagnetic fields behaves in the medium. Solutions of these equations express the spectral and temporal parameters, energy exchange between the interacting waves. As this is a really complicated task, the system of equations can be simplified depending on the situation.

4.5.3. Sum-frequency generation

In a very simplified case of a sum-frequency generation, when plane, monochromatic waves are considered without any dispersion or diffraction, and ω_1 is weak, while ω_2 is strong, the equation system can be written as [54]:

$$\frac{\partial A_1}{\partial z} = i\sigma_1 A_2^* A_3 \exp(-i\Delta kz)\,;\; A_2 = const;\;\; \frac{\partial A_3}{\partial z} = i\sigma_3 A_1 A_2 \exp(i\Delta kz)\,; \quad (22)$$

Solution of these equations shows the periodic exchange of the energy between the waves ω_1 and ω_3: [55]

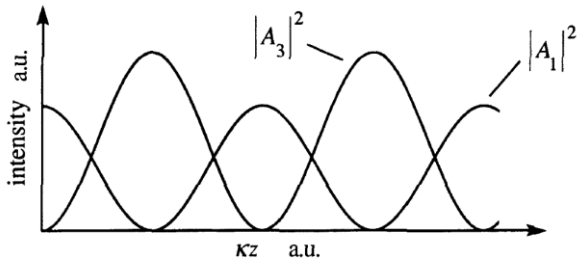

Figure 5. Variation of the intensities of the Signal and Upconverted waves in case of the perfect phase matching in the undepleted-pump approximation.

4.6. Third order nonlinearities

If the third order nonlinearities are taken into account and $P(t) = \chi^{(1)}E(t) + \chi^{(3)}E^3(t)$, the expression of $P^{(3)}(t)$ quickly becomes complicated, having up to 19 new frequency components [54] and other terms indicating new nonlinear phenomena. Generally, the third order nonlinearities, occurring in every media, are responsible for the Kerr effect and the four-wave mixing.

The Kerr effect, or the change of the refractive index depending on the intensity of the pulse $n = n_0 + n_{nl}I$, together with the Gaussian shape of the intensity, results in the self-focusing effect of the beams with an angle $\theta_{sf} = \sqrt{2n_{nl}I/n_0}$, after the critical Power $P_{cr} = \lambda/4\pi n_{nl}n_0$ is surpassed. Another result of the Kerr effect is the self-phase modulation due to the changing phase of the pulse $\varphi(t) = \omega_0 t - kLn(I)$. These phenomena are responsible for the spectral broadening of the pulse and the filament generation. The Four-wave mixing processes $\omega_1 + \omega_2 = \omega_3 + \omega_4$ lead to generation of a number of new frequency components.

The second order nonlinearity – sum frequency generation, was exploited in realizing this time-resolved measurement technique, while the third-order nonlinearities were observed in some of the recorded events, for example pulse broadening in a water medium.

5. Experimental setup

5.1. Laser setup and properties

The laser system used for the Femtosecond Camera setup consisted of Spectra-Physics oscillator *Tsunami* and the amplifier *Spitfire*. The Ti:Sapphire oscillator *Tsunami* was operating in the mode-locked regime emitting < 50 fs, 800 nm, 82 MHz pulse train. It was pumped by Spectra-Physics diode-pumped solid state laser *Millennia* emitting 4.1 W, 532 nm CW laser beam. Spectra-Physics Q-Switched Nd:YLF pump laser *Empower* delivered ~30 W, 527 nm, 1 kHz light and was used as the pump laser for the amplifier. Regenerative Ti:Sapphire based amplifier *Spitfire* used the Chirped Pulse Amplification technique and emitted a ~1.4 W, ~50 fs, 800 nm, 1 kHz pulsed laser beam which was guided to the Femtosecond Camera setup. The pulse duration was measured using the experimental TG-FROG setup [56][57] and also by the third-order autocorrelator *Tundra* from Ultrafast Innovations.

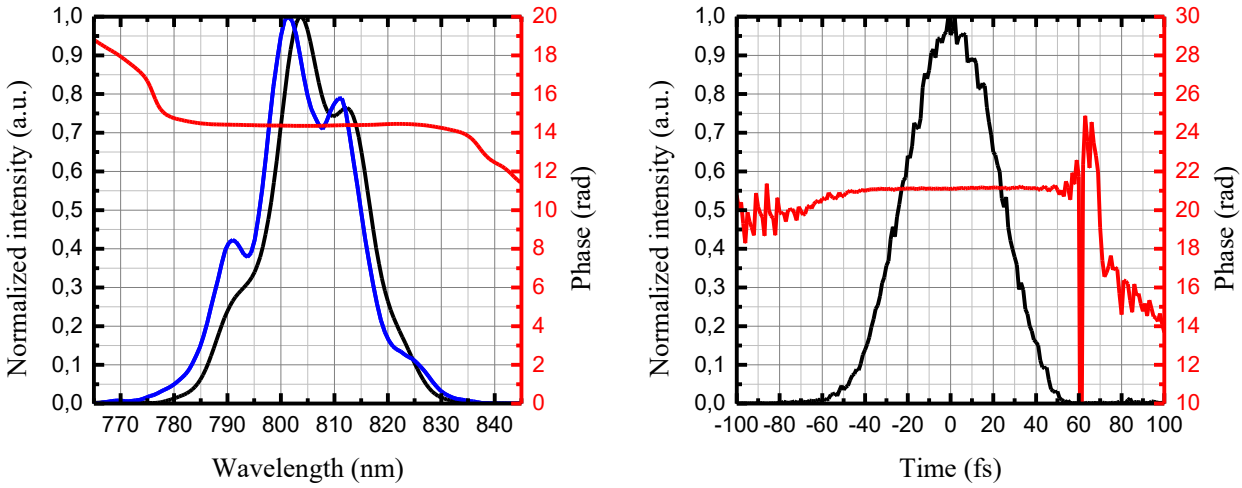

Figure 6. Measurement results of the pulse duration. On the left – retrieved spectrum (black) and the original spectrum (blue) are presented together with the retrieved phase (red). On the right – retrieved duration of the pulse (black) and the phase (red) of the pulse. Retrieved duration of the pulse is $\tau_{0.5} = 49.4 \pm 0.1$ fs.

The results of the measurement using *Tundra* autocorrelator confirmed the pulse duration to be $\tau_{0.5} \sim 50$ fs.

The power of the beam, before the Femtosecond Camera setup was measured to be $P_{av} \sim 1.2$ W. The diameter of the beam was $\omega_{0.5} \sim 5.63$ mm.

5.2. Experimental setup scheme

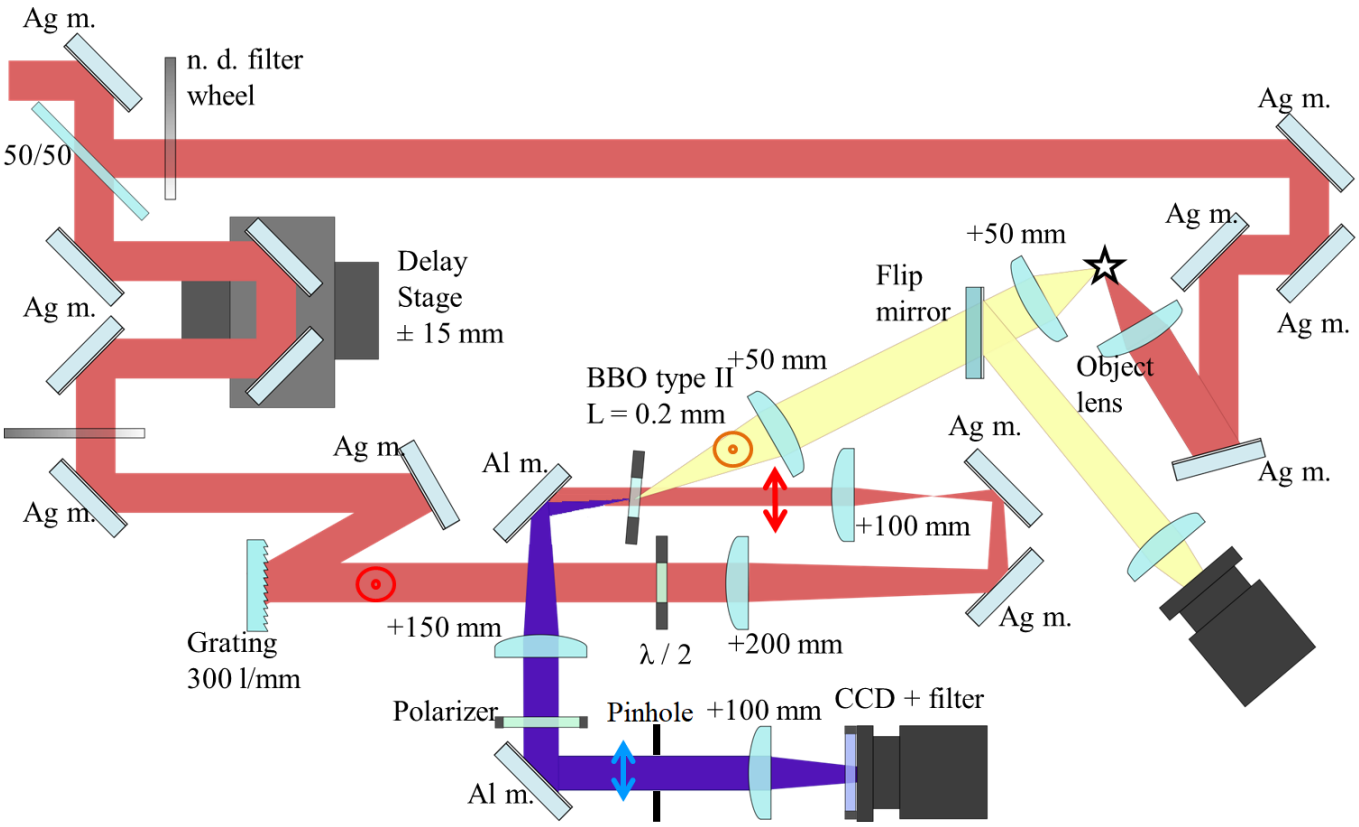

Figure 7. Scheme of the experimental setup.

The experimental scheme of the wide-field ultrafast femtosecond microscope setup or the Femtosecond Camera setup, based on the sum frequency generation, can be seen in the Figure 7. The pulsed beam, delivered by *Spitfire*, arrives at the setup and is divided by the 50/50 beam splitter into two paths – the Gate beam path and the Signal (or Object) beam path. The Gate beam path consisting of a delay stage, a grating and a telescope delivers the Gating pulse to the BBO crystal. The Object path is comprised of set of mirrors, an optional Object lens, a Signal collection telescope and an additional beam path with a second CCD camera. Through the Object path, the Pump pulse creates some sort of scattering or reflection event and the Signal pulse is collected and imaged on the BBO crystal, where the sum frequency generation of both pulses takes place. The Upconverted pulse is collected by the Collection path (blue) and imaged on the main CCD camera. Most of the unwanted light can be filtered out using spectral filters.

All of those beam paths are examined more in detail in the following chapters.

5.3. Gate beam path

The key elements of the Gate path are a delay stage, grating and a 4f telescope.

5.3.1. Delay stage

First of all, after the 50/50 beam splitter, transmitted part of the beam is directed to a set of silver mirrors mounted on Smaract SLC-2445 delay stage. The resolution of the stage is < 1 nm, while the range is ± 14.5 mm, which corresponds to ± 9.7 ps, keeping in mind that the distance traveled by the light is double the delay distance. Length of the delay stage determines a maximum duration of the event, which later is recreated from the captured image sequence.

The reflective variable neutral density filter was placed after the delay stage for controlling the power of the Gating beam. Then, the attenuated beam is directed by the silver mirror to the pulse front tilting module, consisting of a diffraction grating and a telescope.

5.3.2. Pulse front tilting

The need of tilted pulse front of the Gating pulse comes from the non-collinear geometry – angle between the Signal (scattered from the Object) and Gating beams. If the normal of the Gate pulse front envelope does not match the propagation direction of the Signal pulse, the time resolution is reduced. This happens due to the fact that different areas of the Gating beam arrive at different times, thus upconverts the Signal pulse at relatively different times as well. Also, the resulting image is distorted spatially, because the Gate and Signal pulses are overlaid spatially not consistently.

As mentioned before, the pulse front tilting could be achieved by using dispersive elements, as the pulse tilting is closely related with its angular dispersion.

5.3.2.1 Prism

In the first configuration of the Femtosecond Camera setup, the pulse front tilting was realized using the SF11 glass, 60° apex angle prism and the 5:2 demagnifying telescope.

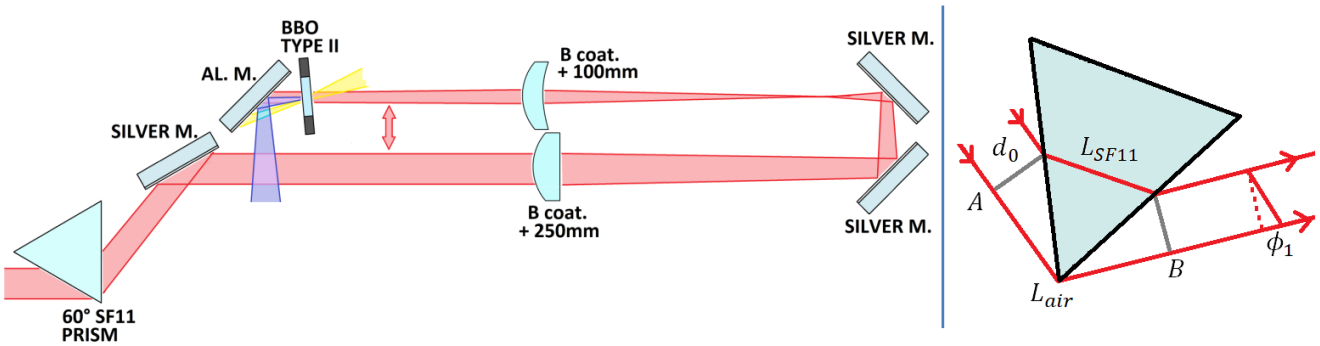

Figure 8. The pulse front tilting setup using prism and telescope on the left and the pulse tilting, using the prism, scheme on the right.

The pulse front tilt of the prism was calculated using relation [47]:

$$\phi_1 = \arctan\left(\frac{c\Delta\tau}{d_0}\right); \quad (23)$$

where $\Delta\tau = \frac{L_{SF11}}{v_g(\lambda)} - \frac{L_{air}}{c}$ (24) is the time difference of the group propagation times from line A to B; L_{SF11} – the beam path length inside the material; L_{air} – the beam path length in the air; $v_g(\lambda) = \frac{c}{n-\lambda(dn/d\lambda)}$ (25) – the group velocity [58]; d_0 – the diameter of the output beam. Calculated pulse front tilt of the SF11 prism was 5.596°. In this expression, the tilt angle is expressed through diameter of output beam for practical reasons. The tilt angle depends on the wavelength of the laser, the refractive index and the apex angle of the prism and incidence angle.

5.3.2.2 4f telescope

This pulse front tilt created by prism is relatively small and usually is adjusted using telescope, as telescope changes transverse magnification, but longitudinal length is still determined by the speed of light.

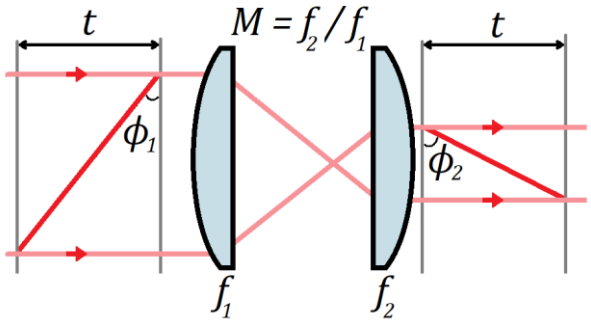

Figure 9. Principal scheme of the pulse front tilting adjustment, using the telescope.

Tilt angle ϕ_2 after the telescope can be calculated using [59]:

$$\tan(90 - \phi_2) = M \tan(90 - \phi_1). \quad (26)$$

Here ϕ_1 is the pulse tilt before the telescope, M – the magnification of the telescope. Telescope images the pulse front right after the prism on the BBO surface. This needs to be done with the 4f configuration telescope, due to the fact that several conditions besides the magnification have to be satisfied. First of all – the pulse needs to be imaged. As the tilting of the pulse is related to the angular dispersion, the pulse becomes spatially inhomogeneous, because different spectral components are directed towards different directions. Hence, the surface of a prism or a grating should be imaged on the crystal plane. That way all spectral components converge again. For example, collimation with a telescope using a negative lens could not be used, even if the correct magnification is chosen. The Beam would become inhomogeneous and the pulse – temporally dispersed.

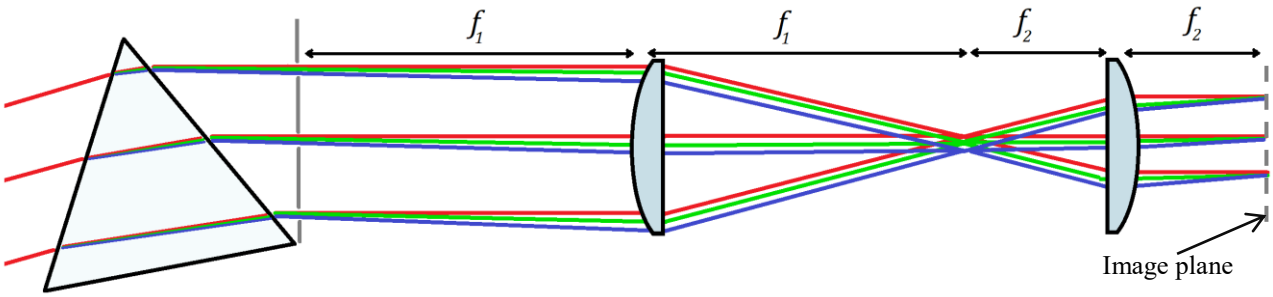

Figure 10. The principal scheme of a 4f imaging telescope. Surface of a prim (or a grating) is imaged on an image plane (which is the BBO crystal surface in the real experimental setup). All spectral components converge back to original spatial distribution.

Another issue is the need to keep similar divergence, hence imaging with only one lens should not be done. For example, in the Figure 11 it is seen that even if the magnification is correct and image of the pulse is formed on the object plane, beam has different divergence. In practice femtosecond pulse will be tilted, but also distorted as its transverse plane edges would be shifted relatively to the center of the pulse.

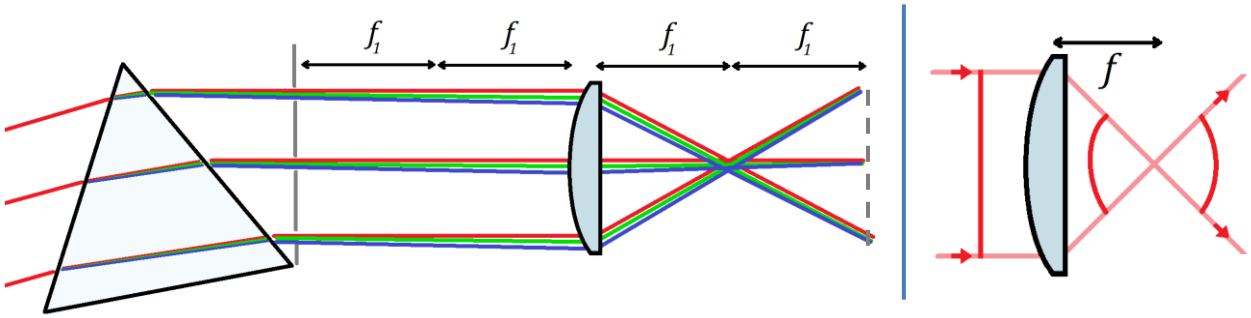

Figure 11. An example of incorrect imaging of the pulse. On the left – imaging setup using only a single lens. The prism plane is imaged 1:1, spectral components converge, but the divergence of the beam is lost. On the right – distortion of the pulse envelope, while traveling in a diverging beam path is presented. The ultrashort pulse is marked as a darker red line. After the lens, the pulse becomes C–shaped.

5.3.2.3 Prism dispersion

By using the telescope, the pulse tilt is increased as the beam size is decreased. This becomes an issue then thinking about the field-of-view (FOV) of the Femtosecond Camera. The FOV is determined by the size of the Gating beam on the crystal (or the clear aperture of the crystal itself) and by the magnification of the telescope, collecting the scattered light. This means that, by adjusting the pulse front tilt and reducing the beam size, FOV is decreased. A way to solve this problem would be increasing the beam size before the prism.

Larger beam size on the prism usually would cause severe issues due to the dispersion inside the prism. One side of the beam undergoes almost no material, while the other side – quite substantial amount of it. Effect increases with the increasing beam size and the pulse becomes more and more temporally broadened at one side of the beam. For example if the same SF11 glass, 60° apex angle prism is used with the 12 mm diameter beam, a L_{SF11} is ~26 mm which means that the 50 fs FWHM pulse broadens up to 275 fs (calculated using Labview *Lab2* module). This *spike* shaped pulse of course is not desired. This is the one of the reasons why gratings instead of a prism are used.

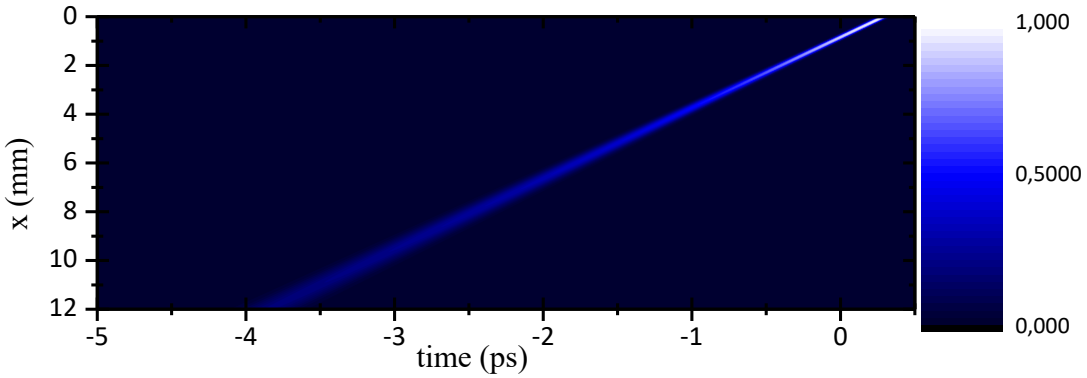

Figure 12. The shape of the pulse after SF11 glass, 60° prism. The Pulse is tilted and has a gradually increasing width over its transverse coordinate.

5.3.2.4 Grating

To remove the unwanted pulse elongation inside a prism, the pulse front tilting was achieved using the gold coated diffraction grating with 300 grooves/mm and blazed for 1 µm from Thorlabs. The gold coating was chosen to increase the reflectivity around the 800 nm wavelength range, as the reflection from the gold coating usually is > 95%. The aluminum coating on the other hand, gives reflection of roughly 75% at 800 nm. The pulse front tilt of the grating was calculated by using formula:

$$\tan(90 - \phi_1) = \frac{s}{Q + R} = \frac{\cos\beta}{\sin\alpha + \sin\beta} = \frac{\cos\beta}{mp\lambda_0}; \quad (27)$$

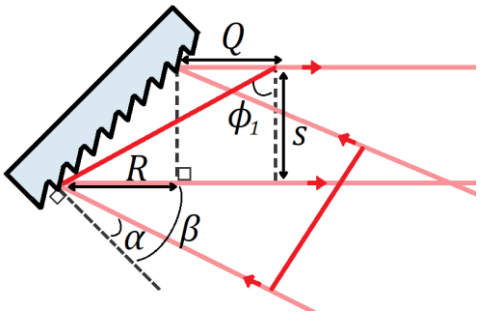

Figure 13. The principal scheme of the pulse front tilting using a grating [59]. Darker red lines mark the envelopes of the pulse.

In this expression s marks the diameter of the beam and the path difference between the different edges of the beam is $Q + R$. This can be expressed through the trigonometric functions of the beam incidence angle α and the diffracted beam angle β. Diffraction angle can be found if the incidence angle α, the diffraction order m, the groove density p and the central wavelength λ_0 of the pulse are known by the grating equation $mp\lambda_0 = \sin\alpha + \sin\beta$. For the 300 grooves/mm density grating, maximized for first order efficiency and 1 µm wavelength, and the input angle $\alpha = 17°$, the pulse front tilt was calculated to be $\phi_1 = 13.5°$.

Gratings are usually most efficient when used in the Littrow configuration, when the incident angle and diffracted angles are the same and the diffracted beam goes to the same direction where it came from. The efficiency also is highly affected by the polarization of the laser light. As both theoretical calculations and manufacturing reproducibility of the efficiency function of input angle and wavelength is hard task, it is recommended to measure the efficiency of the each grating. While this grating was not an ideal solution as the grating is most efficient at different wavelength, it was the best solution out of the standard stock and seemed to work quite well with very satisfactory efficiency $> 80\%$ (including reflection from metallic surface). For the comparison, the efficiency of an aluminum grating with same 300 grooves/mm, would have been $< 70\%$.

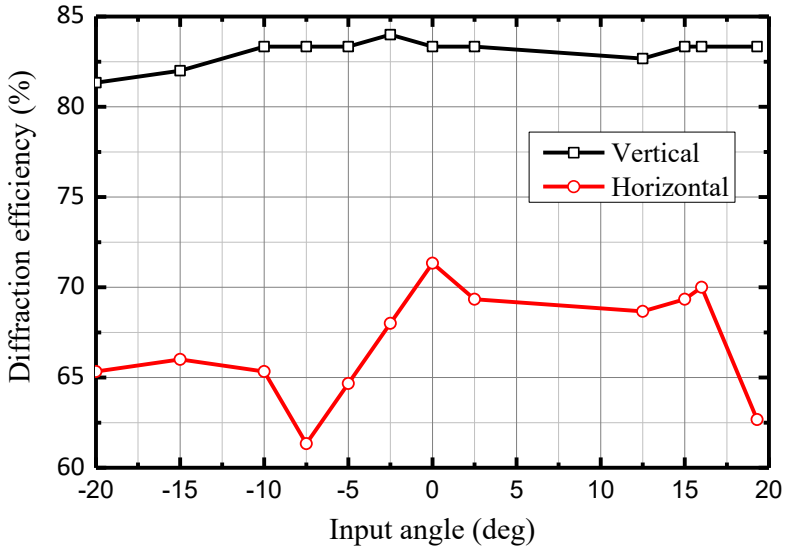

Figure 14. The measured efficiency of the grating.

5.3.2.5 Tilt inside material

Using the grating together with the 2:1 demagnifying 4f telescope, 25.65° tilt angle was achieved at the surface of the BBO crystal. As a tilted pulse enters the material, tilt angle is again changed, due to the pulse front propagating through the different mediums (air and BBO) at the same time. Derived formula for calculating the tilt inside the material after refraction can be used:

$$\tan(\phi_m) = \tan(\beta_m) - \frac{v_g(\lambda)}{c}(\tan(\alpha_m) - \tan(\phi_1)); \quad (28)$$

Here ϕ_m is the tilt angle inside the material; α_m – the incidence angle; β_m – the propagation angle inside the material found from the Snell's law $\sin(\alpha_m)\, n_{air} = \sin(\beta_m)\, n_m(\lambda)$; v_g – the group velocity; ϕ_1 – the tilt angle outside material. The refractive index $n_m(\lambda)$ in this case is $n_{BBOe}(\lambda, \theta)$. In this particular configuration was $\phi_{gate} = \phi_m \approx 17.1°$. This tilt angle inside the material should be the same as the angle between the propagation directions of the Gate and Object beams (if Object pulse tilt is negligible). If this is true, the pulse fronts of the Gate and the Object are matched and best time resolution of the Femtosecond Camera is achieved.

5.3.3. Sum frequency generation

After pulse the front tilting module, the Gating pulse arrives at the nonlinear BBO type II crystal, where it overlaps with the Signal pulse and the upconverted pulse is generated. This step is the main part of the Femtosecond Camera setup. The two main goals were pursued. First one is to increase the signal-to-noise ratio as much as possible. Second one is to keep the time resolution of the optical shutter as high as possible. When designing the sum frequency generation experiment, there are a lot of variables that can be chosen. For example – a material of the crystal, a type of the crystal, a cutting angle θ, a coating of the crystal, a length of crystal and an interaction geometry: collinear or non collinear. If a non collinear geometry is chosen, another variable is an angle between the Gate and Object Signal pulses. In the Femtosecond Camera setup, the sum frequency generation was done using the 0.2 mm thickness, BBO type II crystal with $\theta = 42.4°$. The angle inside the crystal between gate and object beams was $\alpha_{up} \approx 17°$ (outside the crystal, the angle $\alpha_{up'} \approx 30°$). The crystal was coated with single 90 nm thickness MgF_2 layer coating (the transmission centered at 500 nm). Such coating was chosen to decrease the reflectivity more or less equally near the wavelengths of the laser and its second harmonic. The reflectivity was calculated to be $R = 1.675\%$ @ 400 nm and $R = 2.175\%$ @ 800 nm. It was calculated using the Fresnel equations and the Interference equation:

$$R_{12} = \left|\frac{n_1 - n_2}{n_1 + n_2}\right|^2;\ R_{23} = \left|\frac{n_2 - n_3}{n_2 + n_3}\right|^2; \quad (29)$$

$$R = R_{12} + R_{23} + 2\sqrt{R_{12}R_{23}}cos(\varphi_{diff}); \quad (30)$$

The Indexes $1, 2, 3$ mark the air, coating and substrate mediums; R – the reflected intensity; n – the refractive index, φ_{diff} – the phase difference between the waves reflected from the coating and the substrate. The Phase difference is a function of wavelength, the coating thickness and the refractive index of the coating material.

The non collinear sum frequency generation was implemented in the setup with a purpose to have the spatial separation between the upconverted, Gate and Object beams. This helps increasing the signal-to-noise ratio, as a huge amount of unwanted light can be blocked using the pinhole placed after the crystal and choosing the only upconverted beam. For example, if the spectrum of the scattered light from the Object is partially overlaid with the spectrum of the upconverted Signal, spectral filters can't remove the background. Another advantage of a non collinear geometry is ability to compensate the group velocity mismatch.

The second type of interaction $eo - e$ was chosen to reduce the background generated by the Gate pulse. In this case, the crystal is cut in such manner, that the phase matching condition $\Delta\boldsymbol{k} = \boldsymbol{k_1} + \boldsymbol{k_2} - \boldsymbol{k_3} = 0$ is satisfied by the first and second waves being in different polarizations. In this setup, the Gate beam had an extraordinary polarization, while the Signal was made an ordinary one. Two photons of different polarizations are needed for a sum frequency generation so probability of the unwanted second harmonic generation significantly drops, because almost all of the Gate pulse photons are polarized in the same way. This is verified by comparing the images of the same Object taken with the experimental setup using the type I and type II crystals:

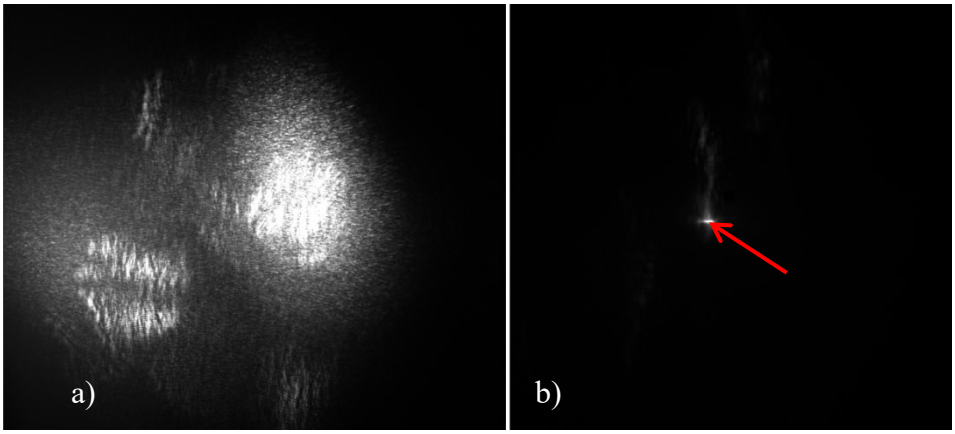

Figure 15. Background noise comparison between time-resolved images captured using Type I (a) and Type II (b) BBO crystals.

The Upconverted Signal in these pictures is the scattered light from the plasma filament in the air. The plasma can be seen in the picture b) as a small white dot and it is marked by the red arrow. Bandpass for 400 nm filter was placed before the CCD camera. Integration time of the camera integration was 221 ms. Power of the Pump beam, scattering from the Object $P_{pump} \approx$ 17 mW, while the Gate beam power in a) $P_{gate} < 1$ mW and in b) $P_{gate} \approx 27$ mW. It can be seen easily that the background noise in the Type II interaction is significantly smaller, while no sum frequency signal can be seen in the picture a). In fact, background noise generated during the Type II interaction is generally weak and limits SNR only when the weakly scattering targets are chosen.

5.3.3.1 Background noise

Talking about the background noise, like shown above, experimentally it is observed that some second harmonic, even though it is significantly less, is still being generated while using the Type II crystal. This background has the same polarization and wavelength (400 nm) as the Upconverted beam (if the scattered light from the Object is also 800 nm, like the Gate beam). Also it could not be filtered out spatially, as it is most likely scattered in all directions, from the defects of the crystal or the dust on this surface. This background noise is a combination of several different aspects and originates from Gate beam.

First of all, the Gate beam could have slightly impure polarization with a small projection to the ordinary axis of the crystal. Then the $eo - e$ interaction is possible, even though not efficiently, as the crystal is in position of satisfying the phase matching for the sum frequency of the Gate and the Signal, not for the type II second harmonic generation of the Gate pulse. To reduce this effect, additional polarizer was placed in the Gate beam, but no drastic change was observed, as the polarization of the laser beam was pure enough.

Another issue – the partial satisfaction of other phase matching angles. During the experiment, the crystal was rotated to satisfy the phase matching for the sum frequency of the Object and Gate beams. But this does not guaranty that all of the incoming light satisfies only this phase matching condition. Some of the incoming Gate beam light could be scattered from the surface of the crystal. Also beams fundamentally have a set of **k** vectors – the beam is diverging or converging. This means that part of incoming photons could potentially partially satisfy the other phase matching angles – for example earlier mentioned $eo - e$ second harmonic generation, as well as other types of interaction. The acceptance angle of the phase matching has an inverse proportion to length of the crystal: $\Delta\theta \sim \frac{1}{L}$, which means that a thicker crystal should reduce the acceptance angles of the unwanted interactions and thereby increase the signal-to-noise ratio.

Last issue is the surface generated second harmonic, which happens on the surface of material, where there is no centrosymmetry. This was tested experimentally by replacing the BBO crystal with a glass plate and observing some second harmonic noise background. Thereby, the Femtosecond Camera setup is sensitive enough to detect the second harmonic being generated only from surface, which means that potentially this background noise is another factor reducing the SNR. The surface second harmonic generation should be independent from the thickness of the crystal, so a thicker crystal should have higher signal-to-noise ratio.

This second harmonic light is scattered by the crystal and part of it is collected and imaged together with the wanted upconverted laser beam on the CCD camera. As this background noise can't be filtered out spatially, spectrally or using polarizers, other ways of improving the

signal-to-noise ratio should be found. For example, a higher surface quality crystal could potentially reduce the scattering of this parasitic second harmonic.

The other types of the background noise which could come from the scattered light from the Object, can be filtered out using polarizers and spectral filters.

5.3.3.2 Improving signal-to-noise ratio

One of the options for improving the signal-to-noise ratio was to increase the crystal length. The results can be seen in the Figure 16 and Figure 17. To test the ratio dependency on the thickness of the crystal, the sum frequency was generated with the 4 BBO type II crystals of different thickness. The object was chosen to be the air plasma and the scattered laser light from it could be observed. The Signal-to-background noise ratios were calculated for the mean (over area in the each picture) and for the peak values. As it was expected, a longer crystal improved signal-to-noise ratio.

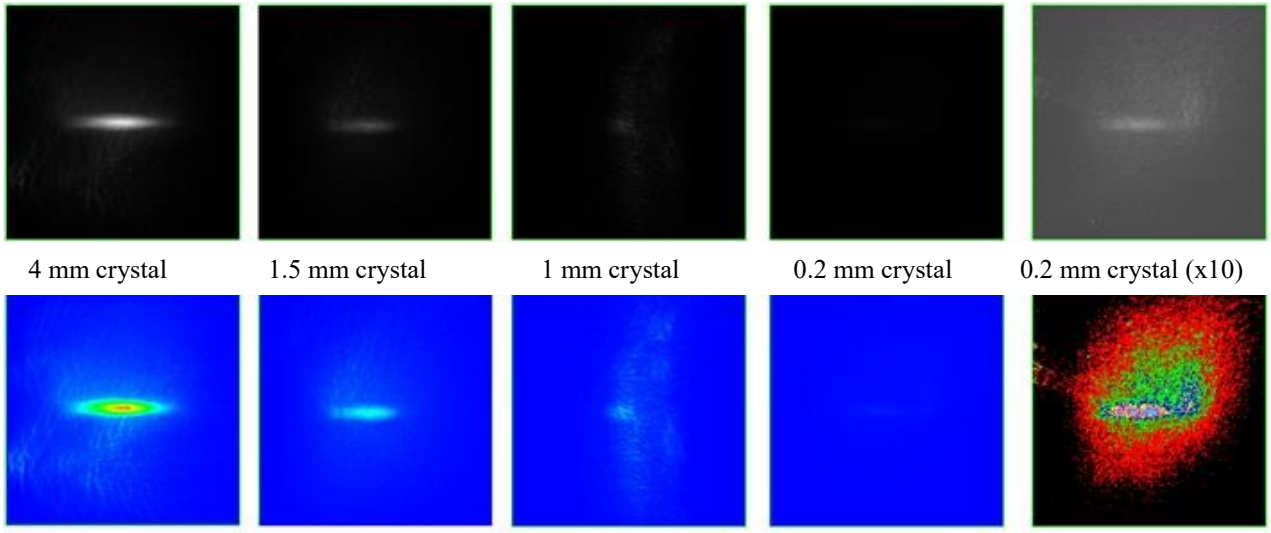

Figure 16. The air plasma scattering pictures captured using BBO Type II crystals of different thicknesses. Upper row – greyscale, lower row – „temperature“ color scale. The mean and peak background values were recorded by covering the Object beam path. The mean value calculated by integrating signal over confined area, visible in the pictures.

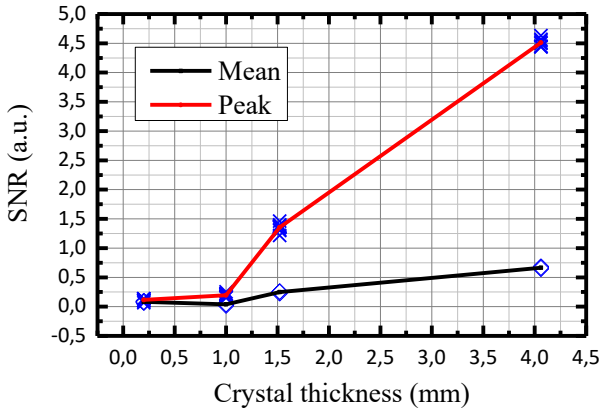

thickness	mean	peak
0.2 mm	0.083	0.115
1 mm	0.038	0.194
1.5 mm	0.249	1.354
4.5 mm	0.666	4.511

Figure 17. The signal-to-background noise ratio dependency on crystal thickness.

Another way of having the higher SNR is to increase the Signal by collecting more light. More detailed overview of arising problems is presented in the Collection path description.

Finally, last way to increase the SNR is to reduce the Gate beam power, as the background noise comes only from the Gate beam while the Upconverted light is being generated by the Gate and Object beams both. Hence $I_{2H} \sim I_{gate}^2$ and $I_{up} \sim I_{gate} I_{obj.}$, so the background noise drops quadratically with the Gate intensity, while the Upconverted Signal decreases only linearly. This is not an ideal solution because the power of the Upconverted Signal drops as well. Then, either longer integration times of CCD camera are needed (and the thermal noise increases and experiment gets more complicated due to longer recording times), or magnification needs to be decreased to keep same intensity on the CCD camera, thus reducing the spatial resolution.

Worth mentioning is that the background noise is quite weak compared to any scattered light from surfaces, defects or strongly scattering medium like water etc. The background noise becomes an issue (or even a serious problem) when trying to observe weakly scattering Objects like the air plasma scattering, the bulk medium scattering and so on.

5.3.3.3 Calculation of sum frequency conversion geometry

As it was shown, a thicker crystal is good for a better signal-to-noise ratio. The drawback of using a longer crystal is a decreased time resolution. This happens because of several reasons. The first one is a dispersion of the Gate and Object pulses, although this factor is not the main factor, because elongation of the 50 fs FWHM pulse through a 4 mm BBO crystal is relatively small: the duration of the o polarized pulse becomes ~52.7 fs, while the duration of the e polarized pulse ~51.1 fs; which is negligible.

The major contributing factor, reducing time resolution is a group velocity mismatch between the Gate pulse and scattered light from the Object. Temporal distortions of Upconverted pulse do not matter, as pulse is being integrated by the CCD camera.

One way of compensating GVM is choosing correct angle α_{up} between Gate and Object pulses. Of course, phase matching condition still has to be satisfied. Then it is needed to find angles θ_G and α inside the crystal, which satisfy both phase matching and GVM compensation conditions.

The refraction indexes for both the ordinary and extraordinary waves were calculated by using the Sellmeier Equations (here wavelengths are in micrometers):

$$n_o^2 = 2.7359 + \frac{0.01878}{(\lambda^2 - 0.01822)} - 0.01354\lambda^2; \quad (31)$$

$$n_{e,0}^2 = 2.3753 + \frac{0.01224}{(\lambda^2 - 0.01667)} - 0.01516\lambda^2; \quad (32)$$

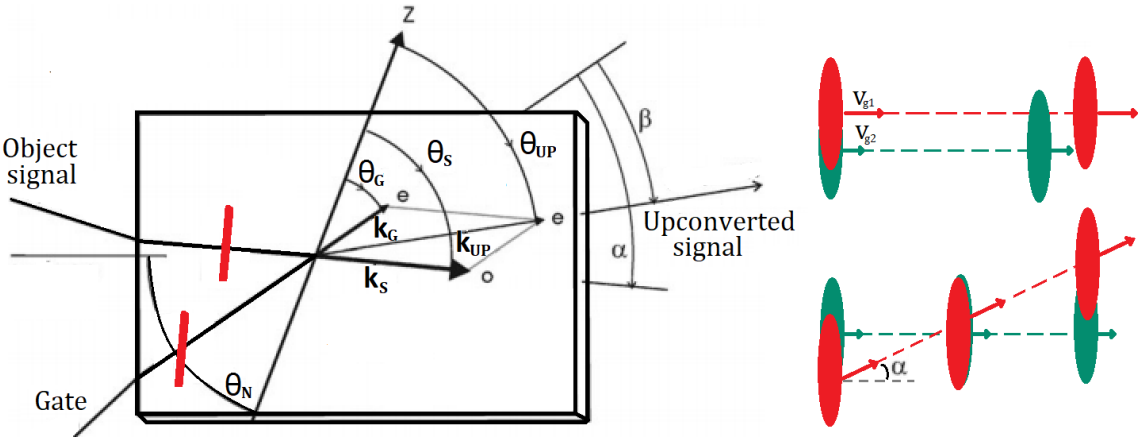

Figure 18. Interaction geometry for the sum frequency generation with Type II phase matching and tilted pulses on the left [47]. On the right – the principal scheme of the non collinear geometry compensated GVM [54].

As a BBO crystal is birefringent, n_e is not only a function of the wavelength, but also a function of the propagation angle θ relative to the crystal axis. This dependency can be calculated using the formula:

$$n_e(\theta) = \sqrt{\frac{n_{e,0}^2 n_o^2}{n_{e,0}^2 \cos^2\theta + n_o^2 \sin^2\theta}} = n_o \sqrt{\frac{1+\tan^2\theta}{1+\left(n_o/n_{e,0}\right)^2 \tan^2\theta}}; \quad (33)$$

The perfect phase matching condition is $\boldsymbol{\Delta k = k_1 + k_2 - k_3 = 0}$. The wavenumber, or the magnitude of the wave vector can be written as $k = |\boldsymbol{k}| = \frac{2\pi}{\lambda_n} = \frac{2\pi n}{\lambda_0}$; Then the addition of vectors $\boldsymbol{k_s + k_g}$ generates a new vector $\boldsymbol{k_{up'}}$ with its magnitude equal to:

$$k_{up'}^2 = k_s^2 + k_g^2 + 2k_s k_g \cos(\alpha); \quad (34)$$

The angle of newly generated $k_{up'}$ relative to the crystal axis can be expressed as:

$$\tan(\theta_{up}) = \frac{k_g \sin(\theta_g) + k_s \sin(\theta_s)}{k_g \cos(\theta_g) + k_s \cos(\theta_s)}; \quad (35)$$

Since the angle θ_{up} is known, the $|k_{up}|$ can be calculated. Then, the phase matching condition can be rewritten as:

$$\boldsymbol{k_{up'}}(\theta_g, \alpha) \equiv \boldsymbol{k_s} + \boldsymbol{k_g}(\theta_g) = \boldsymbol{k_{up}}(\theta_{up}); \quad (36)$$

By solving this equation, angles θ_g and α, which satisfy the phase matching condition, can be found. The geometry of interaction should also compensate the group velocity mismatch between the Gate and Object pulses. A principal scheme of the GVM compensation is shown on the Figure 18 – projection of the Gating pulses group velocity vector should match the group velocity

of the Signal pulse. The time difference between the Gate and Signal pulses generated by GVM over the length L can be written as [47][60]:

$$\tau_{diff} = L\left(\frac{1}{v_{gr}(\lambda_s)} - \frac{1}{v_{gr}(\lambda_g, \theta_g)\left(\frac{\cos(\alpha-\rho)-\tan(\varphi_s)\sin(\alpha-\rho)}{\cos(\rho)}\right)}\right); \quad (37)$$

In this equation, v_{gr} is the group velocity, α – the angle between the Pump and Signal beams, ρ – the birefringent walk-off angle, φ_s – the tilt angle of the signal beam. The tilting of the Signal beam arises from the fact that the Signal beam hits BBO crystal and refracts, which gives tilting of pulse front and can be calculated using the equation:

$$\tan(\phi_m) = \tan(\beta_m) - \frac{v_g(\lambda)}{c}(\tan(\alpha_m) - \tan(\phi_1)); \quad (28)$$

In the equation above, the Gate pulse is assumed to be tilted by $\varphi_g = \alpha + \varphi_s \approx \alpha$ if φ_s is small. After the tilting, the Gate pulse envelope and matches Pulse envelope of the Signal pulse. Ideally $\tau_{diff} = 0$ but practically $\tau_{diff} \leq \tau_{gate}$ is enough.

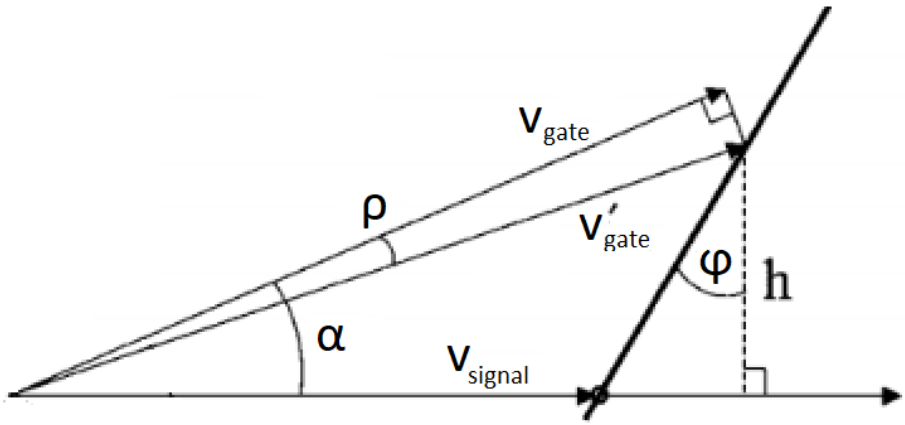

Figure 19. Principal scheme of a group velocity projection of a tilted pulse. The gate pulse is being projected on to the signal pulse [60].

The birefringent walk-off angle, or the angle between the propagation axis and the Pointing vector can be calculated using [61]:

$$\rho = \frac{-1}{n_e(\theta)}\frac{dn_e(\theta)}{d\theta}; \quad (38)$$

The angle θ is an angle between the propagation direction and the axis of a crystal. The minus sign notes that the walk-off occurs in a direction, where the refractive index is decreasing.

All the angles used in equation above θ_g, θ_s, θ_{up} are the angles of propagation relative to the crystal axis z. Angles relative to the surface can be found by knowing θ_N – the cutting angle of the crystal. Calculating the angles of incidence can be done by using the Snell's law.

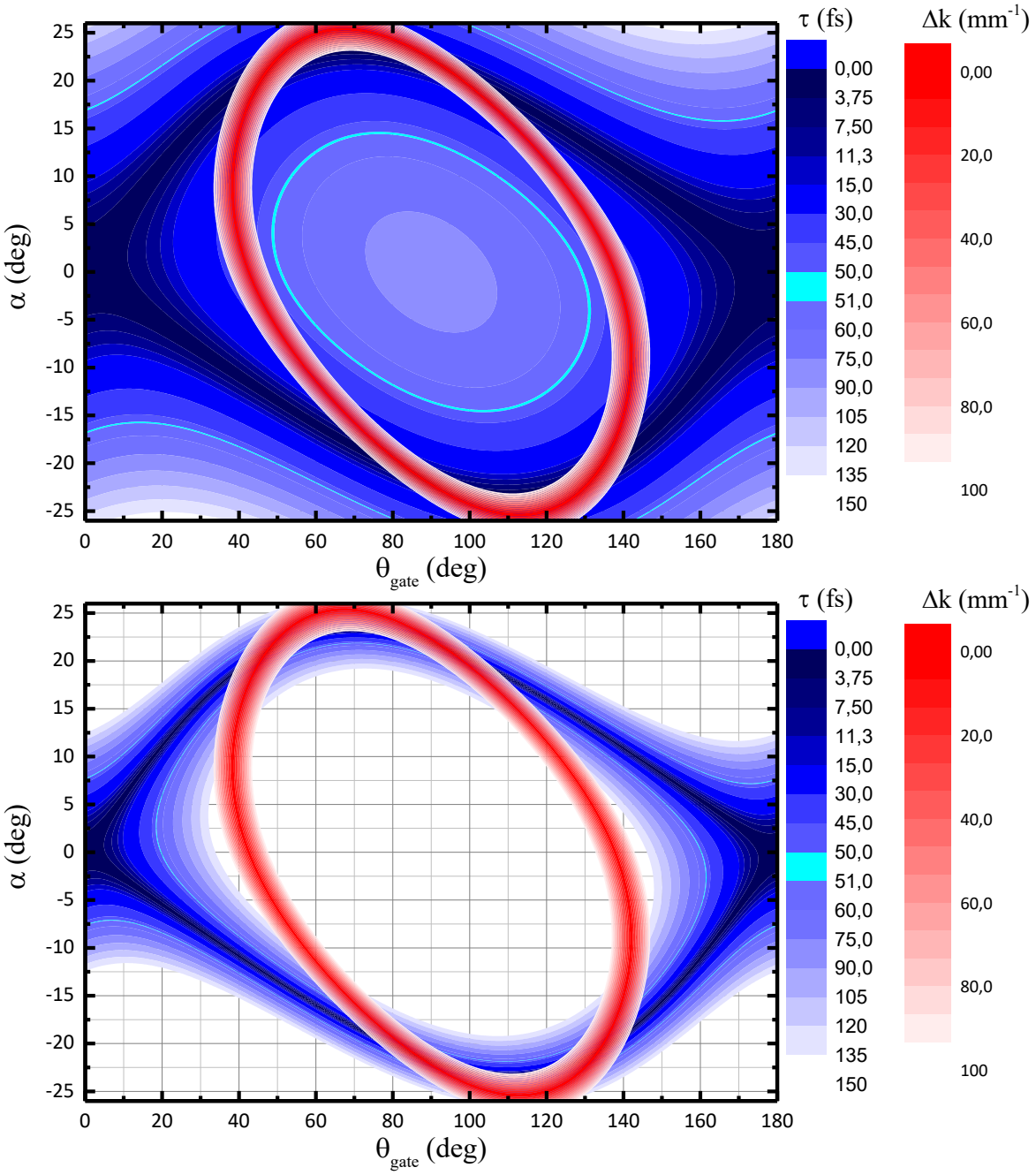

Figure 20. The time difference due to the GVM and the phase matching dependencies on the Gate and Signal beam geometries. Upper graph crystal length = 0.2 mm; lower length = 1 mm.

Using Labview, these equations were solved numerically and the θ_g and the α angles that satisfy $\tau_{diff} \leq \tau_{gate}$ and $\boldsymbol{k_s} + \boldsymbol{k_g}(\theta_g) = \boldsymbol{k}_{up}(\theta_{up})$ were calculated. It is important that τ_{diff} is also a function of the pulse front tilt of the Signal. If the incident angle of the Object signal beam is large, the tilt can't be neglected and a solving algorithm becomes more complicated. One option is to include a feedback loop to fix the solutions θ_g and α, as φ_s become known only when the θ_g and α are known. Another way is to add an additional dimension changing φ_s.

Results of the calculations are presented in Figure 20. Red curve is the phase matching curve. Blue – the time difference between the Gate and Signal pulses after 0.2 mm and 1 mm of the

crystal. Ideally there are 4 solutions, where the blue and red curves coincide. On those points there is a perfect phase matching and no group velocity mismatch. Higher the acceptance of the time difference is allowed – wider the region of the blue line is acceptable. Also it is seen that if the crystal is 0.2 mm thickness, almost in all region of the phase matching, time difference is less than 50 fs. On the other hand, if thicker crystal would be used, overlap region between the phase matching and the GVM compensation is much smaller.

Since the θ_g and α angles are the inside angles, the real incidence angles depend on the crystal cutting angle as mentioned before. Usually BBO crystals are cut in region of $22-45$ deg. for effective Type I or Type II second harmonic generation. The crystal used in this setup was cut in 42.4 deg angle. This means, that usable angles of θ_g for the non collinear geometry sum frequency generation were only around $\sim 45-50$ deg.

The ideal geometry satisfying both GVM compensation and the phase matching was calculated to be $\theta_g \approx 47$ deg; $\alpha \approx 21$ deg; $\theta_N \approx 56$ deg. Then, the incidence angles of the Gate and Signal beams are relatively small, do not introduce an additional pulse front tilt and even a a 4 mm crystal does not create a larger mismatch than 50 fs between the Pump and Signal pulses.

Due to unavailability of the crystal cut in $\theta_N \approx 56$ deg, the crystal with $\theta_N = 42.4$ deg, $L = 0.2$ mm was used to increase the temporal resolution as much as possible. The angle between the Signal and Gate was chosen to be $\alpha \approx 17°$ with a purpose to be closer to the minimum GVM. Crystal was rotated to achieve the phase matching.

To test these calculations, the sum frequency of the Gate pulse and Signal pulse, which was reflected from silver mirror, was observed. The generated sum frequency signal was strong and spatially not distorted. By changing the delay between the Pump and Object Signals, intensity of the sum frequency was changing, but no spatial beam movement was observed as expected. The Gate pulse was tilted to match the Signal pulse front successfully. The temporal resolution of the Femtosecond Camera was later measured to be same as the original Gate pulse duration.

5.4. Signal beam path

The signal beam path is relatively simple compared to the Gate beam path. It consists of 3 modules – the pump module, the imaging module and the unresolved time imaging beam path.

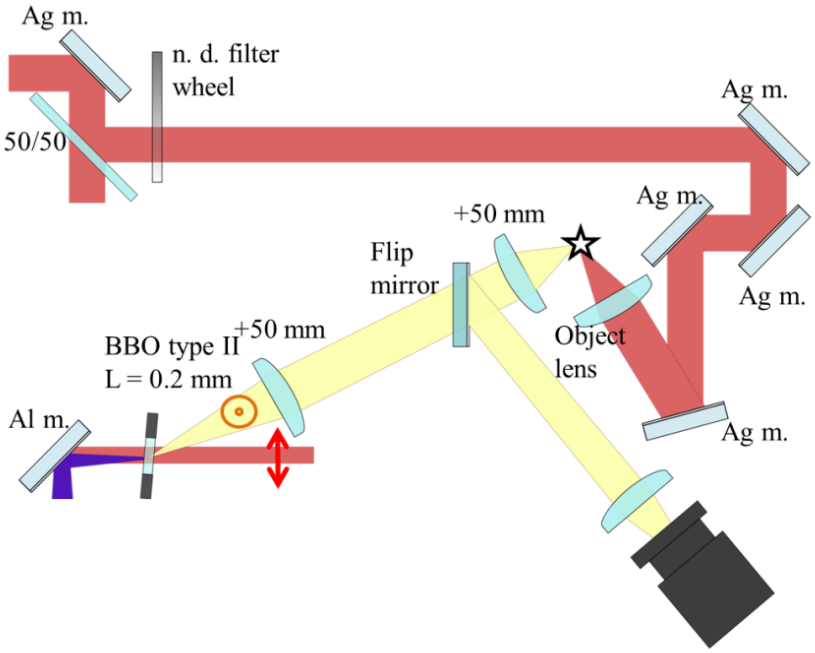

Figure 21. Part of main experimental setup – signal beam path.

5.4.1. Pump module

The elements of the pump module were a continuously variable ND filter OD: 0 - 2.0, a set of silver mirrors, creating the same length beam path as the Gate beam path, nd focusing optics. The reflectivity of silver mirrors was $\sim 95 - 98\%$ @ 800 nm depending on the incidence angle. A number of targets were chosen as the observable objects – a resolution test target, an air plasma, a glass surface, a sapphire, a cuvette filled with water, etc. They are reviewed more in depth in the Results chapter. Either one of the two different lenses (or no focusing element at all) was placed before the object of interest. The beam diameter near the focusing element was ~5.63 mm FWHM.

The focusing element was either a $f = 75$ mm, $d = 25.4$ mm, $R < 0.5\%$ @ 800 nm, fused silica, B-coated plano-convex lens or a M-10X Newport objective with 0.25 NA, $f = 16.5$ mm, $d = 7.5$ mm and $T \sim 90\%$ @ 800 nm. The placement of the each lens or objective was adjusted accordingly, depending on the exact object of interest.

The spatial beam parameters can be approximately estimated using the formulas:

$$\omega_{1/e^2} = \frac{\omega_{FWHM}}{\sqrt{2\ln(2)}}; \quad (39)$$

$$\omega'_{1/e^2} = \frac{\omega_{1/e^2}}{\sqrt{(1+s/f)^2 + (z_R/f)^2}}; \quad (40)$$

$$z_R = \frac{\pi \omega^2{}_{1/e^2}}{M^2 \lambda}; \quad (41)$$

Here ω_{1/e^2} is the radius of the beam at the $1/e^2$ maximum intensity level, ω_{FWHM} – the diameter of the beam at the 0.5 maximum intensity level, s – the beam waist distance to the lens, f – the focal length, ω'_{1/e^2} – the radius of the beam after the focusing lens; z_R – the Reyleigh length; M^2 – the quality parameter.

As mentioned before, the duration of the Pump pulse was $\tau_{FWHM} \approx 50$ fs. The repetition rate $R_{rep} = 1$ kHz and the maximum averaged power of the Pump beam before the focusing element was $P_{max} \sim 0.6$ W.

By knowing pulse the duration τ, the radius spot size ω_{1/e^2}, the averaged power P and the repetition rate R_{rep}, the energy E and the peak intensity I_{peak} of the pulse can be found:

$$I_{peak} = \frac{P_{peak}}{S} = \frac{E}{\tau S} = \frac{E}{\tau \pi \omega^2} = \frac{P_{vid}}{R_{rep} \tau \pi \omega^2}, (42)$$

where P_{peak} – the peak power, S – the area.

5.4.2. Imaging module

The Imaging module consisted of a 1:1 confocal telescope constructed using two $f = 50$ mm lenses. The light from the Object, either scattered or reflected, was collected by one of the lenses and collimated. As the pump beam is polarized vertically, the scattered light is also mostly vertically polarized. The collimated light was collected by the second lens and object was imaged on the BBO crystal surface.

The focus lengths of the lenses were chosen mainly to have desired FOV, as FOV depends on size of Gate beam (together with clear aperture of crystal) and the magnification of the Imaging module. The One to one magnification setup seemed satisfactory for the wide variety of the observable objects.

The between the Signal and Gate beams was made to be $\alpha_{input} \approx \sim 29$ deg, so that inside the BBO it was $\alpha \approx 17$ deg.

5.4.2.1 Light collection efficiency

From the signal-to-background noise point of view, higher NA lenses should be used to collect more light and thereby increase the signal strength. Four elements – a 50 mm lens, a 35 mm lens, a reflective objective Thorlabs LMM-40X-P01 with a focal length $f = 5$ mm and also a reflective objective Newport 50102-02, with the focal length $f = 5.4$ mm were compared to see how much light each of the elements would collect. The Thorlabs and Newport reflective objectives were chosen, as reflective optics is generally good option, when short or potentially event shorter pulses are involved. As the pulse does would not go through any medium, no dispersion would be introduced – the pulses do not experience temporal broadening. Also, the objectives are chromatic aberration free. Calculations were made assuming a point source emitting a half-sphere of the light (which was considered to be 100%). Then the light percentage collected by the lens or objective is $1 - \cos(\alpha')$. The results are presented in the table below. The total amount of the collected light by the objectives is calculated including obstruction (a second mirror blocking the first mirror) and a light (800 nm,) reflection from the 2 mirror surfaces (the silver coating for objective from Thorlabs and the aluminum coating for the objective from Newport, as they do not offer silver coated mirrors).

Item	NA	α (deg)	Obstruction	Collected light	Collected light after obstruction	Total collected light
Lens (B coated) F = 50 mm; D = 25.4 mm	0.246	14.25	0 %	3.1 %	3.1 %	3.05%
Lens (B coated) F = 35 mm; D = 25.4 mm	0.34	19.94	0 %	6 %	6 %	5.94 %
Thorlabs LMM-40X-P01	0.5	30	22 %	13.4 %	10.45 %	9.83 %
Newport 50102-02	0.52	31.33	~25.4 %	14.58 %	10.87 %	6.28 %

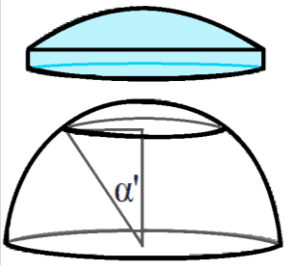

Table 1. The calculation of the collected light efficiency using different optics.

Using the reflective objective helps to collect ~3 times more light than the 50 mm lens, or ~1.65 times more light than the 35 mm lens. On the other hand, higher NA practically means the shorter focal length. If the focal length gets shorted, by wanting to keep same or similar magnification, the second focusing lens of the imaging module has to have a similar focal length. Hence, the distance between the BBO crystal and the second imaging lens decreases, which is not good, as the angle α between the Signal and the Gate is determined by other factors, mentioned before. Also, a large beam incidence angles are generally not desirable. Firstly, if the incidence angle of the Signal on the crystal is large, as mentioned in previous chapter, the Signal pulse experiences an unwanted additional pulse front tilt. Another issue is the decreasing effective

interaction length between the Gate and Signal pulses inside the crystal. Finally it's generally harder to work with the large angles, as the projection of the crystal to the beam gets smaller and the Signal beam can easily hit the side wall of the crystal. Analogously if the Gate beam hits side wall of the crystal, an enormous amount of light is being scattered and parasitic second harmonic background can easily be generated,

5.4.2.2 Signal upconversion method

The one solution of having a higher NA collection lens together with a small magnification, is upconverting not the image of the object, but a rather a collimated beam, or even a Fourier plane of the image. Then, only one lens is placed in between the object and the BBO crystal. The light from the object is collimated and directed towards the BBO. Both of these configurations – image upconversion [45] and Fourier plane upconversion [62][49][63] are used for the image upconversion and each of them have their own unique traits.

If the Fourier plane of the Object is imaged on the crystal, the Gate beam acts like a spatial filter. The center of Gate beam upconverts the lower spatial frequencies of the object, while edges of Gaussian Gate beam upconvert the higher spatial frequencies. This results in reduced sharpness of the image, as higher spatial frequencies are upconverted with lower efficiency. The larger Gate beam diameter or even the larger BBO crystals are required to have full overlap of the Gate and Signal pulses and high spatial resolution. Furthermore, the angular acceptance of the crystal limits the maximum size of the image, as a larger object means larger incidence angles on the crystal.

When the image plane of the object is upconverted, the maximum size of the image depends on the Gate beam diameter, while the resolution is limited by the angular acceptance of the crystal. The thinner the crystal is – the wider the angular acceptance, thus the better spatial resolution. The image is upconverted in a sense more uniformly, following a Gaussian beam distribution of the Gate pulse.

To decide which upconversion method is better for implementation in the Femtosecond Camera setup is too early, as due to lack of time only image plane upconversion has been tested. The main motivation of trying the collimated beam upconversion would be to replace the 50 mm lens with a high NA objective. Also it should be noted that upconverting a collimated beam may not be the same as upconverting an image at its Fourier plane.

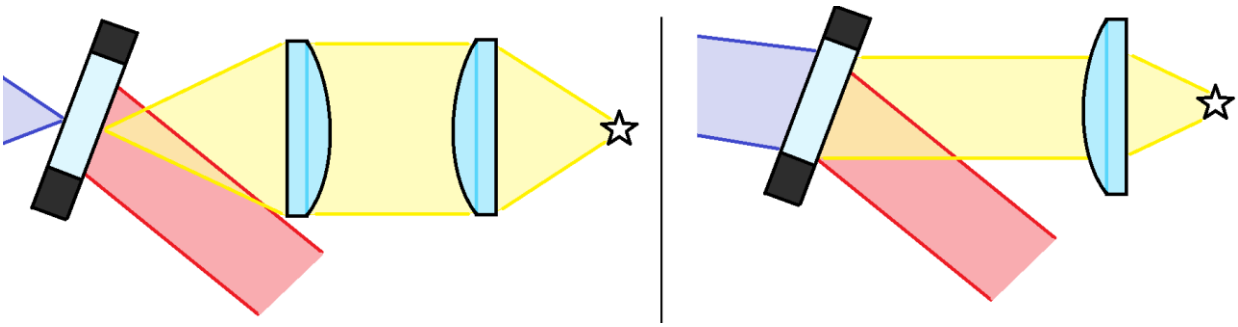

Figure 22. Principal schemes of the image plane upconversion (left) and the collimated beam upconversion (right).

5.4.3. Unresolved time imaging

In between the lenses of the Imaging module, a flipping mirror holder with a silver mirror was placed. When holder is set to a vertical position, the light collected by the 50 mm lens is being directed to the *UV-Nikkor* 105mm f/4.5s objective, which focuses the light on the *Blackfly* BLFY-U3-23S6C CCD camera. Using this camera, simple images, integrated over long (microseconds to seconds) time, can be captured. The objects of interest and various events can be viewed more similarly to the human eye. This was added for the comparison of the simple images to the time-resolved images.

5.5. Collection beam path

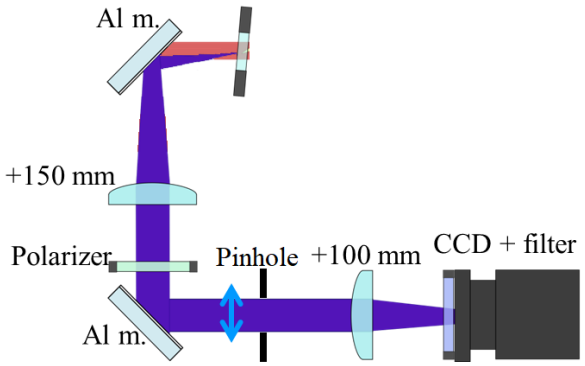

Figure 23. Part of main experimental setup – collection beam path.

The collection beam path images the Upconverted pulses to the CCD camera. It consists of a set of aluminum mirrors (reflectivity of S polarization ≈ 93 % @ 400 nm), a demagnifying telescope 2:3, an optional polarizer, a set of spectral filters (depending on the object of interest) and the *Blackfly* BFS-U3-32S4M CCD camera.

5.5.1. Imaging

The telescope images the crystal plane on the CCD camera with a magnification of 0.67. Such magnification was chosen to increase the intensity per pixel on the CCD camera. By doing this, the spatial resolution is reduced, but it was still sufficient enough. A 1:1 telescope or positive magnification can be used, if the spatial resolution needs to be improved. The Lenses for the telescope (and generally for all telescopes) were either plano-convex, meniscus or BF lenses (the *Best Form* lenses from "Thorlabs"). This was done to reduce the spherical aberrations. Worth mentioning is that the thickness of a lens is not an issue in this case, due to the fact that the Upconverted pulse is being integrated by the CCD camera and temporal broadening of the pulse is not important. Only the pulses of the Object and Gate beams have to be kept short before and during the sum frequency generation process.

An optional polarizer was included so that the generated sum frequency light would be transmitted, while the background noise from Object beam (if there were any) would be blocked. This polarizer does not help dealing with the background noise created by the Gate beam. The Upconverted, together with the Gate beam are both horizontally polarized, while the Object beam is mostly vertical.

5.5.2. Filters

The transmission spectra of the filters, which were used in the setup can be seen in Figure 24. In the same figure, normalized spectra of the laser pulse, its second harmonic (calculated using “Labview Lab2”) and the upconverted white light spectra are also visible for a reference. The exact configuration of the used filters was chosen depending on object of interest.

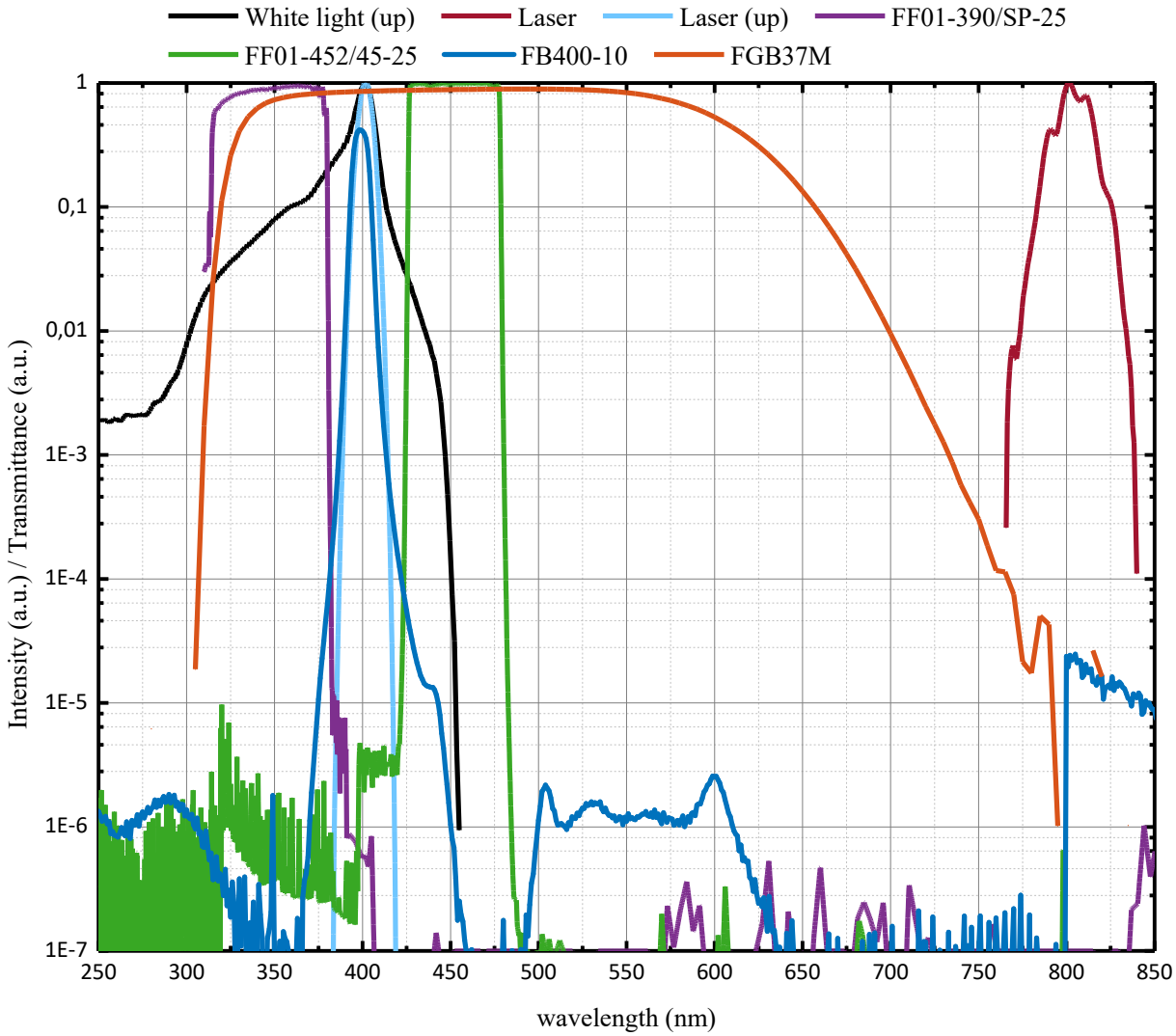

Figure 24. The transmittance spectra of the filters together with normalized intensity spectra of the laser, its second harmonic and the upconverted white light.

When observing an object which scatters the 800 nm laser light, it is needed to collect the 400 nm and block the 800 nm light, which is scattered all over the setup. In this case, bandpass filter FB-400-10 is used. It has peak a transmission of $T \approx 42\%$ @ 400 nm and a spectral bandwidth of 10 $\pm$ 2 nm FWHM. The OD (optical density) at 800 nm is > 4.5.

The colored glass filter FGB37M can also be used for detecting the upconverted signal. It has broad transmittance region, from the 335 nm to 610 nm. Thus, the Upconverted Signal is detected, while the 800 nm light is blocked. The filter can even be used together with the FB-400-10 filter to improve the 800 nm light rejection even further.

Both of the filters above do not help dealing with the background generated by the Gate pulse. Spectral separation of the Upconverted Signal from this background can only be done if the object of interest scatters wavelength not equal to 800 nm. In such case either the FF01-390/SP-25 or the FF01-452/45-25 filters are used, blocking both 800 nm and 400 nm background light.

The transmission range of the FF01-390/SP-25 is $T > 70\,\%$ @ $320-370$ nm and a blocking band $OD > 5$ @ $390-1100$ nm. This transmission range corresponds to the visible range of the object signal light around $535 - 715$ nm.

The FF01-452/45-25 filter has transmission range of $T > 93\,\%$ $423 - 475$ nm and blocking bands $OD > 8$ @ $370-410$ nm, $OD > 3.25$ @ 421 nm and $OD > 5$ @ $489-925$ nm. The purpose of using this filter is to detect the object light in the spectral range of $930 - 1160$ nm.

5.5.3. CCD camera

The resolution of Blackfly BFS-U3-32S4M camera is 2048×1536; the pixel size – 3.45 µm; the exposure time range $5\ \mu s - 30$ s. The quantum efficiency and the thermal noise of the camera are presented in Figure 25.

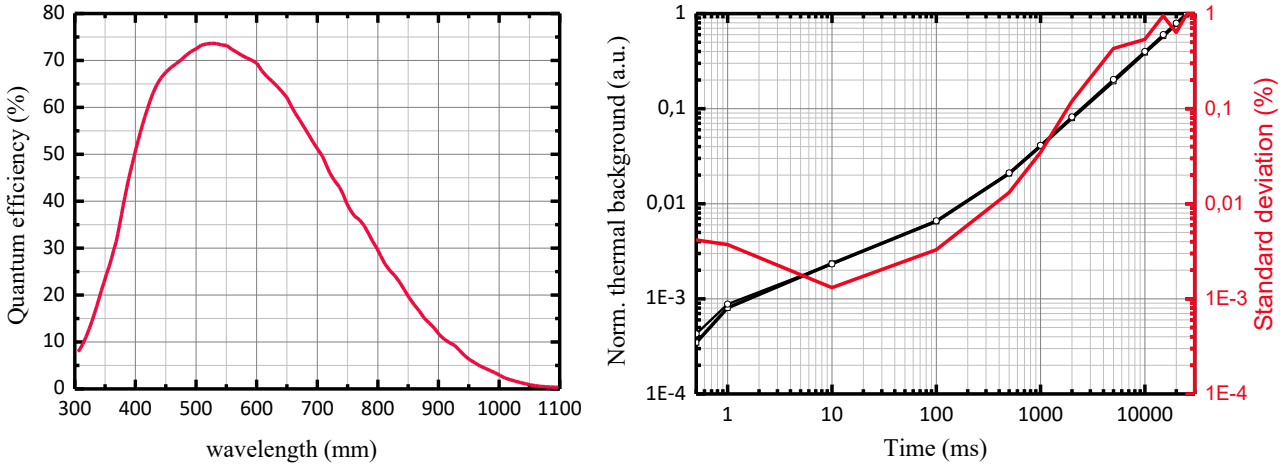

Figure 25. The quantum efficiency plot on the left and the thermal noise background the right.

As it can be seen on the thermal noise background plot, the thermal noise grows linearly with the integration time. This becomes a problem when the detectable signals are weak and long integration times are needed to capture the recorded data. Potentially, this CCD camera should be replaced with a cooled CCD camera, which has significantly lower thermal noise it its starts to grow noticeably slower with the integration time (integrating even for several minutes generates barely any thermal noise). Although, long integration times are not desirable as the experiment becomes more complicated – full recording of the event can take hours, hard and long adjustment process, changing environment conditions. Only few measurements were made with the cooled CCD camera, as it was installed just recently. Thermoelectrically cooled camera was a PCO Sensicam.

5.6. Software

For the automatization and control of the experiment, software synchronizing the delay stage with the CCD camera was needed. Software Labview was used to write the main control program, as well as several other programs for various calculations, data management and post processing.

5.6.1. Main control program

The main program used in experiment was written to control the main parameters of the CCD, the delay stage and to synchronize them together for capturing a sequence of frames, which can after be turned in to a slow motion movie of the event.

Software allows choosing main parameters of the CCD camera like exposure time, frame rate, black level, gain, white balance, size of sensor used and others. It switches off the auto adjustment functions like black level clamping, gamma, auto exposure time, etc. for a consistent signal over all recording of the event. Also the program allows manipulating frames – removing captured background, adding several frames together, averaging them to one frame, rotating and flipping the view. Either 8 or 16 bit monochrome pictures can be saved, together with the data matrix and the main parameters of the camera. Live view is always updated and can be seen in the main window in several different color scales. Additional information about the pictures can also be seen, like the mean value over selected region, the maximum value, the SNR value, the image histogram, integrated values over one of the image directions and so on. The main panel with controls and captured live stream can be seen in the Figure 26.

The delay stage can be controlled by the relative position jumps, position slider or by entering the absolute value. Calibration, holding position, reference search options are also added.

The main program can work in manual mode, where user has to press a button to capture each frame and move the stage, or in automatic mode, where step size of delay stage is chosen and frames with additional data are captured in sequence until program is stopped. It is important to save each stage position, as real step size fluctuates and over measurement errors accumulate.

Using Labview various other calculations were done, like pulse front tilting using prism or grating, walk-off angle, refractive indexes, angular dispersion, antireflection coatings, geometries of sum frequency generation, laser pulse elongation due to the dispersion, parameters of the Gaussian beam, Pulsed beam propagation simulations and several others. Also programs for control of the spectrometer, post processing of the captured images, the SNR calculator, image sequence to movie converter and editor were written.

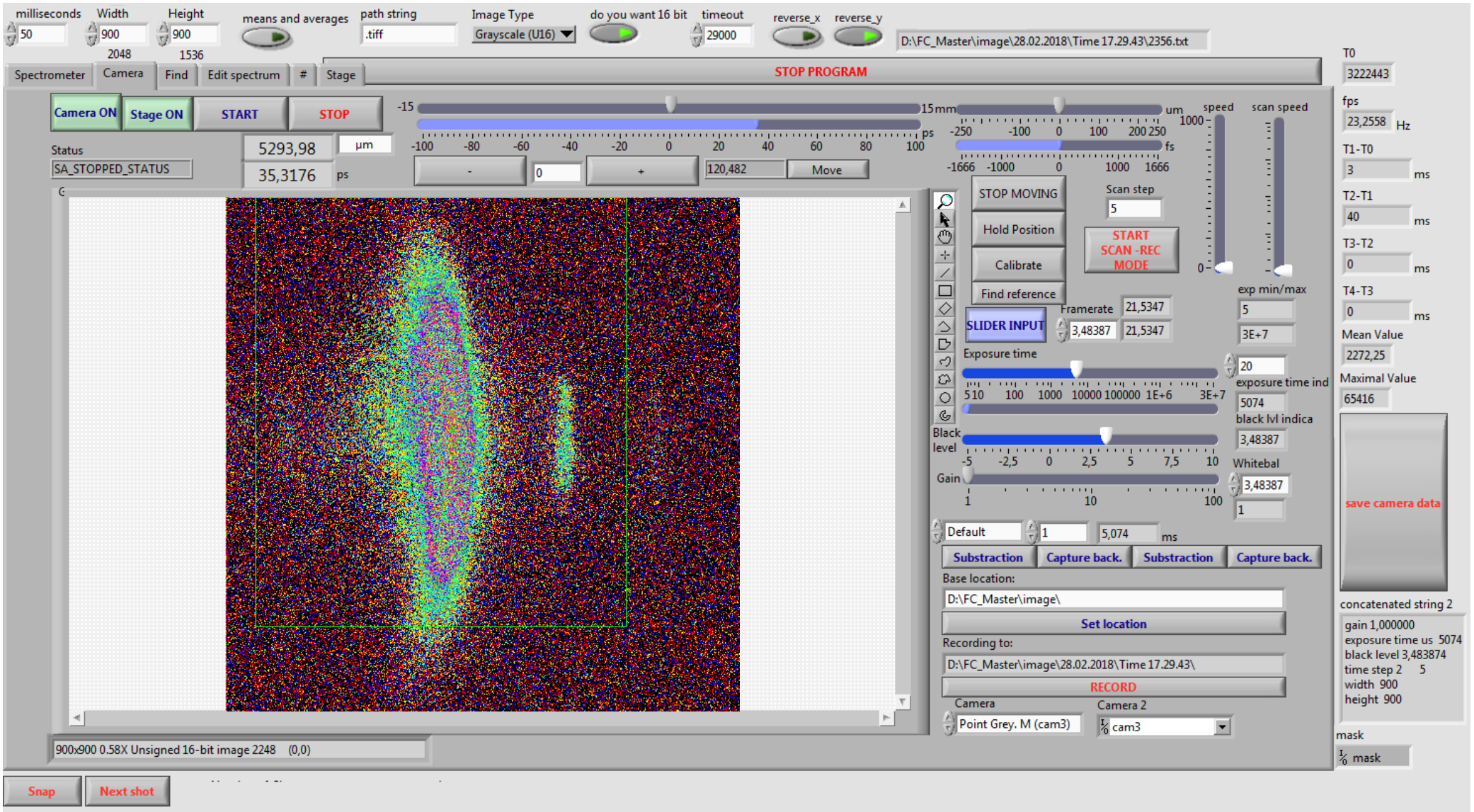

Figure 26. The graphical user interface of the main program used in experiment.

6. Results and overview

In the following chapter the main results – events captured using the Femtosecond camera – are presented. Events like reflection from the resolution test target, scattering from the plasma in air, pulse propagation in a bulk medium, propagation of the pulse in the water, strong scattering from ablation caused defects on the glass surface, were observed. While not all observations were successful due to the extremely weak signal, a lot of observed events were successfully recreated in slow motion movies, allowing observation of the spatial and spectral dynamics of the various optical processes.

6.1. Resolution test target

The first object for observation was chosen a Thorlabs resolution test target R1DS1P, made from chrome, plated on a soda lime glass substrate. The chrome forms a pattern of different thickness lines (sorted into elements and groups), designed for estimating the spatial resolution. Target has 6 groups (+2 to +7) with 6 elements each. The resolution using this target can be calculated using the formula: $Resolution\left[\frac{line\ pair}{mm}\right] = 2^{Group+\left(\frac{Element-1}{6}\right)}$; (43)

The line pair is formed of one black and one white line, next to each other. For example Group 2 and Element 1 shows resolution of 4 lp/mm (line pairs per millimeter), hence width of horizontal white line is 125 µm . Images, captured using this target, were used later as a spatial reference, while observing other objects (magnification of imaging of the system was not changed).

Figure 27 shows scheme of the experiment. The focusing element of the pump beam is removed. The collimated pump beam hits the resolution test target and is reflected. Surface of the target is imaged on the BBO crystal. For observation of this strong reflection, the power of the both Pump and Gate beams was set below 1 mW.

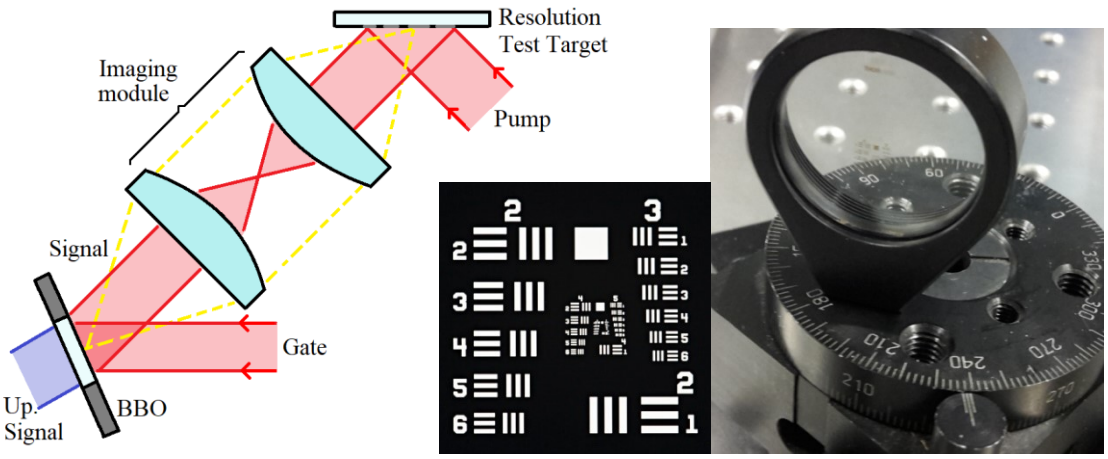

Figure 27. The scheme of the object placement on the left; the resolution target pattern in the middle and the resolution target mounted on the manual rotation and ***XY*** stage on the right.

6.1.1. Movie

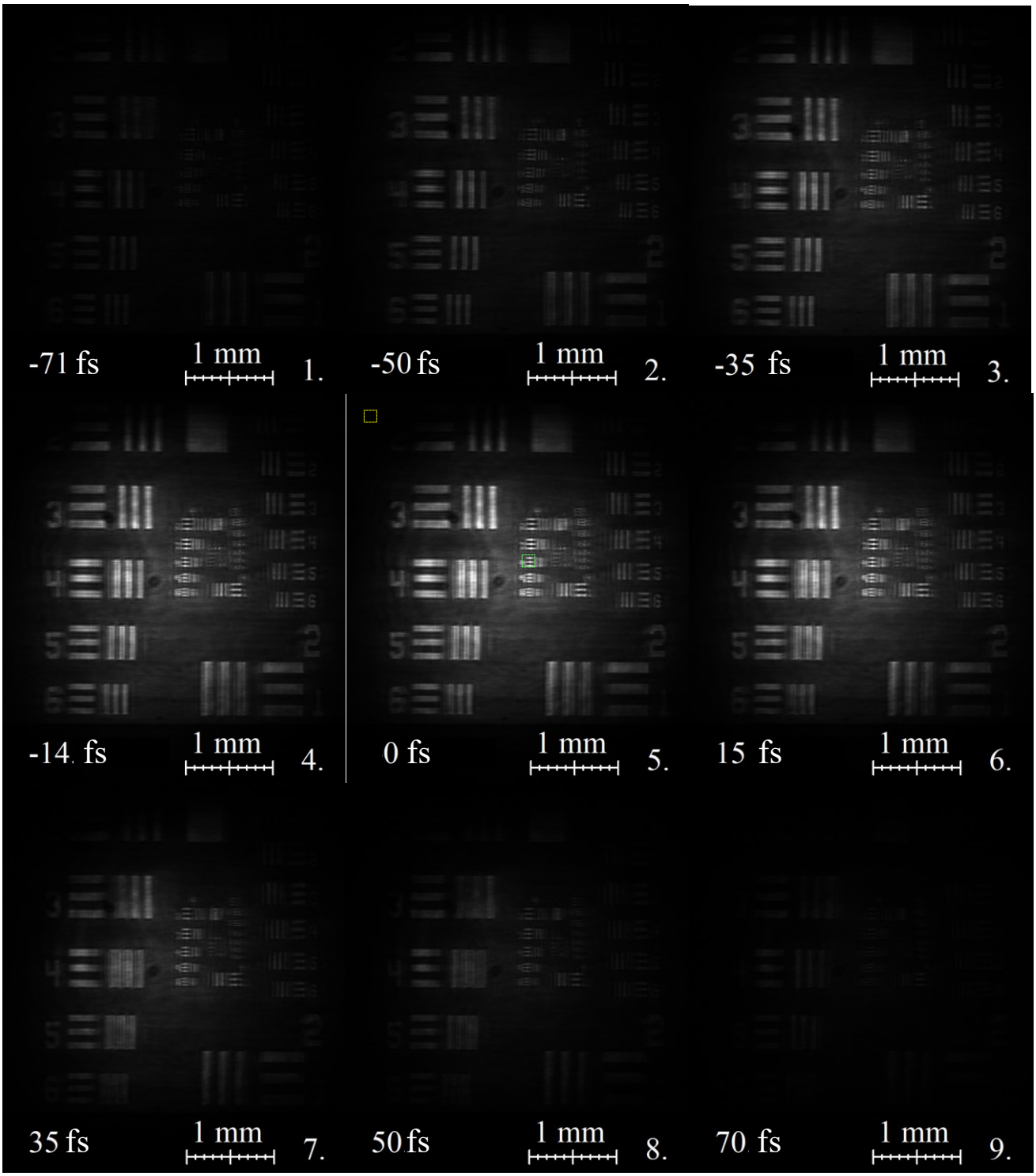

Figure 28. The pulse reflection from the resolution test target. Multiple frames with according time stamps. Total 825 frames were captured, with the time step set to 0.66 fs. It was necessary to record the actual delay stage position, due to the stage fluctuations. The real averaged time step was ~0.795 fs. The integration time for each frame was ~1 s. The slow motion video of the pulse reflecting from the resolution test target surface was recreated. The Signal-to-noise ratio of the following frames: $SNR_{db}(1st) = 10\log_{10}(signal_{mean}/background_{mean}) = 18.285$ dB; $SNR_{db}(5th) = 26.087$ dB. The green and yellow squares in the 5th frame mark the selected areas for SNR calculation. Depending on the selected area, at the peak of the pulse the signal-to-noise ratio can reach $SNR_{db} \approx 27$ dB.

6.1.2. Time resolution, autocorrelation measurement

The resolution test target was also used to determine temporal resolution of the Femtosecond camera setup. The time resolution of the setup depends on the length of the Gate pulse and temporal broadening introduced to the Signal pulse due to the collection setup.

The pulse before setup of the Femtosecond camera, was measured to be $\tau_{0.5} \approx 50$ fs. While observing the reflection of a pump beam from the test target, the Pump beam undergoes almost no material – only the neutral density filter wheel. Then, reflected from the test target, pulse is collected by the imaging module to be imaged on the BBO crystal, hence travels through two imaging lenses. Dispersion due to these lenses is almost negligible for a $\tau_{0.5} \approx 50$ fs pulse.

The Gating beam path also has a neutral density filter wheel, two telescope lenses and a true zero order wave-plate. Ideally, the Gate pulse should also be almost unchanged. Based on this, assumption was made, that the Gate pulse and the Signal pulse (the pump reflected from the resolution test target) should have same or at least very similar duration.

The captured image sequence is a cross-correlation measurement. To estimate duration of the Gate pulse, the images were averaged over selected areas to get mean Intensity value for each frame. Then, mean intensity, corresponding to correlation intensity was plotted against the delay time. Results can be seen in the Figure 29. The step size of the delay stage was 100 nm.

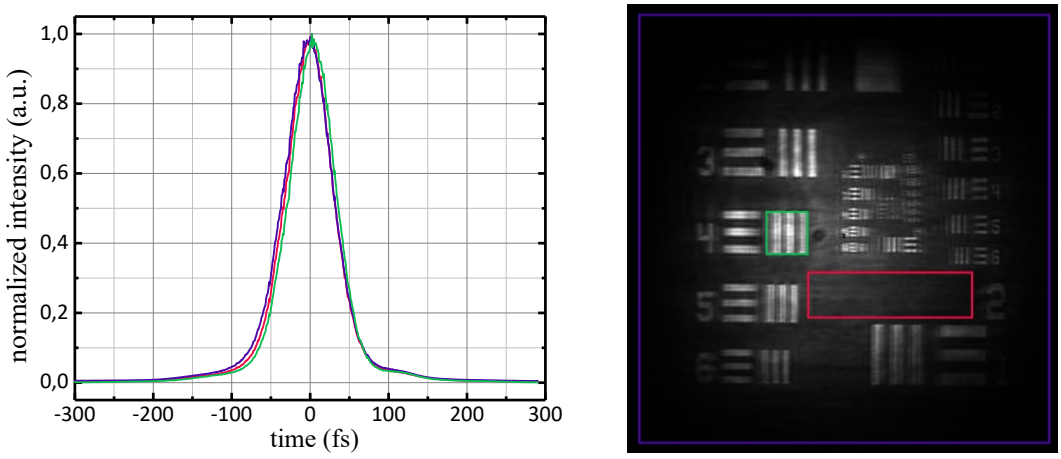

Figure 29. On the left – the cross-correlation function, on the right – the example frame from the measurement. The three different colors correspond to the different integration regions: blue curve integrates all the image, red – the glass substrate surface, green – the mostly metallic surface. Different regions were selected to make sure there is no significant dependence on the selected integration region. The Gaussian function was fitted for each plot and the cross-correlation durations were measured to be $T_{R0.5} = 70.38$ fs; $T_{B0.5} = 73.37$ fs; $T_{G0.5} = 69.48$ fs; giving $T_{0.5} = 71.08$ fs average.

The measured and normalized intensity cross-correlation function for Gaussian pulses can be written as:

$$G(T) = \frac{\int_{-\infty}^{+\infty} I_s(t) I_g(t-T) dt}{\int_{-\infty}^{+\infty} I_s(t) I_g(t) dt} = \frac{\int_{-\infty}^{+\infty} \exp\left(-\frac{2t^2}{\tau_0^2} - \frac{2(t-T)^2}{a_0^2}\right) dt}{\int_{-\infty}^{+\infty} \exp\left(-\frac{2t^2}{\tau_0^2} - \frac{2t^2}{a_0^2}\right) dt} = \exp\left(\frac{-2T^2}{\tau_0^2 + a_0^2}\right); \quad (44)$$

Here $\tau_0 = \sqrt{2\ln 2}\tau_{0.5};\ a_0 = \sqrt{2\ln 2}a_{0.5}$ are the pulse length parameters, defining the two pulses. From this, the cross-correlation full width half maximum can be related to the duration of the pulses:

$$T_{0.5}^2 = a_{0.5}^2 + \tau_{0.5}^2; \quad (45)$$

If the both pulses have similar duration, as it is assumed in this experiment, then the cross-correlation turns into the autocorrelation. Then $T_{0.5}^2 = 2\tau_{0.5}^2$ and duration of the both pulses:

$$\tau_{0.5} = \frac{T_{0.5}}{\sqrt{2}} = \frac{71.08 \text{ fs}}{\sqrt{2}} = 50.26 \text{ fs} \approx 50 \text{ fs}$$

The autocorrelation measurement shows that the duration of the both Gate and Signal pulses are ~ 50 fs, hence neither the Gate nor the Signal pulses experienced temporal broadening in the Femtosecond camera setup. This number describes the time resolution of the Femtosecond Camera, no shorter signal can be resolved. The time resolution in this case is mostly limited by the original laser pulse duration, determined by the used Laser setup.

6.1.3. Dimensions and spatial resolution

Dimension of the captured images can be estimated using the pattern of the resolution test target. Later this information can be used to estimate the spatial dimensions of the other observed events. The spatial resolution of the Femtosecond Camera can also be estimated using the test target. Because the image of test target is captured by the beam reflecting from surface, it should be noted, that only the horizontal scale bars should be used for the dimension estimation, due to the fact, that pattern of the test target preserves its dimensions only vertically. Horizontally image is squeezed, as the projection of surface is imaged (imaged surface is not perpendicular to the imaging setup, but tilted by ~40 deg, hence it appears smaller).

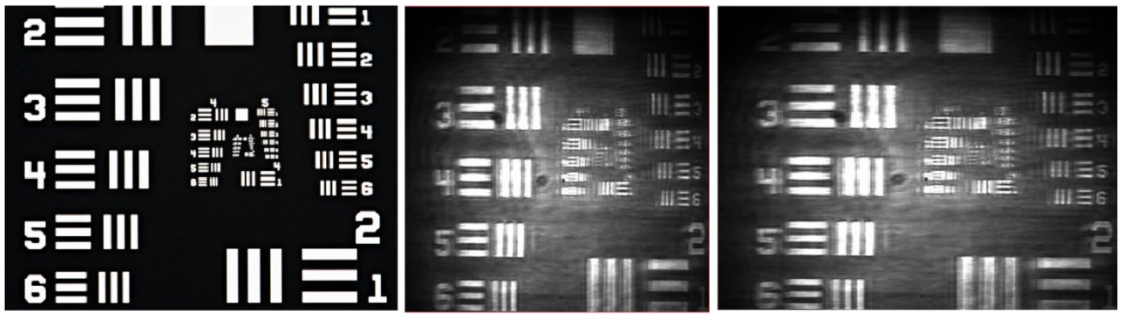

Figure 30. Horizontal scaling of captured target pattern. Captured image (center) has to be extended (right) by 132% to match original pattern (left).

With this exact setup and magnification, if reflection is not saturated, the lines from Group 5 Element 4 can still be distinguishable, hence the spatial resolution of this setup is

~45.3 lp/mm which is correspond to the line thickness of ~11.04 µm. This number is not limited by the diffraction limit, nor by the pixel size. Since the pixel size is not a limiting factor, in this experiment only part (900×900 pixels) of the CCD sensor was used. To improve the spatial resolution, optics with better aberration compensation should be used. Also some resolution is lost during the upconversion process, although most likely the aberrations are the main issue.

6.1.4. Long time scale measurement

In the previous measurement, only several hundred femtoseconds around the main laser pulse were recorded. The movie capturing a longer time scale of the pulse reflection from the test target was also recorder. It was observed that besides the main pulse, there are a lot of weaker signals coming before and after the main peak. The signal (integrated over frame area) dependence on the time can be seen in Figure 31.

Several things can be noticed about this intensity distribution. First of all, as previously, the upconverted Signal of the scattered light from the test target can be interpreted as an autocorrelation signal. An autocorrelation signal is a symmetric function, hence there must be some symmetry in this measurement. Indeed, there are several symmetric peaks marked with the blue arrows: $\pm$ 21 ps ; $\pm$ 18 ps; $\pm$ 12 ps; $\pm$ 9 ps. While the autocorrelation does not give a lot information about temporal shape of the laser pulse, these second peaks indicate that the Pump and Gate pulses have some pre-pulses, post-pulses or both.

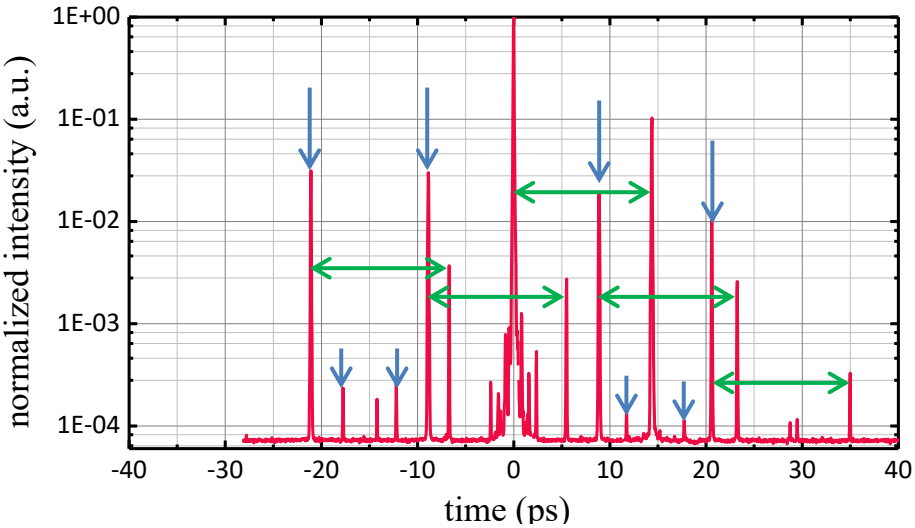

Figure 31. Normalized mean intensity over the time. The step size ~33.3 fs.

Another interesting feature is that if the each symmetric peak is shifted by 14.3 ps, it matches with the positions of non-symmetric peaks (marked by green arrows). The origins of this effect is described below. The frames from the recorded movie with the corresponding time scales are presented in the Figure 32. This captured movie allows the observation how the Pump pulse

(with its secondary pulses) is being reflected from the front and from the back surfaces of the resolution test target substrate.

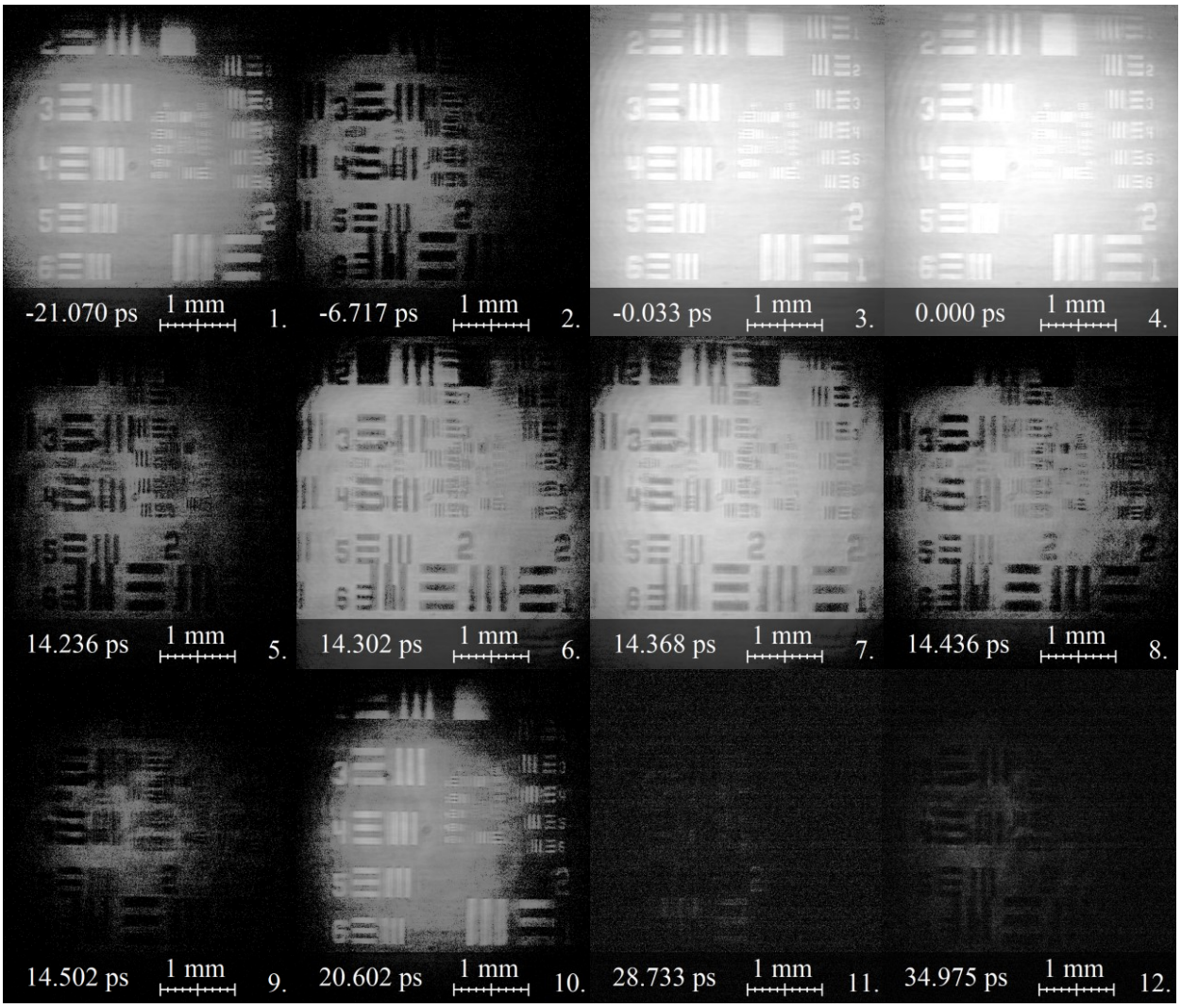

Figure 32. Multiple frames acquired during long time scale measurement. The SNR values of following frames are presented below (metal – reflection from the metal area chosen as a signal, glass – reflection from the glass area chosen as a signal): $SNR_{db}(1st, metal) = 24.38$ dB; $SNR_{db}(1st, glass) = 17.69$ dB; $SNR_{db}(2nd) = 12.17$ dB; $SNR_{db}(11th) = 3.40512$ dB.

The whole movie consist of 2532 frames with step size of 33 fs. In the first and the second frames a pre-pulse generated peak and its reflection from the second surface of the resolution target substrate are presented. In the frames 3, 4 – the reflection of the main peak is visible. The Frames 5-9 show the reflection of the main peak from the second surface. It can be seen, that in the reflections from back surface, color of metallic scale bars is inverted and the scale bars are duplicated and shifted. This happens, because the pulse going through 1st surface is being partially blocked by scale bars, then reflected from back surface, then again refracted by first surface and partially blocked by scale bars one more time. Images 10, 12 show the secondary pulse being reflected from front and back surfaces. Image 11 shows very weak reflection of the peak pulse from the back surface for the second time. Notice that it features the positive (bright) and

shifted reflection of scale bars, as it should. All images except 11 and 12 are in logarithmic scale, 11 and 12 being in linear with strong gain value.

The thickness of the resolution target substrate was $d = 1.524$ mm, the refractive index of substrate was $n = 1.517$, the group index $n_{gr} = 1.517$. Then, the delay between the reflected pulses from the front and back surfaces can be calculated using the formula:

$$\Delta t = \frac{2d(n_{gr} - \sin\alpha \sin\beta)}{c \cos\beta}; \quad (46)$$

Here, α and β are the incidence and refraction angles related by the Snell's law. Reflected rays from the second surface are shifted in horizontal direction by the distance $\Delta x = 2d\cos\alpha \tan\beta$; (47). From the Figure 32 pictures 6-7, where the two target patterns are visible, it was estimated that $\Delta x \approx 1.1$ mm, which gives a $\alpha \approx 40.8$ deg and the time difference $\Delta t = 14.11$ ps, which more or less matches shifting value in Figure 31. This geometry also matches scaling factor presented in Figure 30, as $\cos\alpha \approx 1/1.32$.

6.2. Air plasma

The next target of observation was scattering from the laser induced plasma in air. The principle scheme of this experiment is presented in the figure below.

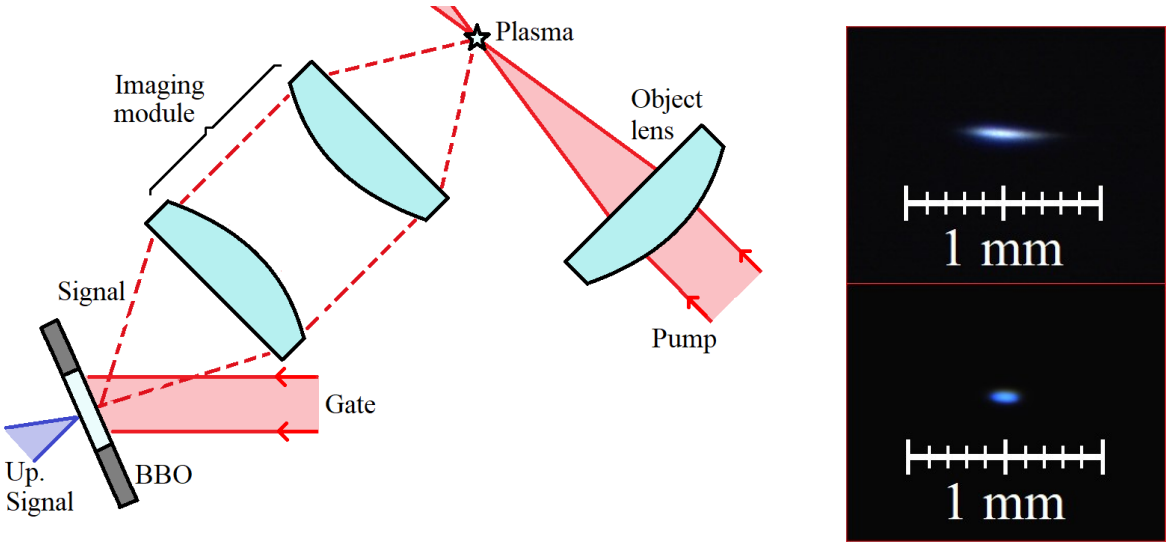

Figure 33. Principal scheme of the air plasma measurement on the left. The pump beam is focused and the air plasma is being generated. The scattered light of the same pulse is being collected by the imaging module and imaged on the CCD camera. On the right – images of the air plasma taken with the time unresolved imaging branch. Upper – the plasma filament generated by using the 75 mm lens, lower – 16.5 mm objective. Note that while the lower plasma filament looks dimmer, it is due to the additional filter, before the CCD camera. The intensity is higher while focusing with the objective.

Initially, with this configuration, the target of interest was scattering from the air molecules, with the goal to observe the propagation of the laser pulse in the air. The signal scattered

from air is extremely low and it was impossible to detect with the current Femtosecond camera setup, as the signal drowns in either the Gate background or the thermal noise of the camera. Power of the pump beam is limited by the air plasma generation threshold limit. To increase the signal-to-background ratio, Gate power was reduced, resulting in the necessity to increase the integration time of the camera, as the signal drops as well. Due to this, the noise, caused by the Gate beam, becomes visible again. Eventually, no Signal is observable even with the maximum integration time.

Pulse breakdown in air however is easy to generate and the generated plasma filament scatters the laser pulse itself. This signal, while still quite week, is significantly higher than the scattering just from the air.

6.2.1. Focusing, intensities

As mentioned before, the object lens was either a $f = 75$ mm, $d = 25.4$ mm lens or an objective with 0.25 NA, $f = 16.5$ mm, $d = 7.5$ mm. The diameter of the Pump beam was $2\omega_{0.5} \sim 5.63$ mm. The radius of the of the focused beam can be calculated using the formulas: $\omega_{1/e^2} = \frac{\omega_{FWHM}}{\sqrt{2\ln(2)}}$; (39), $\omega'_{1/e^2} = \frac{\omega_{1/e^2}}{\sqrt{\left(1+{}^{S}/_{f}\right)^2+\left({}^{z_R}/_{f}\right)^2}}$; (40), $z_R = \frac{\pi\omega^2{}_{1/e^2}}{M^2\lambda}$; (41) and for a truncated beam, the radius can be expressed as a $\omega = K\lambda\frac{f}{d}$ (48), where K is the coefficient:

$$K_{0.5} = 1.029 + \frac{0.7125}{\left(2\omega_{1/e^2}/d - 0.2161\right)^{2.179}} - \frac{0.6445}{\left(2\omega_{1/e^2}/d - 0.2161\right)^{2.221}}; \quad (49)$$

$$K_{1/e^2} = 1.6449 + \frac{0.6460}{\left(2\,\omega_{1/e^2}/d - 0.2816\right)^{1.821}} - \frac{0.5320}{\left(2\omega_{1/e^2}/d - 0.2816\right)^{1.891}}; \quad (50)$$

New spot radii were estimated to be: $\omega_{lens\,1/e^2} \approx 4$ µm; $\omega_{obj.\,1/e^2} \approx 1.55$ µm; and the corresponding Rayleigh lengths $z_{R\,lens} \approx 63$ µm; $z_{R\,obj.} \approx 4.4$ µm. The average power, transmitted through the each lens was accordingly $P_{lens} \approx 268$ mW and $P_{obj.} \approx 180$ mW. Given that the repetition rate of the laser is $R_{rep} = 1$ kHz and the pump pulse duration $\tau_{0.5} \approx 50$ fs, using the formula $I_{peak} = \frac{P_{peak}}{S} = \frac{E}{\tau S} = \frac{E}{\tau\pi\omega^2} = \frac{P_{vid}}{R_{rep}\tau\pi\omega^2}$, (42), peak intensities were estimated to be $I_{lens\,peak} = 1.06 \times 10^{16}$ W/cm^2 and $I_{objective\,peak} = 4.78 \times 10^{16}$ W/cm^2. The peak powers accordingly were $P_{lens\,peak} \approx 5.36 \times 10^9$ W and $P_{objective\,peak} \approx 3.6 \times 10^9$ W.

This is an extremely rough estimation, as first of all, the aberrations make the spot size bigger, hence the intensity drops. Also, due to the nonlinear effects, (nonlinear change of the refractive index, which causes the self-focusing effect and the self-phase modulation) the pulse breaks down spatially and spectrally, before reaching such intensities.

6.2.2. Plasma generation

Based on these estimations, the peak power of the laser beam is slightly higher than the critical power of self-focusing in the air $P_{cr} = 3.77\lambda^2/8\pi n_0 n_2 \approx 2 \times 10^9$ W; ($n_2 = 5 \times 10^{-19}\text{cm}^2/\text{W}$) [64]. This means, that the beam would eventually focus itself even without focusing, as the self-focusing is stronger than the divergence of the beam. When the beam is focused with a focusing element, this self-focusing is an addition factor of the decreasing pulse diameter. As the beam get smaller, the intensity increases and eventually the free-electron plasma is being generated due to the either tunnel or multiphoton ionization (or both). The beam is being defocused by it, as the refractive index where most electrons are generated decreases linearly with the increasing electron density. Generally, these two counter effects change spatial parameters of the laser, and the long plasma filaments in air (and other mediums) can be observed.

As electrons recombine, the electron plasma emits broad spectrum fluorescence, easily observable by naked eye. Although, duration of the fluorescence is significantly longer (the plasma starts to decay only after several nanoseconds, and lasts for even microseconds)[65]. By using the current setup of Femtosecond Camera, is not possible to observe the Fluorescence of plasma, because the Gating time $is \sim 10^6 - 10^9$ shorter than the fluorescence, that only extremely small fraction of luminesced light is collected.

On the other hand, pulse scattering from the plasma filament can be observed. Trailing edge of the pulse is being scattered by the plasma, created by the front side of the pulse.

6.2.3. Movie

In the next Figure 34, the results from the plasma scattering event are presented. Each of the presented frames is a composition of two overlaid pictures, from two measurements. Upper filament was generated with the $+75$ mm lens, lower filament – with 16.5 mm objective. Pulse is being scattered by the filament, making the event visible. By using the +75 mm lens, longer filament is being generated and longer distance of the pulse propagation can be visible. The filament produced by the objective is shorter and narrower. Totally > 1000 frames taken with the time step of 3.34 fs.

The wavelength of all collected and upconverted light is 400 nm, which corresponds to the 800 nm signal. We can see that speed of pulse propagating is $v \approx 3.4 \times 10^8$ m/s, which is approximately equal to the speed of light in air, with an 17% error. Speed of light value is not accurate due to several reasons. First of all, time scale in this exact measurement was calculated using the step value of the delay stage, which later was found out to be incorrect, as the delay step fluctuates and over time overall distance deviates and is usually longer. Absolute position of the

stage should be saved. Another issue was, that while slightly adjusting focus of the imaging setup to see sharp image, the magnification slightly changes, which gives additional error.

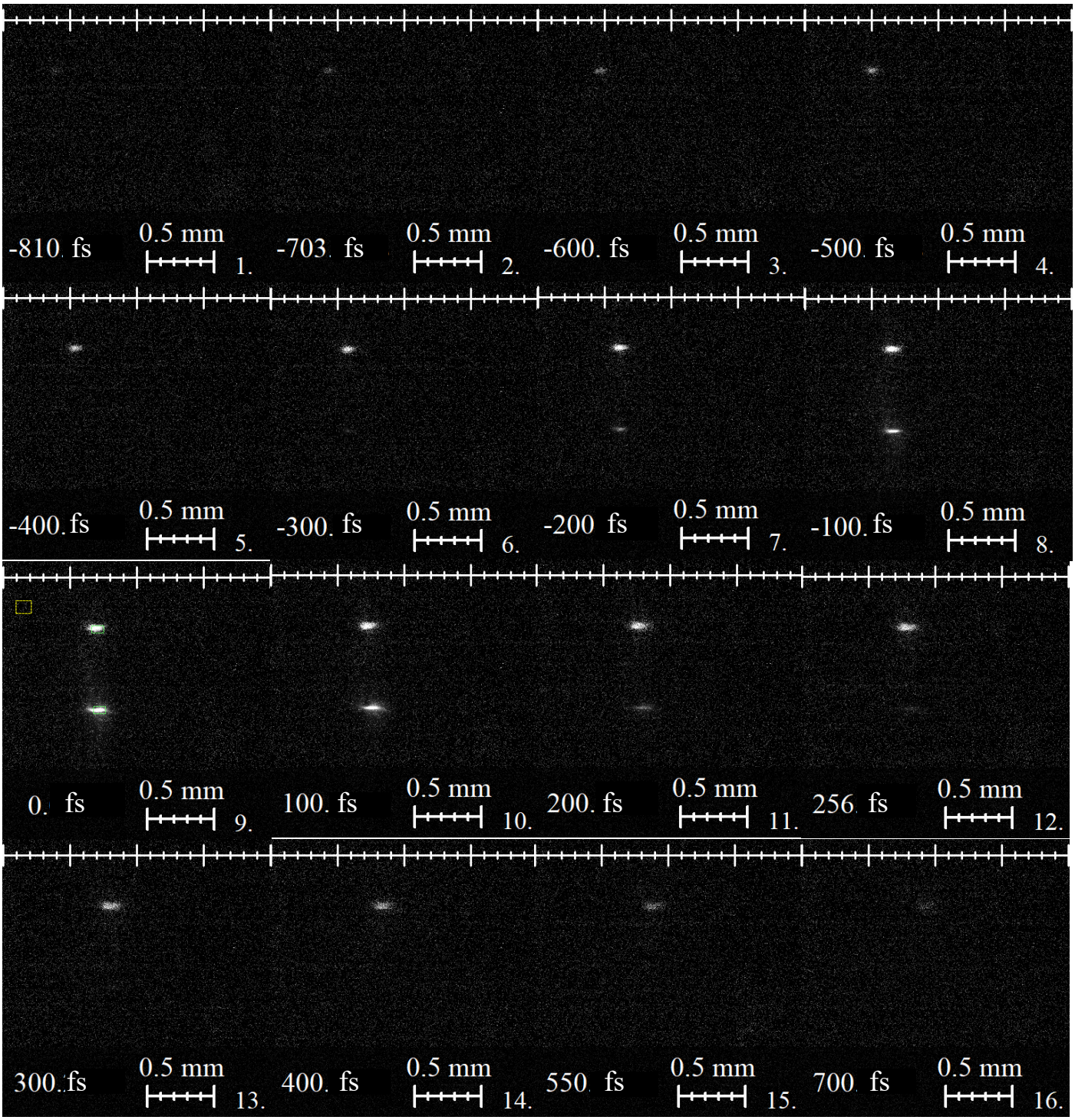

Figure 34. The pulse scattering from the air plasma filament. Side view. Propagation of the pulse direction is from left to right. The upper filament generated by focused with the +75 mm lens, lower – using the 16.5 mm objective. The signal values are equalized for better imaging. The integration times of the CCD were $t_{objective} = 500$ ms and $t_{lens} = 2$ s. The SNR values of 9th and 11th frames: $SNR_{db}(9th, lens) = 13.799$ dB; $SNR_{db}(9th, objective) = 22.45$ dB; $SNR_{db}(11th, lens) = 13.742$ dB; $SNR_{db}(11th, objective) = 12.67$ dB. The signal generated by the lens was generally weaker.

An interesting observation is that the pulses appear to be longer than **50 fs** not due to the time resolution of our camera, but rather due to the size of the object. The speed of light is not infinite and it takes different amounts of time to travel different distances. Hence, if the pulse is at some point in space and it is seen by observer, additionally observer will also see the scattered light from the previous positions of laser pulse, if the transverse width of the pulse was larger than its length.

6.3. Solid medium

After trying to see the scattering of the laser pulse from the air and recording the scattering from the laser-induced air plasma, next target of choice was a bulk medium. The propagation of the light in the two types of media – glass and sapphire was observed.

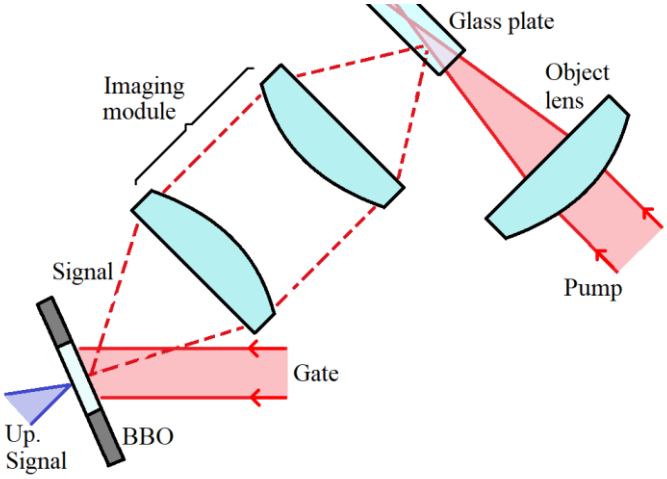

Figure 35. Principal scheme of the pulse propagation inside solid, transparent medium, measurement.

After some initial testing, it was concluded that detecting a pulse propagating inside a solid media is not much easier than detecting a pulse propagating in air, due to also low scattering coefficient. While the scattering from surfaces or defects inside the medium gives extremely high signal, the goal was to see how the pulse propagates through the medium itself.

Several things could be done, which could help. First of all, if the intensity is increased, the scattering signal should increase as well, hence the pump beam was focused inside medium. On the other hand, laser should not generate any defects inside that medium, as they start to scatter strongly and overwhelm the scattering from the bulk medium. So either the field of view should be outside the generated defects, or the laser intensity should be below the damage threshold of the medium.

Another thing, which could help, is observation of different wavelength than the Gating beam. The intensity was increased for a filament generation and hence, generation of additional

laser frequencies. Then, with the filters blocking the 400 nm Gating background, propagation of these newly generated frequencies pulses could be observed.

Last thing which would help is to somehow increase the scattering efficiency. This was done with scratching the side wall of the glass plate and directing the beam near it. Ideally, this would generate more scattered light, which can be collected.

6.3.1. Glass plate with scratched side surface

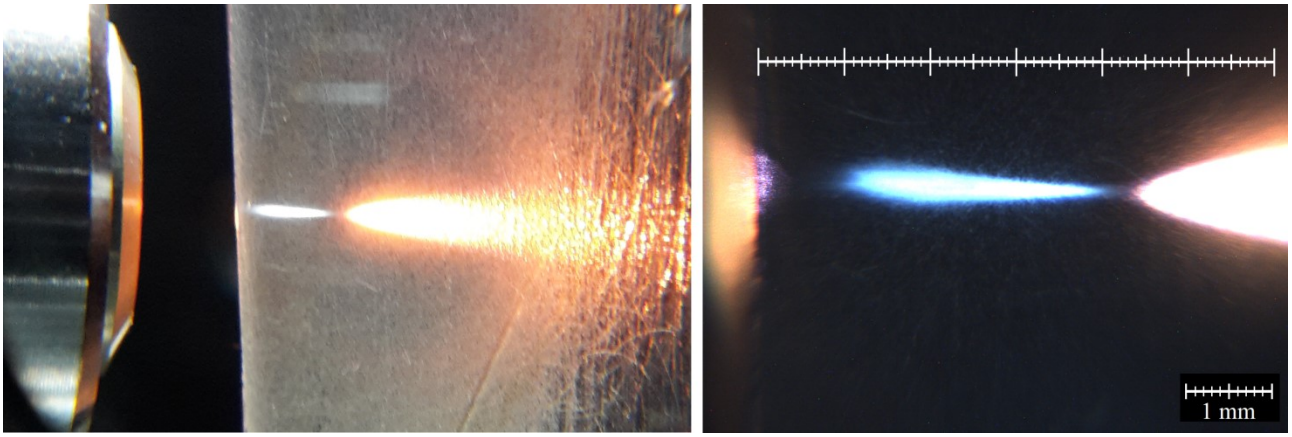

Figure 36. The glass plate with the scratched side surface and the filament being generated inside it. Laser was focused with the 16.5 mm objective. The emitted light of the plasma is observed, followed by laser light with broadened spectrum.

The main goal of this measurement was to detect any scattering of the laser pulse propagating inside the material. Measurement was done using the 400 nm bandpass filter before the CCD camera, which corresponds of detection of the 800 nm Signal. The power of the Gate beam was 124 mW, while the power of the Pump beam ~ 175 mW. The focus point of the Pump beam was chosen to be close to the side edge of the glass plate, but not too close, to prevent ablation.

Results of this measurement can are shown in the Figure 37.

The pulse is propagating from the left to the right. The field-of-view in each frame is around 4 mm × 4 mm and is located near the surface of a glass plate. Surface of the glass plate is marked by the blue line in the 1st frame. To the right from it – the glass medium. In the second frame, at 0 ps, the main peak of the Pump pulse hits the glass plate strong scattering can be observed. The green arrow marks the signal a from pre-pulse, which arrived earlier, before the main peak. In the 4th frame, the main pulse splits into two pulses, marked with red and blue arrows.

The group propagation velocities of each pulse were calculated to be:

$$v_{green} = \frac{\Delta s}{\Delta t} \approx 2 \times 10^8 \text{ m/s};\ v_{red} \approx 2 \times 10^8 \text{ m/s};\ v_{blue} \approx 3 \times 10^8 \text{ m/s};$$

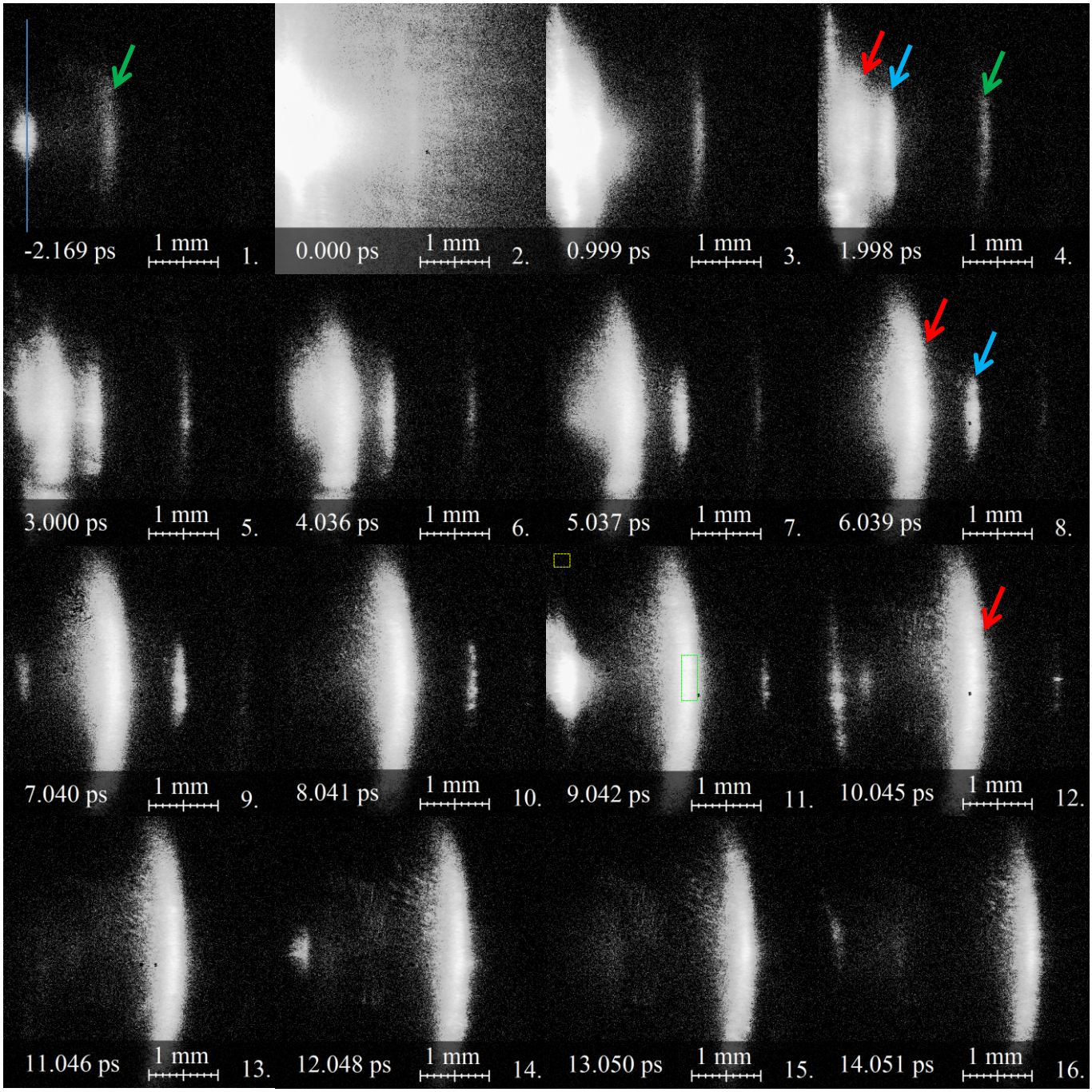

Figure 37. The scattering of the pulse inside a glass medium. Side view. Integration time of each frame 600 ms. Totally 1080 frames captured with a time step of ~33 fs. The images are presented in logarithmic scale. The signal-to-noise ratio of the main peak, 11th frame: $SNR_{db}(11th) = 19.453$ dB.

The pulses marked with the red and green arrows move around 1.5x slower than the blue arrow marked pulse, which has the velocity roughly equal to the speed of light. Which means, that strongest, red arrow marked signal, comes from a pulse, propagating inside a glass substrate. Same applies to the pulse marked by the green arrow. Blue arrow marked signal most likely comes from the light, which propagate near the glass surface from the air side. After the initial Pump pulse hits the surface of the glass substrate, part of it travels inside medium, part of it – outside.

The pulses marked with the green and red arrows have constant separation of ~1.88 mm which corresponds to ~9.4 ps. In 11th frame, after ~9 ps from the main peak, another signal is visible. This is similar to autocorrelation measurement, as signals are most likely symmetrical. They indicate that the both Gate and Pump pulses have some pre-pulses, post-pulses or both.

One thing to notice, is that while light propagating inside glass medium can be observed, its scattered by side wall, not by homogenous medium. Hence, no spatial changes over propagation distance are observed, although it would be expected for a beam to get smaller, as it is focused.

Before changing to the other object, filters before the CCD camera were changed to detect any light below or above 800 nm. This allowed increasing the integration time, as the Gate background is no longer an issue, because it is blocked by either FF01-390/SP-25 or FF01-452/45-25 filter. Despite of that, even with the integration times of 25-30s no signal was detected.

The observed region covered only 4 mm after the glass surface. No new laser frequencies were generated in this region, or they were too weak to detect.

6.3.2. Clear glass plate

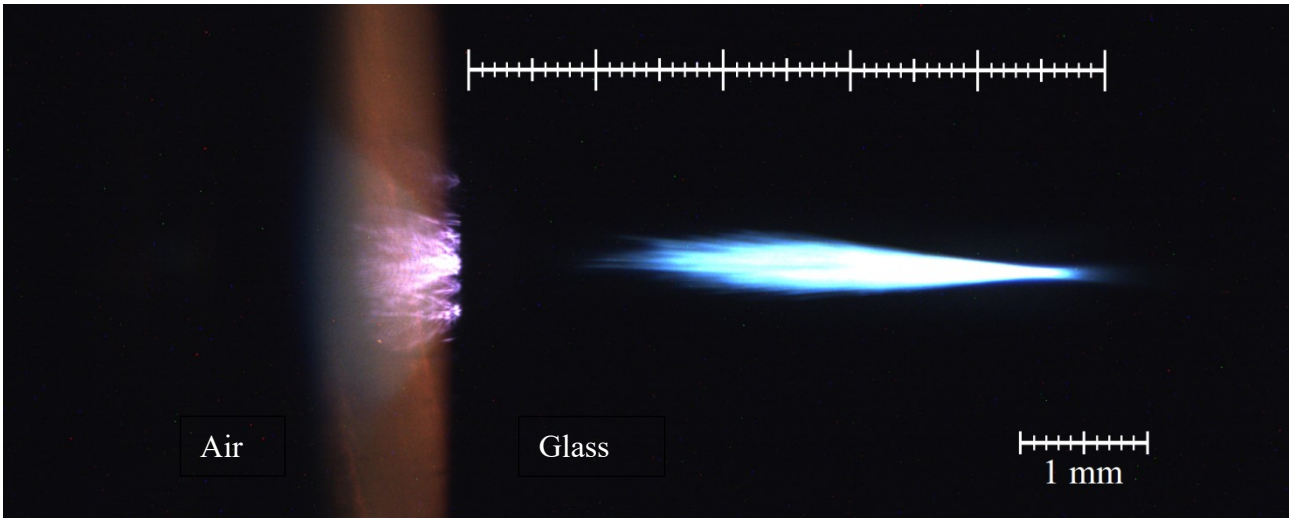

Figure 38. The side of the glass plate and filament being generated inside of it. The beam was focused with 16.5 mm objective.

The glass plate with a scratched side surface was replaced with a regular glass plate. After several tests, few observations were made. As expected, any detectable signals were reduced significantly. The strong scattering was seen during the pulse hitting the surface of the glass plate, similarly to the previous measurements. After the pulse hits the s, some scattering signals can be observed, propagating at the speed of light. This indicates, that some light is traveling near the glass

plate from the air side and is being scattered by the side wall of the glass plate, similarly to the scratched glass plate.

Since the goal was to detect the pulse scattering from inside the sample, the integration time was increased, trying to detect any weak signal. This of course resulted in a higher background both due to the thermal noise and the Gate background. Results are presented in the Figure 39.

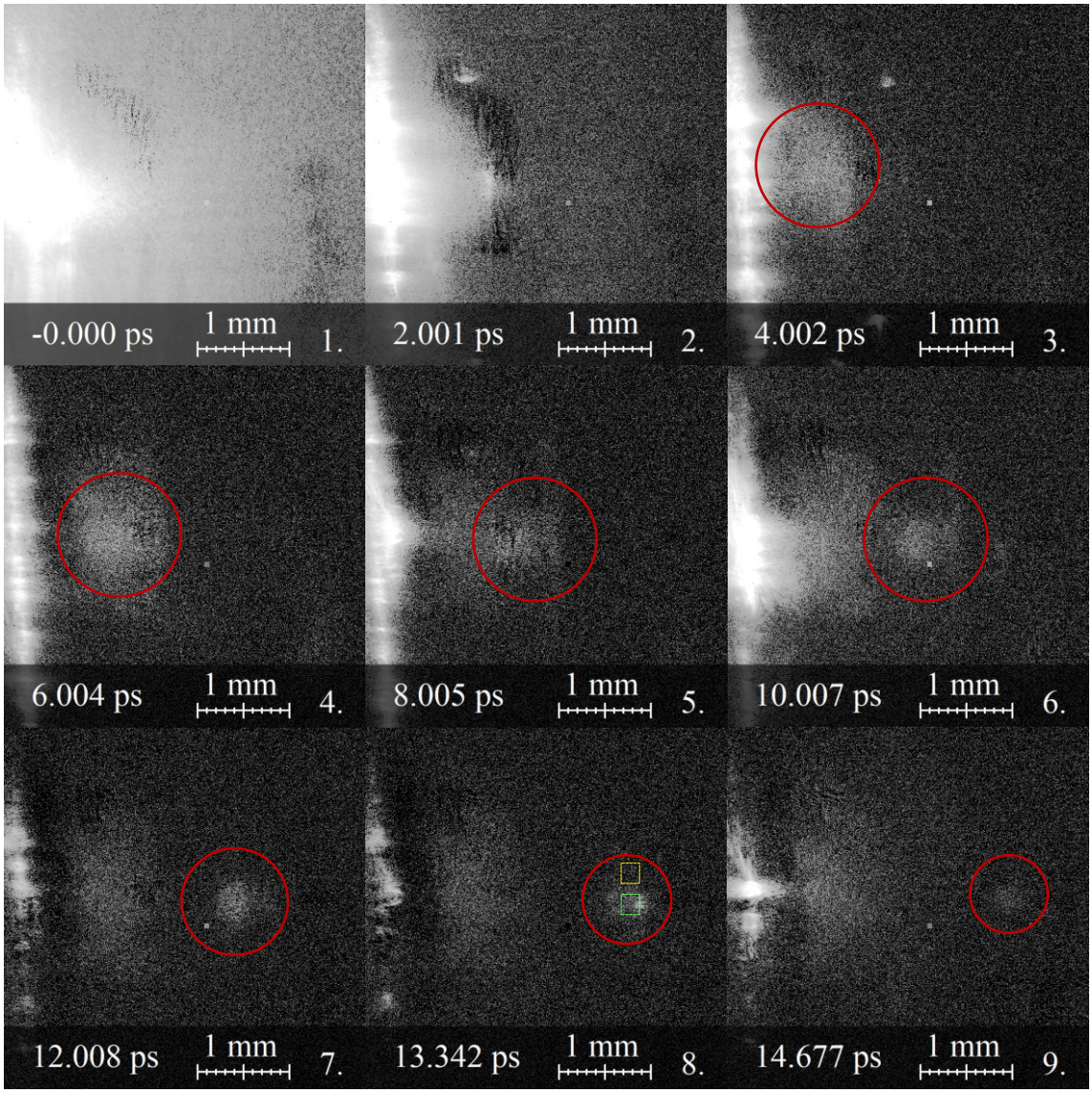

Figure 39. A pulse scattering inside the glass medium. Side view. The integration time of each frame ~15 s. Totally 104 frames captured with a time step of ~667 fs. Images are presented in a logarithmic scale. The power of the Pump beam was 175 mW, the power of the Gate beam – 59 mW. The signal-to-noise ratios of the following images: $SNR_{db}(4th) \approx 2.9667$ dB; $SNR_{db}(6th) \approx 4.921$ dB; $SNR_{db}(8th) \approx 5.4385$ dB. The green and yellow squares in 8th frame marks selected areas for SNR calculation. Similarly SNR was calculated in other frames.

In the 1st frame, the pulse hits the glass surface, strong scattering is seen. In the next several frames, while hardly distinguishable from the background, the pulse propagates further in to

the glass medium. From the 6th frame it can be more easily distinguishable from the background noise. A red circle marks the detected pulse, propagating with a speed of $\sim 2 \times 10^8$ m/s, which is roughly the speed, that the pulse should propagate in bulk glass. It can be seen, that the detected pulse gets smaller. This is expected, as the beam is focused and width of the beam is decreasing. This (together with the propagation speed) indicates, that the detected pulse could actually be a pulse propagating in the glass medium, being scattered by the glass substrate itself.

6.3.3. Sapphire

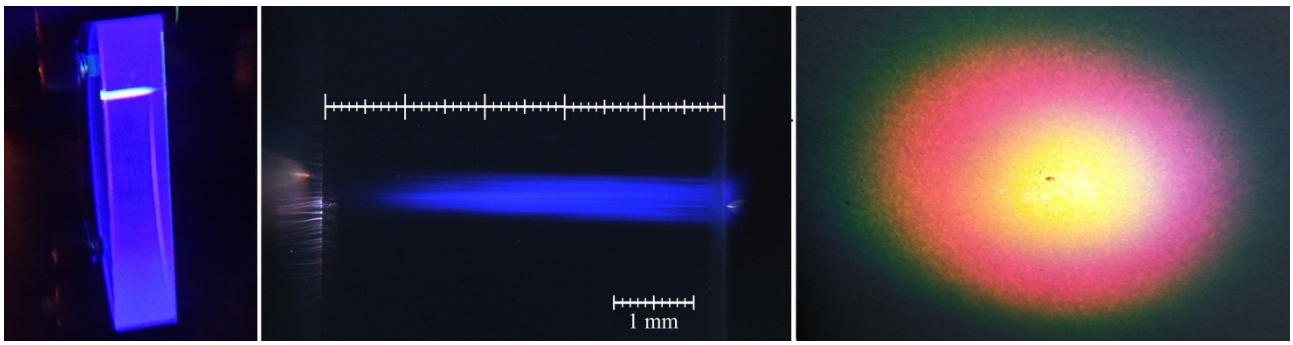

Figure 40. Generation of the white light in sapphire. In the first two pictures – sapphire luminescence. On the right, picture the white light continuum generated in a sapphire window. The beam was focused using +75 mm lens. The thickness of the sapphire was 5 mm.

The goal of this measurement was to capture the white light generation in the sapphire using the Femtosecond Camera setup. While the intense light is propagating in the sapphire, due to third order nonlinear effects like the self-phase modulation and the 4-wave mixing, new frequencies of the spectrum are being generated – spectrum gets so broad that it covers most of the visible light and even some infrared.

The idea was to capture this event in a slow motion video and to observe these new frequencies being generated. The background coming from Gate pulse can be easily removed using FF01-390/SP-25 or filter FF01-452/45-25, allowing increase of integration time to the maximum value.

Unfortunately, even using the longest integration times of the CCD camera (the limit was 30 s) no signal was detected with neither of the filters. The white light generation in sapphire proved to be too challenging for the current state of the setup. Potentially, with a cooled CCD camera, some signals should be detected, as most of the background noise can be removed spectrally. Another issue is the length of the integration time needed to take one frame.

One more important thing to consider is a purity of the crystal. More perfect crystal is – less scattering happens. Some homogenous impurities or defects would potentially help increasing the signal strength. Further investigation should be done to conclude which exact target should be chosen for the best performance.

6.4. Scattering from damaged surface

During experiments, it was observed that the signal of any more strongly scattering object (like surfaces, defects) is very easily detectable. It can be seen in the previous examples, that when pulse hits the surface of the glass plate, the whole image is saturated, because the signal is orders of magnitude higher compared to an air plasma scattering or a bulk medium scattering.

In this sub-chapter short examples of the pulse scattering from surfaces and defects are presented. This potentially could be useful for investigation of laser induced ablation or generally light propagation trough scattering objects with more complex structures.

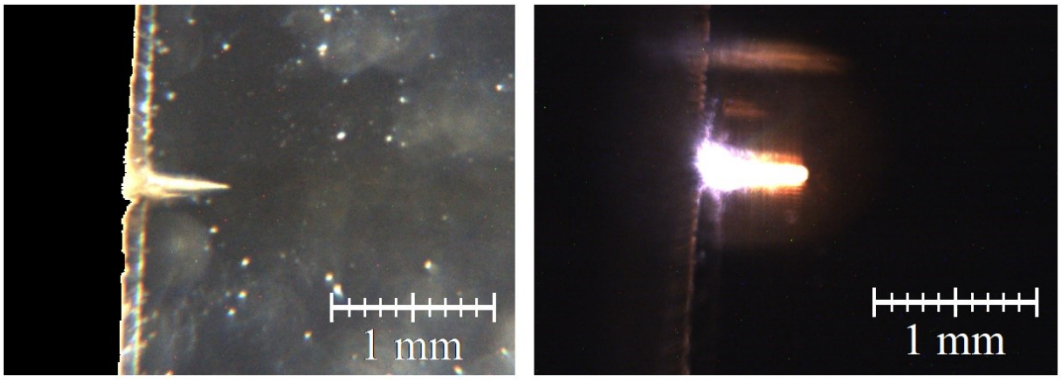

Figure 41. Images of the glass plate with the laser induced surface damage. Without and with laser illumination. Images captured with the time unresolved imaging module.

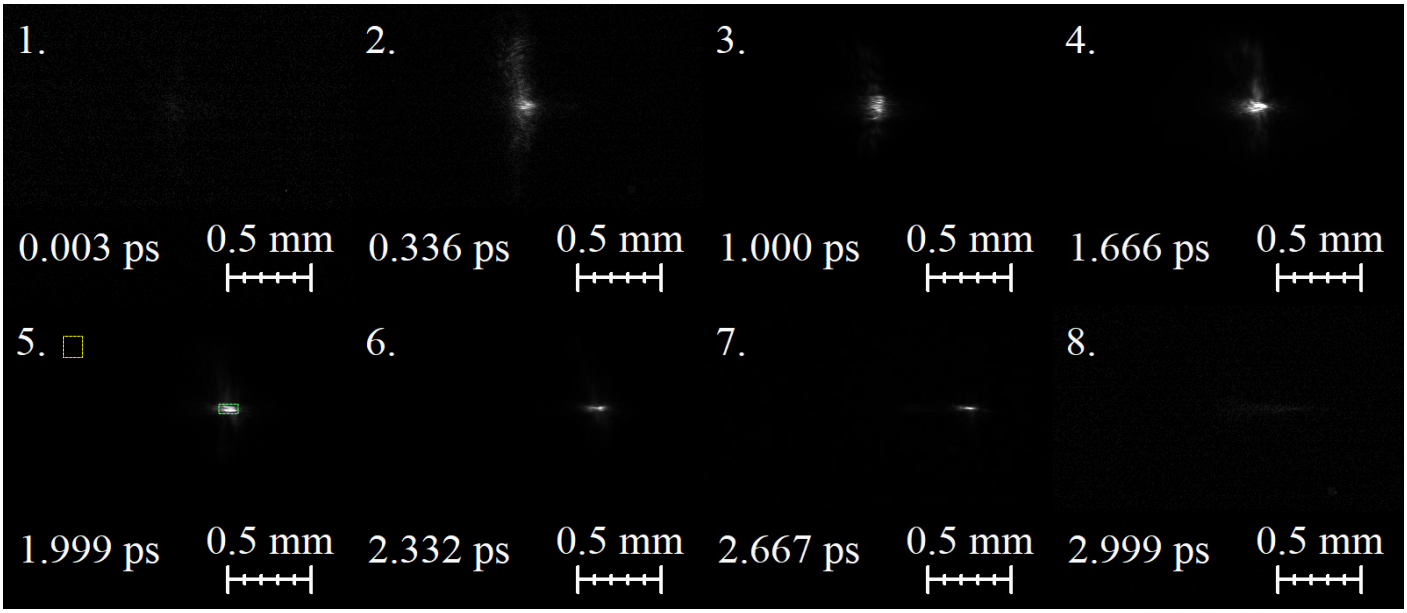

Figure 42. Propagation of the pulse through a laser induced groove on the glass surface. Side view. The integration time for each frame was set to 2.2 ms (it is extremely low compared to the other measurements). Power of the Pump was 303 mW and Gate – 101 mW, +75 lens focusing beam near the surface. In the second frame, the pulse reaches surface of the glass plate. Afterwards, light propagates following a groove shape. Totally >200 pictures taken with a time step of 33 fs. The signal-to-noise ratio: $SNR_{db}(5th) = 33.247$ dB.

If the integration time is increased, the main peak is saturated, but a lot of other weak signals become visible (like in previous measurements from 6.3.1, 6.3.2 chapters). The pre-pulses and post-pulses are observed, side surface scattered light, also sometimes the laser pulse can be seen even before reaching the surface of glass plate (most likely scattered by some ablation induced residue). Examples are presented in Figure 43.

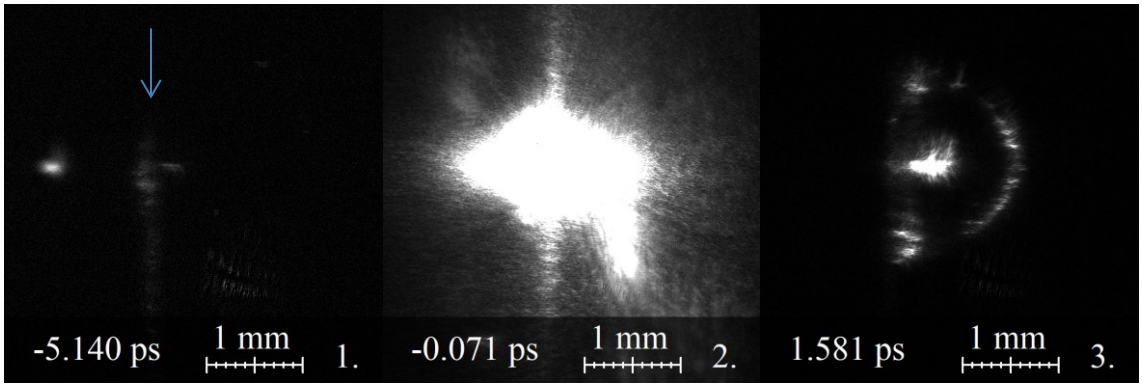

Figure 43. Pulse propagation through a laser induced grove. Side view, saturated signal. The pulse is propagating from left to right. In the first frame – pulse visible even before hitting glass plate. The blue arrow marks the surface of a glass. In the second frame – saturated signal from the pulse hitting the glass surface. Last frame, at the end of the ablation groove, spherically shaped signal appears propagating at the speed of light. Integration time for each frame was ~470 ms. Power of the Pump was 288 mW, while power of the Gatewas 106 mW. Pump was focused using a +75 lens near the surface. Totally >1100 pictures were taken with a time step of 13.3 fs.

6.5. Water

Last target of observation was a cuvette filled with water and a drop of milk. Although the propagation of the laser pulse through water is not ideally repetitive, because gas bubbles are generated, it is still repetitive enough, for a pump-probe type measurement. The water with a drop of milk was chosen as it is a strongly scattering medium. Hence, the pulse propagation in water was expected to be easily observed.

Similarly to bulk media or air, due to the nonlinear change of the refractive index (and induced self-focusing and self-phase modulation) and possibly other nonlinearities such as four-wave-mixing, some new frequencies in the water are also generated, resulting a broadened laser spectrum. Hence, observation of these newly generated laser frequencies was done.

Using 16.5 mm objective laser beam was focused inside the cuvette. Pictures of the experiment are shown in the Figure 44.

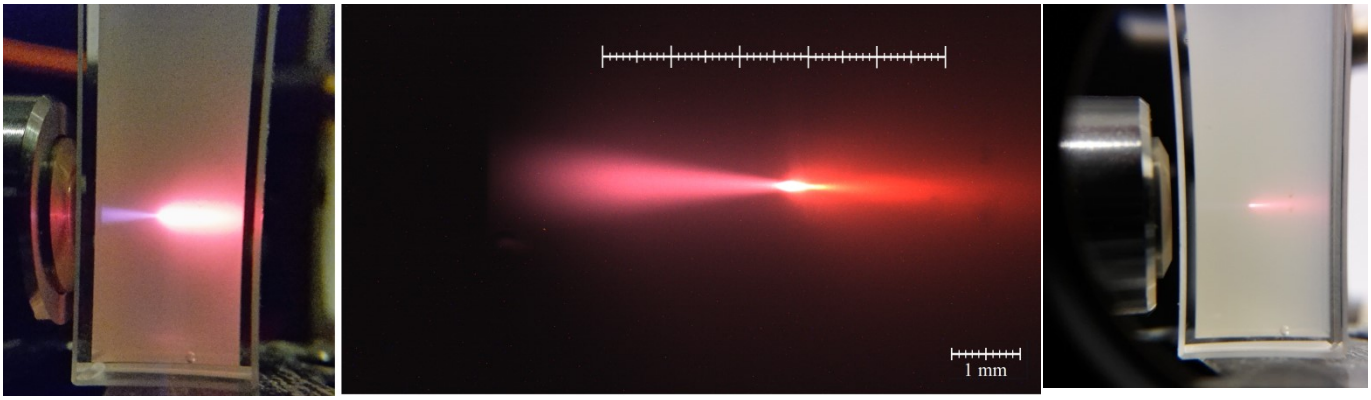

Figure 44. A water filled cuvette with a drop of milk and a laser beam focused inside. The converging purple beam before focus point is an incoming 800 nm laser beam. After the focus point, change of laser spectrum is visible, the broadband light is being generated. The image on the right is taken with the Pump power set to 40 mW, while image on the left is with the maximum Pump power of 180 mW.

The Main results of the time-resolved measurement can be seen in Figure 45. Each frame is a composition of three different pictures from the three measurements corresponding to the different wavelength regions. Three wavelength regions were recorded using FF01-390/SP-25, FB400-10 and FF01-452/45-25 filters. Corresponding detectable frequency ranges (before upconversion) were $535 - 715$ nm; 800 nm and $930 - 1160$ nm.

The signals for longer wavelengths were more easily detectable and integration times of the CCD were set to $t_{800nm} = 55$ ms and $t_{930-1160nm} = 1000$ ms. The signal in the visible range on the other hand was hard to detect and required an extremely long integration time of $t_{530-715nm} = 26.45$ s. The Pump powers were 40 mW for the infrared wavelengths and 50 mW (to increase the signal a little bit) for the visible wavelengths. The Gate power was set to 18 mW for 800 nm and $930 - 1160$ nm regions, while the Gate for $535 - 715$ nm was set to a maximum of 108 mW.

Results showed a 800 nm pulse propagating in a water medium and following a Gaussian beam distribution: the pulse was getting smaller in size and more intense while approaching the focus point. When the light pulse reached the focus point of the beam (and its maximum intensity), new frequencies were generated. After, the pulse was propagating further together with the newly generated frequencies.

The calculated group velocity of propagating 800 nm pulse was $v = \frac{\Delta s}{\Delta t} \approx 2.27 \times 10^8$ m/s. If the water refractive index is around ~1.33 and the group refractive index ~1.34, this is roughly speed of light pulse in a water medium. Different color regions propagate with slightly different speeds, although with this magnification and times scales it's harder to observe it.

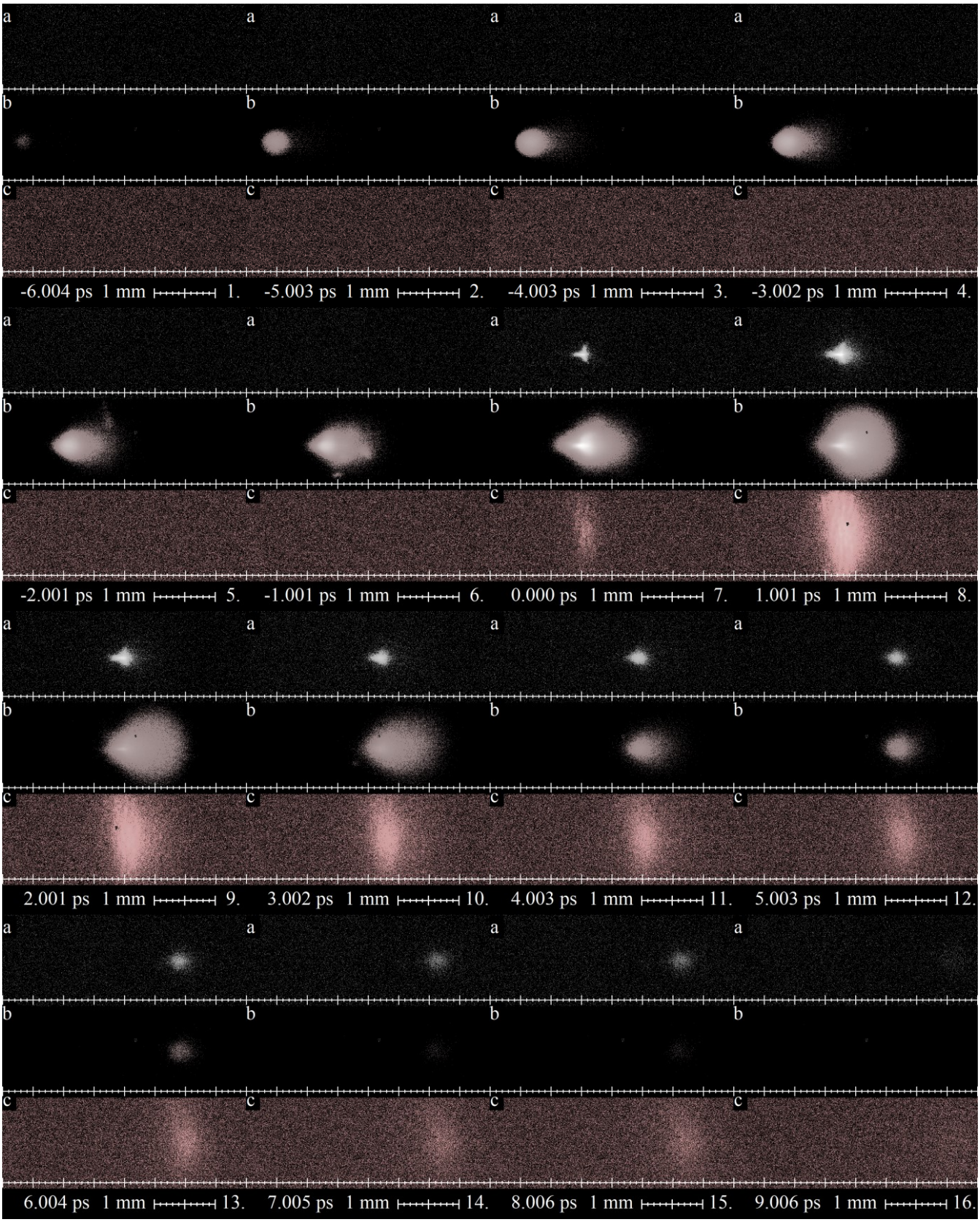

Figure 45. Pulse propagation in water medium. Pulse is propagating from left to right. Section a: $930 - 1160$ nm, section b: 800 nm, section c: $535 - 715$ nm. Totally, >3000 frames were taken with a time step of 16.7 fs for a and b regions and 66.7 for region c. Signal-to-noise ratio of each spectrum: $SNR_{db}(8th, a) = 21.775$ dB; $SNR_{db}(8th, b) = 30.217$ dB; $SNR_{db}(8th, c) = 8.201$ dB; $SNR_{db}(14th, a) = 6.413$ dB; $SNR_{db}(14th, b) = 10.1$ dB; $SNR_{db}(14th, c) = 1.7$ dB;

Notice that the signal visible in section c has a different shape most likely due to an extremely long integration time, compared to the sections a and b. The Images are presented in a logarithmic scale.

Besides that, this was a first example of the Femtosecond Camera successfully recording a time-resolved nonlinear event in several spectral regions.

6.6. Summary of the results

The developed Femtosecond Camera setup was tested and characterized by capturing several different light phenomena such as reflection, scattering and propagation in different mediums. After capturing multiple frames, phenomena were later recreated in a format of slow-motion videos.

By recording reflection from a resolution test target, it was possible to estimate temporal and spatial resolution of the Femtosecond Camera. Temporal resolution, determined by pulse duration of the Gate pulse was estimated to be $\sim 50\,\mathrm{fs}$. Spatial resolution, limited by aberrations due to simple design of the imaging lenses was $\sim 45.3\,\mathrm{lp/mm}$. While spatial resolution can easily be increased, temporal resolution is limited by the output parameters of a used laser system.

Signals originating from reflection and scattering from surfaces or defects exceed the background level significantly and, therefore are very easily detectable. Signal-to-noise ratios of such events vary from $25\,\mathrm{dB}$ to $33\,\mathrm{dB}$. Processes of light scattering from ablation caused defects and scattering from surfaces were also recorded as well as several pulse reflections between surfaces of a glass plate. This indicates, that prominent scattering events, like material ablation and light propagation in complex, scattering structures, while taking place on the ultrafast scale, can be easily recorded and recreated with high temporal and spatial resolution.

On the other hand, weak signals, like pulse scattering from the plasma filaments created by the same pulse can also be recorded. Reconstructed dynamics of the process indicated that while the leading edge of the laser pulse ionizes air and creates plasma, the trailing edge of the pulse is scattered by it and detected by the imaging setup. Captured images allowed to see the pulse propagation through the plasma filament. The signal-to-noise ratio of the captured plasma scattering event was estimated to be $14 - 22\,\mathrm{dB}$, depending of focusing conditions.

Although with current design of this setup it was not possible to observe extremely low signals like pulse propagation in air and white-light filament generation in sapphire, it was possible to capture pulse propagating inside a glass medium, with $SNR_{db} \approx 5\,\mathrm{dB}$. Potentially, even light propagation inside a bulk media could be visualized and investigated.

Finally, capturing pulse propagation and spectrum broadening inside a cuvette filled with water, served as a good example of systems capability of capturing ultra-fast nonlinear events, recording them in high temporal and spatial resolution with additional spectral information.

These various experiments were proof-of-principle type of measurements, demonstrating capabilities and performance of the developed Femtosecond camera.

The main limiting factor for SNR was either thermal noise or background generated by the Gating pulse. The background can be removed if the signal coming from the object has different wavelength than the Gating pulse. It should be noted, that even with the background noise, the system was capable of recording weak signals, like scattering from air plasma or pulse propagation inside a glass. The thermal noise can be reduced by substituting a regular CCD camera with a cooled CCD camera.

7. Conclusions

1. By capturing and recreating a number of ultra-fast processes it was concluded, that the imaging setup, based on the non-collinear sum frequency generation was implemented successfully and therefore, can be used for collecting temporally, spatially and spectrally resolved information.
2. Cross-correlation measurements revealed the Gate and Signal pulses durations are $\sim 50\,\mathrm{fs}$, meaning that the optical shutter was implemented correctly, without introducing additional pulse temporal broadening in the entire optical setup. The temporal resolution of the setup was limited by the output parameters of a used laser system.
3. By capturing image of the resolution test target, the spatial resolution of the Femtosecond camera was estimated to be $\sim 45.3\,\mathrm{lp/mm}$. By comparing it to the diffraction limited spot sizes and the pixel size of the CCD camera, it was determined, that resolution is limited by the aberrations, caused by the imaging optics.
4. During the development of the setup, it was determined, that temporal and spatial distortions of the captured images governed by the non-collinear sum frequency generation can be avoided by introducing pulse front tilting of the Gate pulse.
5. The origin of the observed background signal was found to be either surface-generated or non-phase-matched (or both) second harmonic of the Gate pulse. This becomes a limiting factor of a SNR, when the Signal wavelength matches the Gating wavelength.
6. By measuring the SNR for several BBO crystals of different thicknesses, it was determined, that the SNR could be increased, by having a thicker BBO crystal. In such case, higher SNR comes at a price of reduced temporal resolution, unless a perfect geometry is chosen to compensate the group velocity mismatch between the Signal and Gate pulses.
7. When the Signal wavelength does not match the Gating wavelength, the limiting factor of SNR was the thermal noise of the CCD camera, which can be reduced significantly by replacing a regular CCD sensor with a cooled sensor.
8. Although with low $SNR \approx 5\,\mathrm{dB}$, even extremely weak signals, originating from the pulse propagation in a bulk glass, were detected. This proved the setup is capable of detecting both strong (with $SNR > 25\,\mathrm{dB}$) and weak signals with potential applicability in various measurements.
9. As setup is capable of imaging weak signals while maintaining spectral information, it could potentially be used for visualization and investigation of light propagation or nonlinear processes in various media like solids, gasses, liquids or tissues.

8. Bibliography

[1] E. Muybridge, A horse's motion scientifically determined, Sci. Am., **39**(16), 241 (1878)

[2] G. Gariepy, N. Krstajić, R. Henderson, C. Li, R. R. Thomson, G. S. Buller, B. Heshmat, R. Raskar, J. Leach, D. Faccio, Single-photon sensitive light-in-fight imaging, Nat. Commun., **6**, 6021 (2015), http://dx.doi.org/10.1038/ncomms7021

[3] J. L. Boon, The Eastman High-Speed Camera, Type III, J. Soc. Motion Pict. Eng., **43**(5), 321–326 (1944), http://dx.doi.org/10.5594/J12880

[4] J. H. Waddell, The Rotating-Prism Camera: An Historical Survey, J. SMPTE, **75**(7), 666–674 (1966), http://dx.doi.org/10.5594/J07135

[5] W. S. Boyle, G. E. Smith, Charge Coupled Semiconductor Devices, Bell Syst. Tech. J., **49**(4), 587–593 (1970), https://doi.org/10.1002/j.1538-7305.1970.tb01790.x

[6] G. T. Etoh, Q. A. Nguyen, Y. Kamakura, K. Shimonomura, Y. T. Le, and N. Mori, The Theoretical Highest Frame Rate of Silicon Image Sensors, Sensors, **17**(3) (2017), http://dx.doi.org/10.3390/s17030483

[7] T. G. Etoh, K. Shimonomura, A. Q. Nguyen, K. Takehara, Y. Kamakura, P. Goetschalckx, L. Haspeslagh, P. De Moor, V. T. S. Dao, H. D. Nguyen, N. Hayashi, Y. Mitsui, and H. Inumaru, A 100 Mfps image sensor for biological applications, **10505**, 506–510 (2018), https://doi.org/10.1117/12.2288861

[8] R. Warburton, C. Aniculaesei, M. Clerici, Y. Altmann, G. Gariepy, R. McCracken, D. Reid, S. McLaughlin, M. Petrovich, J. Hayes, R. Henderson, D. Faccio, and J. Leach, Observation of laser pulse propagation in optical fibers with a SPAD camera, Sci. Rep., **7**, 43302 (2017), http://dx.doi.org/10.1038/srep43302

[9] E. Bordenave, E. Abraham, G. Jonusauskas, J. Oberlé, and C. Rullière, Longitudinal imaging in biological tissues with a single laser shot correlation system, Opt. Express, **10**(1), 35–40 (2002), http://dx.doi.org/10.1364/OE.10.000035

[10] S. Brustlein, F. Devaux, and E. Lantz, Picosecond fluorescence lifetime imaging by parametric image amplification, Eur. Phys. J. Appl. Phys., **2**, 161–165 (2005), https://doi.org/10.1051/epjap:2004204

[11] R. Fang, A. Vorobyev, and C. Guo, Direct visualization of the complete evolution of femtosecond laser-induced surface structural dynamics of metals, Light Sci. Appl., **6**(3), 16256 (2017), http://dx.doi.org/10.1038/lsa.2016.256

[12] A. Ehn, J. Bood, Z. Li, E. Berrocal, M. Aldén, and E. Kristensson, FRAME: femtosecond videography for atomic and molecular dynamics, Light Sci. Appl., **6**(9), 17045 (2017), http://dx.doi.org/10.1038/lsa.2017.45

[13] M. M. Gabriel, J. R. Kirschbrown, J. D. Christesen, C. W. Pinion, D. F. Zigler, E. M. Grumstrup, B. P. Mehl, E. E. M. Cating, J. F. Cahoon, and J. M. Papanikolas, Direct Imaging of Free Carrier and Trap Carrier Motion in Silicon Nanowires by Spatially-Separated Femtosecond Pump–Probe Microscopy, Nano Lett., **13**(3), 1336–1340 (2013), https://doi.org/10.1021/nl400265b

[14] K. Nakagawa, T. Suzuki, and F. Kannari, Sequentially Timed All-Optical Mapping Photography for Real- Time Monitoring of Laser Ablation: Breakdown and Filamentation in Picosecond and Femtosecond Regimes, in: *Laser Ablation - From Fundamentals to Applications*, eds.: Tatiana Itina (InTech, 2017), pp. Ch. 05, http://dx.doi.org/10.5772/intechopen.71524

[15] G. T. Etoh, V. D. Son, T. Yamada, and E. Charbon, Toward One Giga Frames per Second — Evolution of in Situ Storage Image Sensors, Sensors, **13**(4), (2013), http://dx.doi.org/10.3390/s130404640

[16] A. Velten, D. Wu, A. Jarabo, B. Masia, C. Barsi, C. Joshi, E. Lawson, M. Bawendi, D. Gutierrez, and R. Raskar, Femto-photography: Capturing and Visualizing the Propagation of Light, ACM Trans. Graph., **32**(4), 44:1-44:8 (2013), http://doi.acm.org/10.1145/2461912.2461928

[17] J. C. Blake, J. Nieto-Pescador, Z. Li, and L. Gundlach, Ultraviolet femtosecond Kerr-gated wide-field fluorescence microscopy, Opt. Lett., **41**(11), 2462–2465 (2016), http://dx.doi.org/10.1364/OL.41.002462

[18] F. Devaux and E. Lantz, Ultrahigh-speed imaging by parametric image amplification, Opt. Commun., **118**(1), 25–27 (1995), https://doi.org/10.1016/0030-4018(95)00212-Q

[19] E. Abraham, K. Minoshima, and H. Matsumoto, Femtosecond laser-induced breakdown in water: time-resolved shadow imaging and two-color interferometric imaging, Opt. Commun., **176**(4), 441–452 (2000), https://doi.org/10.1016/S0030-4018(00)00547-2

[20] J. P. McDonald, J. A. Nees, and S. M. Yalisove, Pump-probe imaging of femtosecond pulsed laser ablation of silicon with thermally grown oxide films, J. Appl. Phys., **102**(6), 63109 (2007), https://doi.org/10.1063/1.2778740

[21] Y. Tochigi, K. Hanzawa, Y. Kato, R. Kuroda, H. Mutoh, R. Hirose, H. Tominaga, K. Takubo, Y. Kondo, and S. Sugawa, A Global-Shutter CMOS Image Sensor With Readout Speed of 1-Tpixel/s Burst and 780-Mpixel/s Continuous, IEEE J. Solid-State Circuits, vol. **48**(1), 329–338 (2013), https://doi.org/10.1109/JSSC.2012.2219685

[22] R. Kuroda, Y. Tochigi, K. Miyauchi, T. Takeda, H. Sugo, F. Shao, and S. Sugawa, A 20Mfps Global Shutter CMOS Image Sensor with Improved Light Sensitivity and Power Consumption Performances, ITE Trans. Media Technol. Appl., **4**(2), 149–154 (2016),

https://doi.org/10.3169/mta.4.149

[23] J. Honour, Electronic camera for simultaneous framing and streak recording, in: *Proc. SPIE 2869, 22nd International Congress on High-Speed Photography and Photonics*, (Santa Fe, United States, 1996), https://doi.org/10.1117/12.273467

[24] J. Honour, High-resolution sixteen-frame ultrafast digital imaging system, in: *Proc. Spie 3968, High-Speed Imaging and Sequence Analysis II* (San Jose, United States, 2000), https://doi.org/10.1117/12.378866

[25] C. T. Chin, C. Lancée, J. Borsboom, F. Mastik, M. E. Frijlink, N. de Jong, M. Versluis, and D. Lohse, Brandaris 128: A digital 25 million frames per second camera with 128 highly sensitive frames, Rev. Sci. Instrum., **74**(12) 5026–5034 (2003), https://doi.org/10.1063/1.1626013

[26] F. Mochizuki, K. Kagawa, S. Okihara, M.-W. Seo, B. Zhang, T. Takasawa, K. Yasutomi, and S. Kawahito, Single-event transient imaging with an ultra-high-speed temporally compressive multi-aperture CMOS image sensor, Opt. Express, **24**(4) 4155–4176 (2016), https://doi.org/10.1364/OE.24.004155

[27] M. Versluis, High-speed imaging in fluids, Exp. Fluids, **54**(1458), 1-35 (2013), https://doi.org/10.1364/OE.24.004155

[28] https://www.hamamatsu.com/resources/pdf/sys/SHSS0022E_FESCA-100.pdf. [Accessed: 04-May-2018].

[29] K. Nakagawa, A. Iwasaki, Y. Oishi, R. Horisaki, A. Tsukamoto, A. Nakamura, K. Hirosawa, H. Liao, T. Ushida, K. Goda, F. Kannari, and I. Sakuma, Sequentially timed all-optical mapping photography (STAMP), Nat. Photonics, **8**, 695 (2014), http://dx.doi.org/10.1038/nphoton.2014.163

[30] T. Suzuki, F. Isa, L. Fujii, K. Hirosawa, K. Nakagawa, K. Goda, I. Sakuma, and F. Kannari, Sequentially timed all-optical mapping photography (STAMP) utilizing spectral filtering, Opt. Express, **23**(23), 30512–30522 (2015), http://dx.doi.org/10.1364/OE.23.030512

[31] T. S. and R. H. and Y. Y. and K. N. and T. S. and F. Kannari, Single-shot 25-frame burst imaging of ultrafast phase transition of Ge 2 Sb 2 Te 5 with a sub-picosecond resolution, Appl. Phys. Express, **10**(9), 92502 (2017), http://dx.doi.org/ 10.7567/APEX.10.092502

[32] E. M. Grumstrup, M. M. Gabriel, E. E. M. Cating, E. M. Van Goethem, and J. M. Papanikolas, Pump–probe microscopy: Visualization and spectroscopy of ultrafast dynamics at the nanoscale, Chem. Phys., **458**, 30–40 (2015), https://doi.org/10.1016/j.chemphys.2015.07.006

[33] C. Schnedermann, J. M. Lim, T. Wende, A. S. Duarte, L. Ni, Q. Gu, A. Sadhanala, A. Rao, and P. Kukura, Sub-10 fs Time-Resolved Vibronic Optical Microscopy, J. Phys. Chem. Lett.,

7(23), 4854–4859, (2016), https://doi.org/10.1021/acs.jpclett.6b02387

[34] M. Seo, S. Boubanga-Tombet, J. Yoo, Z. Ku, A. V Gin, S. T. Picraux, S. R. J. Brueck, A. J. Taylor, and R. P. Prasankumar, Ultrafast optical wide field microscopy, Opt. Express, **21**(7), 8763–8772 (2013), https://doi.org/10.1364/OE.21.008763

[35] N. Zhang, X. Zhu, J. Yang, X. Wang, and M. Wang, Time-Resolved Shadowgraphs of Material Ejection in Intense Femtosecond Laser Ablation of Aluminum, Phys. Rev. Lett., **99** (16), 167602 (2007), https://link.aps.org/doi/10.1103/PhysRevLett.99.167602

[36] Y. Yu, L. Jiang, Q. Cao, B. Xia, Q. Wang, and Y. Lu, Pump-probe imaging of the fs-ps-ns dynamics during femtosecond laser Bessel beam drilling in PMMA, Opt. Express, **23**(25) 32728–32735 (2015), https://doi.org/10.1364/OE.23.032728

[37] H. Hu, X. Wang, N. Zhang, H. Zhai, and P. Wang, Shock induced phenomena in high fluence femtosecond laser ablation of silica glass, in: *Proc. SPIE 7843, High-Power Lasers and Applications V*, 7843 (Beijing, China, 2010).

[38] Z. Wang, B. Zeng, G. Li, H. Xie, W. Chu, F. He, Y. Liao, W. Liu, H. Gao, and Y. Cheng, Time-resolved shadowgraphs of transient plasma induced by spatiotemporally focused femtosecond laser pulses in fused silica glass, Opt. Lett., **40**(24) 5726–5729 (2015), https://doi.org/10.1364/OL.40.005726

[39] M. Domke, S. Rapp, M. Schmidt, and H. P. Huber, Ultrafast pump-probe microscopy with high temporal dynamic range, Opt. Express, **20**(9), 10330–10338 (2012), https://doi.org/10.1364/OE.20.010330

[40] J. Hernandez-Rueda, D. Puerto, J. Siegel, M. Galvan-Sosa, and J. Solis, Plasma dynamics and structural modifications induced by femtosecond laser pulses in quartz, Appl. Surf. Sci., **258**(23), 9389–9393 (2012).

[41] L. Gundlach and P. Piotrowiak, Femtosecond Kerr-gated wide-field fluorescence microscopy, Opt. Lett., vol. **33**(9) 992–994 (2008), https://doi.org/10.1364/OL.33.000992

[42] G. W. Faris and M. Banks, Upconverting time gate for imaging through highly scattering media, Opt. Lett., **19**(22), 1813–1815(1994), https://doi.org/10.1364/OL.19.001813

[43] E. Abraham, E. Bordenave, N. Tsurumachi, G. Jonusauskas, J. Oberlé, C. Rullière, and A. Mito, Real-time two-dimensional imaging in scattering media by use of a femtosecond Cr4+:forsterite laser, Opt. Lett., **25**(12), 929–931 (2000), https://doi.org/10.1364/OL.25.000929

[44] Y. Zhao, S. G. Adie, H. Tu, Y. Liu, B. W. Graf, E. J. Chaney, M. Marjanovic, and S. A. Boppart, Optical parametrically gated microscopy in scattering media, Opt. Express, **22**(19), 22547–22560 (2014), https://doi.org/10.1364/OE.22.022547

[45] L. Pattelli, R. Savo, M. Burresi, and D. S. Wiersma, Spatio-temporal visualization of light

transport in complex photonic structures, Light Sci. Appl., **5**, 16090 (2016), http://10.0.4.14/lsa.2016.90

[46] E. Lantz and F. Devaux, Parametric Amplification of Images: From Time Gating to Noiseless Amplification, IEEE J. Sel. Top. Quantum Electron., **14**(3), 635–647 (2008), https://doi.org/10.1109/JSTQE.2008.918650

[47] L. Zhao, J. Pérez Lustres, V. Farztdinov, and N. P Ernsting, Femtosecond fluorescence spectroscopy by upconversion with tilted gate pulses, Phys. Chem. Chem. Phys., **7**, 1716–1725, (2005). https://doi.org/10.1063/1.4948932

[48] X.-X. Zhang, C. Würth, L. Zhao, U. Resch-Genger, N. P. Ernsting, and M. Sajadi, Femtosecond broadband fluorescence upconversion spectroscopy: Improved setup and photometric correction, Rev. Sci. Instrum., **82**(6), 63108 (2011), https://doi.org/10.1063/1.3597674

[49] J. S. Dam, C. Pedersen, and P. Tidemand-Lichtenberg, High-resolution two-dimensional image upconversion of incoherent light, Opt. Lett., **35**(22), 3796–3798 (2010), https://doi.org/10.1364/OL.35.003796

[50] B. E. A. Saleh and M. C. Teich, *Fundamentals of Photonics* (John Wiley & Sons, Inc., 2001)

[51] A. P. Stabinis and G. Valiulis, *Ultratrumpųjų šviesos impulsų netiesinė optika* (Vilnius: TEV, 2008)

[52] S. A. Akhmanov, V. A. Vysloukh, and A. S. Chirkin, *Optics of Femtosecond Laser Pulses*. (AIP-Press 1992)

[53] R. W. Boyd, Chapter 1 - The Nonlinear Optical Susceptibility BT - *Nonlinear Optics (Third Edition)* (Burlington: Academic Press 2008), pp. 1–67

[54] A. Dubietis, *Netiesinė optika* (Vilniaus universiteto leidykla, 2011)

[55] R. W. Boyd, Chapter 2 - Wave-Equation Description of Nonlinear Optical Interactions BT - *Nonlinear Optics (Third Edition)* (Burlington: Academic Press, 2008) pp. 69–133

[56] J. N. Sweetser, D. N. Fittinghoff, and R. Trebino, Transient-grating frequency-resolved optical gating, Opt. Lett., **22**(8), 519–521 (1997), https://doi.org/10.1364/OL.22.000519

[57] F. J. L. and S. X. Z. and Q. F. L. and G. K. Z. and J. Liu, A new multifunctional device for femtosecond pulse characterization with a wide operating range, Laser Phys. Lett., **11**(1), 15302 (2014).

[58] Z. Bor, B. Racz, G. Szabo, M. Hilbert, and H. A. Hazim, Femtosecond pulse front tilt caused by angular dispersion, **32**, 32–34 (1993), https://doi.org/10.1117/12.145393

[59] H. Hirori and K. Tanaka, Nonlinear Optical Phenomena Induced by Intense Single-Cycle Terahertz Pulses, IEEE J. Sel. Top. Quantum Electron., **19**(1), 8401110 (2013), https://doi.org/10.1109/JSTQE.2012.2221685

[60] A. V Smith,“Group-velocity-matched three-wave mixing in birefringent crystals, Opt. Lett., **26**(10), 719–721 (2001), https://doi.org/10.1364/OL.26.000719

[61] R. J. Gehr, M. W. Kimmel, and A. V Smith, Simultaneous spatial and temporal walk-off compensation in frequency-doubling femtosecond pulses in b-BaB2O4, Opt. Lett., **23**(16), 1298–1300 (1998), https://doi.org/10.1364/OL.23.001298

[62] C. Pedersen, E. Karamehmedović, J. S. Dam, and P. Tidemand-Lichtenberg, Enhanced 2D-image upconversion using solid-state lasers, Opt. Express, **17**(23), 20885–20890 (2009), https://doi.org/10.1364/OE.17.020885

[63] J. S. Dam, C. Pedersen, and P. Tidemand-Lichtenberg, Theory for upconversion of incoherent images, Opt. Express, **20**(2), 1475–1482 (2012), https://doi.org/10.1364/OE.20.001475

[64] C. H. R. Ooi and M. R. Talib, Intricate Plasma-Scattered Images and Spectra of Focused Femtosecond Laser Pulses, Sci. Rep., **6**, 32056 (2016), http://dx.doi.org/10.1038/srep32056

[65] N. L. Aleksandrov, S. B. Bodrov, M. V Tsarev, A. A. Murzanev, Y. A. Sergeev, Y. A. Malkov, and A. N. Stepanov, Decay of femtosecond laser-induced plasma filaments in air, nitrogen, and argon for atmospheric and subatmospheric pressures, Phys. Rev. E, **94**(1), 13204 (2016) https://doi.org/10.1103/PhysRevE.94.013204

9. Summary

Džiugas Kimbaras

FEMTOSECOND IMAGING BASED ON SUM FREQUENCY GENERATION

Main topic of this thesis was building a high-speed imaging setup by using a sum frequency generation based optical shutter together with a wide-field imaging module. Such module would allow capturing and recreating various physical phenomena with a femtosecond temporal resolution. Main tasks of this thesis were to design, build and test such imaging device.

Basic working principle of the constructed setup is described as following. The laser pulse is split into two pulses – the Gate pulse and the Object pulse. The Object pulse hits the chosen target of interest (for example cuvette with water) and is partly scattered or reflected. The scattered light is collected and imaged on the nonlinear crystal, where it overlaps with short Gate pulse. When two pulses overlap, sum frequency signal is generated and registered by the CCD camera. Changing delay between the Gate and Object pulses allows upconverting different part of the scattered light, thus capturing different moment of the observed event.

While designing the setup, a lot of various problems were solved, trying to achieve the best temporal and spatial resolution, as well as high signal-to-noise ratio. It was observed, that to generate not distorted images with high temporal resolution, front of the Gate pulse has to match front of the scattered Object pulse. Pulse front tilting of the Gate pulse was achieved by using diffraction grating and 4f telescope. Another important observation was that main sources of the background noise are the thermal noise of the camera and the 2nd harmonic signal, generated by the Gating pulse. It was concluded, that to achieve better SNR, it is better to use thicker nonlinear crystal and cooled image sensor. Finally, to keep the high temporal resolution, it is important to choose geometry of non collinear interaction correctly, which would satisfy phase-matching and compensate group velocity mismatch of the Gate and Object pulses.

Image setup was tested by capturing and recreating various fast processes, like light reflection from resolution test target, laser pulse scattering from the plasma filament in air, propagation of the light pulse in glass, scattering from various defects, pulse propagation and nonlinear spectral broadening in water. Signal-to-noise ratio varied from ~ 5 dB (weak signals like pulse propagation in glass), to 33 dB (reflection from the surface).

Using cross-correlation technique it was measured, that temporal resolution of the setup is ~50 fs. Resolution is limited by the duration of the Gate pulse, which was determined by the used laser setup. Spatial resolution, limited by optical abberations, was measured to be ~45.3 lp/mm.

10. Santrauka

Džiugas Kimbaras

FEMTOSEKUNDINĖS SKYROS VAIZDINIMAS PANAUDOJANT SUMINIO DAŽNIO GENERACIJĄ

Aukštos laikinės skyros vaizdinimas leidžia stebėti ir tyrinėti kitaip nematomus, sparčiai vykstančius gamtos procesus. Užregistruota vaizdų seka atskleidžia proceso dinamiką – jo erdvinių ir spektrinių charakteristikų kitimą laike. Elektroninių sensorių laikinė skyra siekia šimtus pikosekundžių, fotoelektronų kamerų – šimtus femtosekundžių. Norint stebėti dar spartesnius procesus, pavyzdžiui, šviesos impulso sklidimą, reikalingi dar greitesni registravimo būdai. Jie realizuojami naudojant šviesą – trumpus lazerio impulsus. Šio darbo tema – vaizdinimo sistemos, pagrįstos nekolinearios suminio dažnio generacijos principu, kūrimas, konstravimas, charakterizavimas ir taikymas, stebint šviesos sklidimo dinamiką.

Sukurta vaizdinimo sistema veikia toliau aprašytu principu. Pirmiausia trumpas lazerio impulsas padalijamas į du impulus – skenuojantįjį ir stebimąjį. Stebimasis impulsas nukreipiamas į kokį nors objektą, pavyzdžiui, kiuvetę su vandeniu. Dalis pro objektą sklindančio impulso yra išsklaidoma arba atspindima. Sklaidyta šviesa surenkama ir objekto plokštuma atvaizduojama ant netiesinio kristalo. Antrasis – skenuojantysis impulsas, prasklidęs pro valdomą vėlinimo liniją, nukreipiamas į tą patį netiesinį kristalą. Persiklojus objekto sklaidytai šviesai ir skenuojančiam impulsui, kristale generuojamas suminio dažnio signalas, kuris registruojamas vaizdo jutikliu su krūvio sąsajos įtaisu. Skenuojantysis impulsas veikia kaip optinė sklendė, iškerpanti tik trumpą sklaidytos šviesos signalo dalį. Keičiant vėlinimą tarp skenuojančiojo ir stebimojo impulsų, objekto sklaidyta šviesa ir skenuojantysis impulsas persikloja vis kitu laiko momentu, registruojamas vis kitas stebimo proceso momentas.

Kuriant sistemą buvo sprendžiamos įvairios problemos, siekiant kuo geresnės laikinės bei erdvinės skyrų, aukšto signalo ir triukšmo santykio. Buvo pastebėta, kad, norint gauti neiškraipytą erdvėje ir gera laikine skyra pasižymintį signalą, reikia, jog skenuojančiojo impulso frontas sutaptų su sklaidytos šviesos impulso frontu. Skenuojančio impulso pokrypis buvo sukurtas naudojant difrakcinę gardelę ir 4f atvaizdavimo sistemą. Taip pat buvo nustatyta, kad pagrindiniai foninio triukšmo šaltiniai yra šiluminis kameros triukšmas ir skenuojančiojo impulso generuojamas antros harmonikos signalas. Pastebėta, kad siekiant pagerinti signalo ir triukšmo santykį geriau naudoti storesnį netiesinį kristalą. Norint išlaikyti gerą laikinę skyrą, svarbu parinkti tinkamą nekolinearią geometriją, tenkinančią fazinio sinchronizmo sąlygą ir kompensuojančią grupinių greičių nederinimą tarp skenuojančio ir sklaidytos šviesos impulsų.

Šia vaizdinimo sistema buvo stebėti ir sėkmingai atkurti įvairūs procesai. Užregistruotas šviesos atspindys nuo stiklo plokštelės su erdvinei rezoliucijai įvertinti skirta struktūra, lazerio impulso sklaida nuo ore sugeneruoto plazmos filamento, šviesos impulso sklidimas stiklo plokštelėse (tiek paviršiais, tiek tūryje), šviesos impulso sklidimas ir jo spektro išplitimas dėl netiesinių sąveikų vandenyje. Signalo triukšmo santykis priklauso nuo stebimų objektų signalo. Itin stipriems signalams, pavyzdžiui, atspindžiui nuo stiklo plokštelės paviršiaus, buvo būdingas signalo ir triukšmo santykis, lygus $25 - 33$ dB. Tuo tarpu itin silpnų signalų, pavyzdžiui, impulso sklidimo stikle, signalo ir triukšmo santykis buvo ~ 5 dB.

Kryžminės koreliacijos metodu įvertinta sukurtos vaizdinimo sistemos laikinė skyra lygi ~ 50 fs. Ši skyra ribojama skenuojančiojo impulso trukmės, kuri lygi naudojamos lazerinės sistemos generuojamų impulsų trukmei. Erdvinė skyra, ribojama naudojamos optikos sukurtų aberacijų, nustatyta ~ 45.3 lp/mm.